Thesis for The Degree of Doctor of Philosophy in
Shipping and Marine Technology

Efficient Full-Scale CFD for Ship Hydrodynamics

Michal Orych

Department of Mechanics and Maritime Sciences
Chalmers University of Technology
Gothenburg, Sweden, 2024

Efficient Full-Scale CFD for Ship Hydrodynamics

Michal Orych
ISBN 978-91-7905-982-8

Doktorsavhandlingar vid Chalmers tekniska högskola
Ny serie nr 5448
ISSN 0346-718X

Department of Mechanics and Maritime Sciences
Chalmers University of Technology
SE-412 96 Göteborg,
Sweden
Phone: +46(0)31 772 1000

Printed by Chalmers Digitaltryck,
Gothenburg, Sweden 2024.

Efficient Full-Scale CFD for Ship Hydrodynamics

Michal Orych

Department of Mechanics and Maritime Sciences
Chalmers University of Technology

Abstract

An efficient numerical approach for ship hydrodynamics, involving a hybrid free-surface potential flow/RANS method, is explored. The work focuses on estimating the delivered power of ships in calm water and in waves, highlighting the benefits of full-scale simulations, particularly for ships with Energy Saving Devices. The robustness and accuracy of the approach are confirmed by verifications and validations at both model and full-scale, showing uncertainties significantly lower than in typical sea trial data, with comparison errors within a few percent. This is attributed to the discretization, structured grids and solving the steady RANS equations in a coupled manner. Special attention is paid to hull roughness effects in the simulations, a critical factor in ship resistance. Efficiency variations of different Energy Saving Devices between model and full scale, notably influenced by Reynolds number dependency, are also highlighted. The method demonstrates effectiveness across various cargo ship types and conditions, suggesting its suitability as a reliable and practical tool for ship designers for full-scale hydrodynamic performance evaluation and optimization. It complements physical testing and more expensive, unsteady RANS methods.

Keywords

CFD, RANS, Roughness, Ship, Full-scale, Uncertainty, Verification, Validation, Self-propulsion, Seakeeping, Energy-Saving Device

List of Publications

Appended publications

The thesis consists of an extended summary and the appended papers listed below.

[**Paper I**] **M. Orych**, S. Werner, L. Larsson. (2022). Roughness effect modelling for wall resolved RANS – Comparison of methods for marine hydrodynamics. *Ocean Engineering, 266*.

[**Paper II**] **M. Orych**, S. Werner, L. Larsson. (2021). Validation of full-scale delivered power CFD simulations. *Ocean Engineering, 238*.

[**Paper III**] **M. Orych**, M. Östberg S., M. Kjellberg, S. Werner, L. Larsson. (2023). Speed and delivered power in waves—Predictions with CFD simulations at full scale. *Ocean Engineering, 285*.

[**Paper IV**] K. Kim, M. Leer-Andersen, S. Werner, **M. Orych**, Y. Choi. (2012, August). Hydrodynamic Optimization of Pre-swirl Stator by CFD and Model Testing. *29th Symposium on Naval Hydrodynamics, Gothenburg, Sweden.*

[**Paper V**] K. Kim, M. Leer-Andersen, **M. Orych**. (2014, November). Hydrodynamic Optimization of Energy Saving Devices in Full Scale. *30th Symposium on Naval Hydrodynamics, Hobart, Tasmania, Australia.*

Other publications

In addition to the appended papers, I have authored or co-authored the following publications on numerical hydrodynamics:

[**a**] **M. Orych**, M. Kjellberg, L. Larsson. (2023). Efficient CFD simulations for speed and delivered power in waves at full scale. *The Naval Architect, RINA.*

[**b**] K.,B. Korkmaz, K. Kim, M. Liefvendahl, S. Werner, **M. Orych**. (2023). A validation study of full-scale CFD simulation for sea trial performance prediction of ships. *Proceedings, 10th International Conference on Computational Methods in Marine Engineering, MARINE.*

[**c**] K. Ljungqvist, **M. Orych**, L. Larsson, C. Finnsgård. (2017). Comparison of modern keel types for sailing yachts. *International Journal of Small Craft Technology 159,B2, 81-88.*

[**d**] **M. Orych**, L. Larsson. (2015, March). Hydrodynamic aspects of transom stern optimisation. *Proceedings, 5th High Performance Yacht Design Conference, Auckland, 247-256.*

[**e**] J. Allroth, T-H. Wu, **M. Orych**, L. Larsson. (2015, March). Sailing yacht transom sterns-a systematic CFD investigation. *Proceedings, 5th High Performance Yacht Design Conference, Auckland, 257-266.*

[**f**] K.,B. Korkmaz, **M. Orych**, L. Larsson, C. Finnsgård. (2015). CFD predictions including verification and validation of resistance, propulsion and local flow for the Japan Bulk Carrier (JBC) with and without an energy saving device. *Proceedings, Tokyo 2015 Workshop on CFD in Ship Hydrodynamics Vol.3.*

[**g**] **M. Orych.** (2013). Development of a free surface capability in a RANS solver with coupled equations and overset grids. *Licentiate Thesis, Göteborg, Chalmers University of Technology.*

[**h**] L. Broberg, **M. Orych**. (2013). Energy saving device evaluation in full scale using computational fluid dynamics. *Proceedings, International Conference on Ship and Offshore Technology, ICSOT India, RINA Conference.*

[**i**] K. Ljungqvist, B. Axfors, H. Tunander, **M. Orych**, F. Vesting, L. Larsson. (2012, March). Investigation of keel bulbs for sailing yachts. *Proceedings, 4th High Performance Yacht Design Conference, Auckland, New Zealand.*

[**j**] L. Broberg, **M. Orych**. (2012). An efficient numerical technique to simulate the propeller hull interaction. *International Journal of Innovative Research & Development, Vol 1 Issue 10, 494-507.*

[**k**] L. Broberg, **M. Orych**. (2011). Modern tools for efficient hydrodynamic design of ships. *Proceedings, International Conference on Ship and Offshore Technology, ICSOT India, RINA Conference.*

[**l**] **M. Orych**, L. Larsson, B. Regnström. (2010). Adaptive overlapping grid techniques and spatial discretization schemes for increasing surface sharpness and numerical accuracy in free surface capturing methods. *Proceedings, 28th Symposium on Naval Hydrodynamics, Pasadena, California, USA, 12-17 September.*

[**m**] **M. Orych**, L. Larsson, B. Regnström. (2010). Viscous free surface calculations for the KCS hull. *Proceedings, Gothenburg 2010 - A Workshop on Numerical Ship Hydrodynamics .*

[**n**] L. Zou, L. Larsson, **M. Orych**. (2010). Verification and validation of CFD predictions for a manoeuvring tanker. *Journal of Hydrodynamics, B22/5, 438-445.*

[**o**] **M. Orych**, B. Regnström, L. Larsson. (2009). A surface capturing method in the RANS solver SHIPFLOW. *Proceedings, 12th Numerical Towing Tank Symposium.*

[**p**] **M. Orych**, H. Ran, L. Larsson. (2008). Numerical investigations of the effects of winglets on IACC yacht drag components. *Proceedings, 3rd High-Performance Yacht Design Conference, Auckland, New Zealand, 203-214.*

[**q**] M. Östberg, B. Regnström, L. Broberg, **M. Orych**. (2008). Verification and validation of the chapman incompressible RANS solver. *Proceedings, 3rd Workshop on CFD Uncertainty Analysis, Lisbon, Portugal.*

[**r**] B. Regnström, L. Broberg, M. Östberg, **M. Orych**. (2006). An uncertainty exercise for incompressible flow. *Proceedings, 2nd Workshop on CFD Uncertainty Analysis, Lisbon, Portugal.*

Acknowledgments

First and foremost, I wish to express my deepest gratitude to my main supervisor, Lars Larsson. His guidance, patience, and profound expertise have been pivotal throughout this research journey. Even in challenging moments, Lars never allowed me to give up, constantly pushing me forward and encouraging me to persevere. His steadfast belief in my potential has been a significant source of motivation, and I am forever thankful for his mentorship. I must also express my profound appreciation to my second supervisor, Rickard Bensow. His unique perspectives, critical feedback, and commitment to academic rigour have significantly shaped the outcome of my research. Rickard's persistent encouragement to finalize and wrap things up guided me to the completion of this thesis. I would also like to express my appreciation to Sofia Werner, my co-supervisor, for her invaluable contributions, feedback, and persistent encouragement. Her expertise added a rich layer of depth to my research, and her strong support made a significant difference in my journey. Special thanks go to Leif Broberg, my boss at FLOWTECH International AB, whose understanding and flexibility allowed me to balance my professional and academic commitments. His encouragement and belief in my capabilities were a great source of motivation. I am indebted to Keunjae Kim, my co-author and a great expert in ship hydrodynamics, for his significant intellectual contributions and for sharing the research results. Collaborating with him has enriched my experience significantly. I would also like to extend my heartfelt thanks to my colleagues, Björn Regnström, Magnus Östberg and Martin Kjellberg, for their invaluable contributions to my research. Beyond their professional insights and collaborative spirit, their constant encouragement and support were a source of strength for me. Their ability to cheer me up and keep me motivated during arduous times has been both uplifting and essential to my research journey. Lastly, I wish to acknowledge the PhD coordinators at Chalmers University of Technology. Their relentless efforts behind the scenes ensured a smooth and productive research process. Their dedication to fostering a nurturing research environment is admirable.

In addition to the immense personal and academic support I received, this research was made feasible through considerable financial backing. I am profoundly grateful to the Swedish Energy Agency and FLOWTECH International AB for their generous financial contributions. The specific study on energy-saving devices also benefited greatly from the support extended by

Daewoo Shipbuilding & Marine Engineering Co., Ltd. The computations were enabled by resources provided by FLOWTECH, SSPA/RISE and the Swedish National Infrastructure for Computing (SNIC) at the National Supercomputing Centre (NSC) partially funded by the Swedish Research Council through grant agreement no. 2018-05973.

Nomenclature

6DOF	Six Degrees of Freedom
AHR	Average Hull Roughness
BEM	Boundary Element Method
CFD	Computational Fluid Dynamics
EASM	Explicit Algebraic Stress Model
EEDI	Energy Efficiency Design Index
EEXI	Energy Efficiency Existing Ship Index
EFD	Experimental Fluid Dynamics
ESD	Energy Saving Device
GMRES	Generalized Minimal Residual Method
IMO	International Maritime Organization
ITTC	International Towing Tank Conference
ITTC-78	1978 ITTC Power Prediction Method
KCS	KRISO Container Ship
KRISO	Korea Research Institute of Ships and Ocean Engineering
KVLCC2	KRISO VLCC, second variant
Lpp	Length between perpendiculars
PSS	Pre-swirl Stator
RANS	Reynolds-Averaged Navier–Stokes
RMS	Root-Mean-Square
VOF	Volume of Fluid

β, β^*	Modeling coefficients for k and ω equations
δ_{ij}	Kronecker's delta
γ_0, γ_1	Modeling coefficients for k and ω equations
$\mathbf{\Lambda}$	Eigenvalues of $\mathbf{A}$
ν	Kinematic viscosity
ν_E	Total kinematic viscosity
ν_T	Turbulent kinematic viscosity
ω	Specific dissipation of turbulent kinetic energy
$\sigma_k, \sigma_\omega, \sigma_{\omega 2}$	Modeling coefficients for k and ω equations
τ, η	Auxiliary functions in turbulence model
ξ_B	Parameter direction crossing the boundary
λ	Wave length
$\mathbf{A}, \mathbf{A}_1, \mathbf{A}_2$	Discrete Jacobians
$\mathbf{f_v}, \mathbf{g_v}, \mathbf{h_v}$	Viscous fluxes
$\mathbf{f}, \mathbf{g}, \mathbf{h}$	Convective fluxes
$\mathbf{F}_i, \mathbf{F}_{i,i}$	Fluxes
$\mathbf{L}, \mathbf{R}$	Left and right eigenvectors of $\mathbf{A}$
$\mathbf{q}$	Vector of dependent variables
$\overline{u_i' u_j'}$	Reynolds stress tensor
a, b, c	Auxiliary functions in turbulence model
a_1, a_2, a_3, a_4	Auxiliary functions in turbulence model
B	Bias error
C_F	Frictional resistance coefficient
C_P	Pressure resistance coefficient
C_T	Total resistance coefficient
C_W	Wave resistance coefficient
C_{AW}	Wave added resistance coefficient
D	Experimental data

E	Comparison error
F_1	Auxiliary function in turbulence model
f_w	Weather factor
Fr	Froude number
H_s	Significant wave height
k	Turbulent kinetic energy
K_Q	Torque coefficient
k_S	Equivalent sand grain roughness height
K_T	Thrust coefficient
n	Propeller revolution rate
n_g	Number of grid cells
n_i	Normal to surface
P	Precision error
p	Time average pressure, Order of accuracy
P_D	Delivered power
R_i	Volume force
Re	Reynolds number
S_{ij}	Strain-rate
T_z	Wave zero up-crossing period
U_D	Experimental uncertainty
U_G	Grid uncertainty
u_i, u, v, w	Time-averaged velocity components in Cartesian directions
$u_i^{'}$	Fluctuating velocity components in Cartesian directions
U_{SN}	Numerical uncertainty
U_{Val}	Validation uncertainty
w_n	Nominal wake
W_{ij}	Rotation-rate
x_i	Cartesian coordinates

Contents

Part I

Summary

Chapter 1

Introduction

Full-scale flow simulations around ship hulls have likely been attempted since Computational Fluid Dynamics (CFD) methods began emerging in this field. Interestingly, one of the first reported examples of such an endeavour is the work conducted by a developer of SHIPFLOW and co-founder of FLOWTECH International AB (Broberg et al., 1991). This work was one of three full-scale Reynolds number submissions to the 1990 SSPA-CTH-IIHR Workshop on Ship Viscous Flows (Larsson et al., 1991). At that time, the focus was solely on the velocity field at the propeller plane, which involved solving Reynolds-Averaged Navier–Stokes (RANS) equations with wall functions. The feasibility of performing simulations at high Reynolds numbers without using wall functions was presented in a study (Eça and Hoekstra, 1997), which utilized PARNASSOS — a program originally developed at MARIN in the Netherlands (Raven and Hoekstra, 1985) and later extended at IST in Portugal. The results indicated the correct flow behaviour with increasing Reynolds number. Subsequently, the same group further explored the impact of turbulence models on the near-wake field and hull resistance at full scale (Eça and Hoekstra, 2001). The Gothenburg 2000 Workshop on Numerical Ship Hydrodynamics (Larsson et al., 2000) attracted 23 participants. Several of them submitted full-scale simulations. Groups from France (Deng and Visonneau, 2000), later involved in ISIS code development, and Germany (Abdel-Maksoud et al., 2000), utilizing the CFX code, both presented encouraging wake and resistance predictions.

One of the first published full-scale simulations using the free-surface fitting RANS method was presented at 25^{th} Symposium on Naval Hydrodynamics (Raven et al., 2004). At the same time, MARIN initiated a European co-operative project known as EFFORT (European Full-Scale Flow Research and Technology) (Verkuyl and Raven, 2003). The primary objectives were to enhance and validate CFD methods for analyzing viscous flow around a ship's hull at full scale, and to apply these methods to practical ship and propeller design. Six participants submitted simulation data for several test cases, and the results were in line with expectations, highlighting the importance of full-scale predictions (Hänninen and Mikkola, 2006). In 2008, a prediction of full-scale power based entirely on CFD was still not considered reliable enough for tasks

requiring high accuracy (Raven et al., 2008).

Applying an unsteady Reynolds-Averaged Navier-Stokes (RANS) approach with a level-set free-surface capturing method (Bhushan et al., 2009) demonstrated the impressive capabilities of CFDShip-Iowa. Promising full-scale results for resistance, powering with a body force propeller model, seakeeping, and manoeuvring simulations, including hull roughness effects, were described. Still, the authors indicated that more verifications and validations were necessary. Self-propulsion computations of the KCS containership, performed at full scale with a rotating propeller, were also presented, using the same code (Castro et al., 2011). The scale effects on ship hydrodynamics, with a focus on full-scale self-propulsion using a hybrid Reynolds-Averaged Navier-Stokes/Boundary Element Method (RANS/BEM) approach to represent the propeller through a potential flow method, were described in detail (Starke and Bosschers, 2012). The importance of CFD simulations at full scale for Energy Saving Devices (ESDs) was illustrated in publications that are part of this thesis (Kim et al., 2012; Kim et al., 2014). These studies highlight strong scale effects and the diminishing advantages of ESDs with increasing Reynolds number. By this point, it had become evident that full-scale CFD simulations could provide valuable results, potentially rivalling towing tanks, which depend on extrapolated measurements to predict delivered power.

Lloyd's Register Technical Investigation Department published a study based on one ship from their database (Ponkratov and Zegos, 2015), finding that their CFD predictions aligned more closely with sea trials than did the model test extrapolations using the ITTC-78 method. Similar conclusions were documented in a thesis (Mikkelsen and Steffensen, 2016) that utilized sea trial data from DNV GL. In 2016 Lloyd's Register organized the first Workshop on Ship Scale Hydrodynamic Computer Simulations, attracting participants from 15 countries. A general cargo vessel, MV Regal, was used as the validation case (Ponkratov, 2017). Further analysis of these published results shows that the average comparison error of the predicted power is 13% for all submitted results. Notably, 3 out of the 27 participants achieved errors below 3% for all considered speeds (Werner, 2021). The availability of this validation data also resulted in many more publications for the same test case (Murakami and Hino, 2017; Starke et al., 2017; Wieleman, 2018; Jasak et al., 2019; Pena et al., 2020; Song et al., 2021).

For validation purposes, it is essential to conduct the sea-trial data collection meticulously, under favourable conditions, and to document it thoroughly to enable the estimation of uncertainties. For accurate validation, laser scanning of the hull, propeller, and appendages is recommended, while roughness measurements are deemed absolutely essential. The most comprehensive and high-quality validation data obtained this way, accessible to a broader group of researchers, comes from the Joint Research Project titled "Development of an industry recognised benchmark for Ship Energy Efficiency Solutions" (JoRes, 2023). Thus far, measurements for five different ships have been shared with project participants. However, there are plans to make this data publicly available once the joint project is finalized. The growing interest in these activities is further amplified by the potential to utilize CFD results for compliance with

the Energy Efficiency Existing Ship Index (EEXI) and the Energy Efficiency Design Index (EEDI).

From the studies mentioned above, it can be confidently deduced that unsteady RANS codes can simulate full-scale self-propulsion with high accuracy. However, these simulations demand significant computational resources and can take weeks or even months to complete. Therefore, they can hardly be considered a practical tool for ship designers working in a typical commercial environment with short lead times. While selecting the most advanced methods might seem ideal, it is not always feasible or necessary. Through careful verification and validation studies, methods that are both efficient and sufficiently accurate can be selected.

This work focuses on simpler numerical methods that can provide accurate results on a conventional desktop computer within hours. A fast, steady RANS code with an embedded lifting line propeller model is used for self-propulsion simulations while the added resistance in waves is estimated with an unsteady potential flow seakeeping method (Orych et al., 2021; Orych et al., 2022; Orych et al., 2023). This approach is utilized to estimate power requirements at full scale both in calm water and in waves. Additionally, the scale effects impacting Energy Saving Devices are investigated (Kim et al., 2012; Kim et al., 2014).

1.1 Problem statement and objectives

The use of unsteady Reynolds-Averaged Navier-Stokes methods in full-scale simulations presents a significant challenge. These simulations, especially when they involve propulsion systems with rotating propellers, require substantial computational resources even in calm water. They require exceptional grid resolutions and very short time steps to provide accurate and dependable results. This computational intensity escalates dramatically when the simulations are extended to accommodate six degrees of freedom (6DOF) in wave conditions, leading to execution times that may become unmanageable or even exceed the computing capacities typically accessible in ship design offices. Consequently, detailed simulations of this nature may extend over prolonged periods, ranging from several weeks to months, and require the deployment of hundreds of CPU cores.

Given these challenges, the primary objective of this work is to identify, verify, and validate computational methods capable of delivering accurate full-scale power predictions in both calm water and in waves within a limited time frame and computational resources. The aim is to complete the simulations within a few hours, utilizing the computational capabilities of a standard office desktop computer. With efficiency in mind, a simpler and more computationally efficient hybrid method - combining steady RANS and potential flow solvers - is being reconsidered as an alternative to the more complex and resource-intensive unsteady RANS approach.

1.2 Scope

The scope of this research is established with the aim of developing a numerical methodology that is well-suited for full-scale simulations and seakeeping analysis. This methodology should ensure a balance between computational efficiency and the accuracy of results.

- Methodology Identification and Enhancement

  The initial step is to explore and identify existing computational methods that align with the specific needs. This task encompasses reviewing methods available in SHIPFLOW to ascertain which ones may be applicable and effective for full-scale simulations in calm water and waves. Once the potential candidates are identified, the focus shifts to their improvement. This involves making necessary adjustments and refinements to optimize these methods for the planned applications while considering inherent limitations.

- Capabilities

  The selected methods must be capable of handling simulations with high Reynolds numbers to ensure their applicability to full-scale conditions. Additionally, it is critical that these methodologies take hull surface roughness into account due to its significant impact on the required power output of the ship. Furthermore, they should enable precise predictions of the complex interactions between the hull, propeller, and appendages, thus providing a complete understanding of the propulsion system, including energy-saving devices. Lastly, the methods should accurately account for the increased resistance due to incoming waves.

- Verification and Validation

  To ensure the reliability and accuracy of the selected methods, it is essential to conduct a series of verification and validation simulations. Verification will involve performing multiple simulations for selected conditions to determine numerical errors and to indicate the consistency and reliability of the results. Validations should provide a clear indication of the comparison errors by comparing the simulation results with measurements from both model scale tests and full-scale sea trials.

By adhering to the outlined scope, this research aspires to make a valuable contribution to the field of computational fluid dynamics in practical ship hydrodynamics.

1.3 Thesis outline

Part I provides an overview of the entire body of work:

- **Chapter 1** introduces the subject of the thesis and highlights how the included papers contribute to a cohesive work. It states the objectives and the scope of this research.

- **Chapter 2** describes the methodologies employed throughout the thesis, including their inherent limitations.
- **Chapter 3** reports the most important results derived from the research.
- **Chapter 4** highlights summaries of each paper, detailing the division of work, underlying motivations, and primary objectives.
  - *Paper I* describes the implementation, verification, and validation of roughness models essential to full-scale ship hydrodynamics.
  - *Paper II* focuses on verification and validation of full-scale delivered power predictions using the hybrid method.
  - *Paper III* elaborates on simulations with incoming wave and wind effects, reinforcing the real-world applicability of the explored numerical methods.
  - *Paper IV* presents a validation of the hybrid method through simulations of energy-saving devices.
  - *Paper V* illustrates the necessity of full-scale simulations in the design process of energy-saving devices.
- **Chapter 5** contains a discussion and possible directions for future work.

Part II encloses all the papers in their original, published form.

It is essential to note that the included papers represent an integral part of the thesis. Part I of this thesis provides a descriptive overview of the work, whereas Part II covers all the details in the published papers.

Chapter 2

Methodology and limitations

In this work, SHIPFLOW software is employed. It utilizes three distinct CFD methods: steady potential flow, unsteady potential flow, and steady RANS. The steady potential flow solver was utilized in its existing form without further modification. Enhancements have been applied to the other methodologies to meet the objectives of the project. Outputs from all solvers are combined to achieve the required final results. Several crucial factors influenced the selection of methods:

- Accuracy and Robustness:

  The most important attributes of any numerical tool are its accuracy and robustness. For this project, it is imperative to predict the delivered power in waves at full scale within error margins acceptable to ship designers, shipyards, and ship operators. Accuracy without robustness is of limited utility, as the simulations must be successfully performed across a variety of ship types and conditions. Both of these essential aspects will be emphasized throughout this thesis.

- Time required to perform simulations:

  Computing an added resistance in waves using a RANS code with viscous free-surface modelling can take several weeks on a single high-performance computer. A calm water self-propulsion simulation at full scale with a rotating propeller geometry may require a few days. Such extensive time demands can make the tool impractical for tasks requiring multiple simulations. For ship designers, a more rapid execution time is essential. With the selected approach, seakeeping simulations can be conducted in approximately 1.5 hours per wave length, and a self-propulsion run at full scale is completed in about 2 hours using a single computer equipped with a 24-core CPU.

- Availability of the source code and experience with using and developing the software:

As a PhD student, I had the opportunity to work with several CFD codes. However, my extensive use of SHIPFLOW since 2004 in various projects has provided me with the greatest familiarity and consistently positive experiences with this code, contributing significantly to my decision to pursue this research path. Direct access to the source code provides the opportunity to not only evaluate existing capabilities but also to improve or implement new methods. Such access represents a significant advantage for a PhD project focused on numerical simulations.

2.1 Calm water wave resistance, sinkage and trim

A potential flow panel method is used to compute calm water wave resistance, dynamic sinkage, and trim (Janson, 1997). The method is based on the assumption of an inviscid and irrotational flow, where the velocity corresponds to the gradient of a velocity potential, which is governed by Laplace's equation. This equation requires boundary conditions on all boundaries within the computational domain: the velocity normal to the hull must be zero, and on the free surface, the flow should be tangential with the pressure remaining constant. The disturbance from the hull diminishes to zero at infinity. The free-surface boundary condition is applied to the wavy free surface, which is initially unknown, rendering the problem nonlinear. It is resolved through a series of linearized approximations. Quadrilateral panels are utilized to describe both the hull and the free surface. On the free surface, first-order panels of the Rankine source type (Hess and Smith, 1964) are employed, whereas the hull is represented using higher-order panels. Throughout the iterative solving process, continuous adjustments are made to the vessel positioning, requiring the regeneration of panelization for both the hull and the free surface. Convergence is achieved when changes in trim, sinkage, and wave elevation meet predefined criteria. The wave resistance is calculated using the transverse wave cut technique, which provides more robust results than pressure integration for the current method (Janson and Spinney, 2004). In subsequent stages, the hull position, determined from the potential flow simulations, is used as input for RANS simulations. Additionally, wave resistance values derived from the potential flow method are integrated, resulting in a one-way coupling (Orych et al., 2021). The RANS viscous simulation results do not affect the previously calculated trim, sinkage, or wave resistance.

2.2 Calm water resistance and propulsion

The viscous resistance and propulsion simulations utilize a steady, incompressible, single-phase, finite-volume RANS equation solver with an Explicit Algebraic Stress turbulence Model (EASM) and direct near-wall region treatment, i.e. without wall functions. A double-model approach is used where the free-surface is approximated by a plane of symmetry. The chosen methods are

specifically tailored to improve the efficiency and robustness of the solver in handling high Reynolds number flows. The solver is built around structured grids with overlapping (overset) capability, which is used for appendages. It uses Roe's Approximate Riemann solver for inviscid fluxes, which is particularly suitable for flows with abrupt changes or even discontinuities of the field variables. Additionally, the momentum and continuity equations are solved in a coupled manner for better pressure-velocity interaction. This approach is particularly adept at handling flows with very steep velocity gradients, which are encountered in the boundary layers of full-scale ships.

The entire numerical method, with the exception of the roughness modelling, constitutes the background material that was already in place before this work began. Given its critical role in full-scale self-propulsion simulations, a more detailed description of the RANS method is presented in the following subsections.

2.2.1 Momentum and continuity equations

In the present framework, the flow field is assumed to reach a steady state, leading to the omission of time-dependent terms in the RANS equations. Under the assumption of constant density, the continuity equation simplifies to the conservation of volume flow rate. For turbulent flows, the momentum equation, with the Boussinesq assumption included and the continuity equation, are then expressed as follows:

$$\underbrace{\frac{\partial(u_j u_i)}{\partial x_j}}_{1} = \underbrace{R_i}_{2} \underbrace{- \frac{\partial p}{\partial x_i} - \frac{2}{3}\frac{\partial k}{\partial x_i}}_{3} + \underbrace{\frac{\partial}{\partial x_j}\left[(\nu + \nu_T)\left(\frac{\partial u_i}{\partial x_j} + \frac{\partial u_j}{\partial x_i}\right)\right]}_{4} \tag{2.1}$$

$$\frac{\partial u_i}{\partial x_i} = 0 \tag{2.2}$$

For the sake of clarity and to maintain the flow of the text, all symbols used in the equations are defined in the nomenclature section. The numbered underbraces, (l), indicate equation terms referred to in the text.

2.2.2 Turbulence modelling equations

In ship hydrodynamics, one of the most well-established turbulence models is $k-\omega$ SST (Menter, 1993). This model, based on the Boussinesq approximation, has been implemented and thoroughly tested in the code during the early 2000s. The results indicated a tendency to underestimate some of the vortical structures typically observed in ship flows. Consequently, a slightly more sophisticated Explicit Algebraic Stress Model (EASM) was implemented based on Deng et al., 2005. It is based on the $k-\omega$ SST model, but calculates individual Reynolds stresses using nonlinear algebraic equations. The results show better agreement with model scale measurements and maintain stability at high Reynolds numbers. In the momentum equation (Eq. 2.1), the term

related to the nonlinear part (2) of the Reynolds stress tensor (Eq. 2.5), is added explicitly to the volume force vector R_i, see term (2) in Eq. 2.1. The transport equations for the turbulent kinetic energy, k, and for the specific dissipation rate, ω, are:

$$\underbrace{\frac{\partial(u_j k)}{\partial x_j}}_{1} = \underbrace{P}_{2} \underbrace{-\beta^* k\omega}_{3} + \underbrace{\frac{\partial}{\partial x_j}\left[(\nu + \sigma_k \nu_T)\frac{\partial k}{\partial x_j}\right]}_{4} \tag{2.3}$$

$$\underbrace{\frac{\partial(u_j \omega)}{\partial x_j}}_{1} = \underbrace{\frac{\gamma}{\nu_T}P}_{2} \underbrace{-\beta\omega^2}_{3} + \underbrace{\frac{\partial}{\partial x_j}\left[(\nu + \sigma_\omega \nu_T)\frac{\partial \omega}{\partial x_j}\right]}_{4} + \underbrace{2\sigma_{\omega 2}\frac{1-F_1}{\omega}\frac{\partial k}{\partial x_j}\frac{\partial \omega}{\partial x_j}}_{5} \tag{2.4}$$

where the production term is $P = -\overline{u_i' u_j'}\frac{\partial u_i}{\partial x_j}$, and the Reynolds stress tensor is given by:

$$\begin{aligned}\overline{u_i' u_j'} =& \frac{2}{3}k\delta_{ij} \\ & - 2\nu_t[\underbrace{S_{ij}}_{1} + \underbrace{a_2 a_4(S_{ik}W_{kj} - W_{ik}S_{kj}) - 2a_3 a_4(S_{ik}S_{kj} - \frac{1}{3}S_{mn}S_{mn}\delta_{ij})}_{2}]\end{aligned} \tag{2.5}$$

where the turbulent eddy viscosity is given by:

$$\nu_t = \max\left(-k\alpha_1, 0.0005\frac{k}{\beta^*\omega}\right) \tag{2.6}$$

and α_1 is obtained by solving the following cubic equation:

$$\left(\frac{\alpha_1}{\tau}\right)^3 - a\left(\frac{\alpha_1}{\tau}\right)^2 + b\left(\frac{\alpha_1}{\tau}\right) + c = 0 \tag{2.7}$$

with the remaining parameters:

$$a = \frac{\gamma_1}{\eta^2\tau^2\gamma_0},\ b = \frac{\gamma_1^2 - 2\eta^2\tau^2\gamma_0 a_1 - \frac{2}{3}\eta^2\tau^2 a_3^2 + 2R^2\eta^2\tau^2 a_2^2}{(2\eta^2\tau^2\gamma_0)^2},\ c = \frac{\gamma_1 a_1}{(2\eta^2\tau^2\gamma_0)^2},$$

$$R^2 = \frac{W_{ij}W_{ij}}{\eta^2},\ W_{ij} = \frac{1}{2}\left(\frac{\partial u_i}{\partial x_j} - \frac{\partial u_j}{\partial x_i}\right),\ \eta^2 = S_{ij}S_{ij},\ S_{ij} = \frac{1}{2}\left(\frac{\partial u_i}{\partial x_j} + \frac{\partial u_j}{\partial x_i}\right)$$

2.2.3 Boundary conditions

The boundary conditions, as presented in Table 2.1, are implemented using two layers of ghost cells outside the fluid domain. There are no wall functions used in the code, allowing for direct integration of the equations to the wall and thus enabling a more detailed resolution of the boundary layer flow. The no-slip condition is applied on the hull and appendages, while the slip is used for the outer boundary as well as the symmetry planes, including the free surface.

Table 2.1: The boundary conditions

No-slip	Slip	Inflow	Outflow
$u_i = 0$	$u_i n_i = 0,\ \frac{\partial u_i}{\partial \xi_B} = 0$	$u_i = \text{Constant}$	$\frac{\partial u_i}{\partial \xi_B} = 0$
$\frac{\partial p}{\partial \xi_B} = 0$	$\frac{\partial p}{\partial \xi_B} = 0$	$\frac{\partial p}{\partial \xi_B} = 0$	$p = 0$
$k = f(k_s^+)$	$\frac{\partial k}{\partial \xi_B} = 0$	$k = \text{Constant}$	$\frac{\partial k}{\partial \xi_B} = 0$
$\omega = f(u_\tau, k_s^+ \ldots)$	$\frac{\partial \omega}{\partial \xi_B} = 0$	$\omega = \text{Constant}$	$\frac{\partial \omega}{\partial \xi_B} = 0$

2.2.4 Roughness modelling

To account for the effect of hull roughness, the boundary conditions for the specific dissipation of turbulent kinetic energy, ω, and the turbulent kinetic energy, k, are adjusted according to a model based on empirical correlations (Aupoix, 2014). A detailed description of the implementation, verification and validation is given in Paper I. For a given equivalent roughness height k_s, the wall value of k is obtained from the following function:

$$k_w = \max\left[0, \frac{1}{\sqrt{\beta^*}} \tanh\left(\left(\frac{\log\left(\frac{k_s^+}{30}\right)}{\log(10)} + \left(1 - \tanh\left(\frac{k_s^+}{125}\right)\right)\right) \tan\left(\frac{k_s^+}{125}\right)\right)\right] u_\tau^2 \tag{2.8}$$

and the wall value of ω is defined by:

$$\omega_w = \min\left[\left(\frac{300}{{k_s^+}^2}\left(\tanh\left(\frac{15}{4k_s^+}\right)\right)^{-1} + \frac{191}{k_s^+}\left(1 - \exp\left(\frac{-k_s^+}{250}\right)\right)\right)\frac{u_\tau^2}{\nu}, \frac{6\nu}{\beta^* y^2}\right] \tag{2.9}$$

where $k_s^+ = \frac{u_\tau}{\nu} k_s$ and y is a distance to the wall.

2.2.5 Propeller modelling

To simulate the effect of the propeller, body forces are introduced to the Navier-Stokes equations. As the flow passes the propeller-swept volume, its linear and angular momentum are increased, mimicking the effect of a propeller with an infinite number of blades. The forces vary in space but are time-independent and produce a steady flow induced by the propeller. These body forces are calculated using a built-in lifting line propeller analysis program (Zhang, 1990). Additionally, a component of friction resistance is considered, contributing to the propeller torque through a simple coefficient. The body forces are recalculated in every iteration of the RANS solver. During the self-propulsion simulations, the program automatically adjusts the propeller rotational speed to find a balance between the resistance and the thrust (ITTC, 2017a).

2.2.6 Computational grids

The solver uses multi-block, overlapping, structured grids to represent the geometry. The dynamic hull attitude is calculated separately by the steady potential flow method and applied to the geometry prior to grid generation.

2.2.7 Discretization

The system of Reynolds-Averaged Navier-Stokes, continuity, and transport equations for the turbulent kinetic energy and the specific dissipation rate of the kinetic energy of turbulence can be written in the conservative form in the Cartesian coordinate system. This approach simplifies the understanding of the discretization process:

$$\frac{\partial \mathbf{f}}{\partial x} + \frac{\partial \mathbf{g}}{\partial y} + \frac{\partial \mathbf{h}}{\partial z} = \frac{\partial \mathbf{f_v}}{\partial x} + \frac{\partial \mathbf{g_v}}{\partial y} + \frac{\partial \mathbf{h_v}}{\partial z} + \mathbf{r} \tag{2.10}$$

where the inviscid $(\mathbf{f}, \mathbf{g}, \mathbf{h})$ and viscous $(\mathbf{f_v}, \mathbf{g_v}, \mathbf{h_v})$ fluxes are:

$$\mathbf{f} = \begin{bmatrix} u^2 + p \\ uv \\ uw \\ u \\ uk \\ u\omega \end{bmatrix}, \qquad \mathbf{g} = \begin{bmatrix} uv \\ v^2 + p \\ vw \\ v \\ vk \\ v\omega \end{bmatrix}, \qquad \mathbf{h} = \begin{bmatrix} uw \\ vw \\ w^2 + p \\ w \\ wk \\ w\omega \end{bmatrix} \tag{2.11}$$

$$\mathbf{f_v} = \begin{bmatrix} \tau_{xx} \\ \tau_{yx} \\ \tau_{zx} \\ 0 \\ \nu_k \frac{\partial k}{\partial x} \\ \nu_\omega \frac{\partial \omega}{\partial x} \end{bmatrix}, \qquad \mathbf{g_v} = \begin{bmatrix} \tau_{xy} \\ \tau_{yy} \\ \tau_{zy} \\ 0 \\ \nu_k \frac{\partial k}{\partial y} \\ \nu_\omega \frac{\partial \omega}{\partial y} \end{bmatrix}, \qquad \mathbf{h_v} = \begin{bmatrix} \tau_{xz} \\ \tau_{yz} \\ \tau_{zz} \\ 0 \\ \nu_k \frac{\partial k}{\partial z} \\ \nu_\omega \frac{\partial \omega}{\partial z} \end{bmatrix} \tag{2.12}$$

and p is the mean pressure plus the isotropic part of turbulent stress, $\frac{2}{3}k$. The linear part of the stress tensor is defined as $\tau_{ij} = (\nu + \nu_T)(\frac{\partial u_i}{\partial x_j} + \frac{\partial u_j}{\partial x_i})$. The

vector $\mathbf{r}$, on the right-hand side, represents the source term, which contains the explicit terms and is also used to introduce the propeller forces.

The convective terms of the equation (Eq. 2.10) are linearized using Roe's Approximate Riemann method (Roe, 1981). This approach to an incompressible, single-phase flow solver is unconventional since this method is mainly used for problems where shock waves are of interest. However, the method proved beneficial for flows exhibiting steep velocity and pressure gradients near solid boundaries and around complex geometries, which are present in full-scale ship simulations. The core idea is to linearize the flux functions around the discontinuity to simplify the problem while maintaining the behaviour of the actual non-linear system. Roe's procedure suggests that for a given system of hyperbolic partial differential equations, for example: $\frac{\partial \mathbf{F}(\mathbf{U})}{\partial x} = 0$, to which the chain rule is applied, giving $\mathbf{A}(\mathbf{U})\frac{\partial \mathbf{U}}{\partial x} = 0$, where $\mathbf{A} = \frac{\partial \mathbf{F}}{\partial \mathbf{U}}$ is the Jacobian matrix of a flux vector $\mathbf{F}(\mathbf{U})$, a matrix $\tilde{\mathbf{A}}(\mathbf{U}_i, \mathbf{U}_{i+1}) = \mathbf{A}(\mathbf{U})$ can be found that is assumed constant between two cells. This matrix must satisfy the conditions that make it consistent with the exact Jacobian as $\mathbf{U}_i, \mathbf{U}_{i+1} \rightarrow \mathbf{U}$, should have only real eigenvalues and should be conserving: $\mathbf{F}_{i+1} - \mathbf{F}_i = \tilde{\mathbf{A}}(\mathbf{U}_{i+1} - \mathbf{U}_i)$

For the RANS solver, the convective flux differences with respect to $\mathbf{q} = (u, v, w, p, k, \omega)^T$ can be written:

$$\Delta\mathbf{f} = \mathbf{A}_1(\Delta\mathbf{q}), \qquad \Delta\mathbf{g} = \mathbf{A}_2(\Delta\mathbf{q}), \qquad \Delta\mathbf{h} = \mathbf{A}_3(\Delta\mathbf{q}) \tag{2.13}$$

where $\mathbf{A}_1$,$\mathbf{A}_2$,$\mathbf{A}_3$ are the discrete Jacobians of the dependent variables. The eigensystem is evaluated for a linear combination of the Jacobians: $\mathbf{A} = n_x\mathbf{A}_1 + n_y\mathbf{A}_2 + n_z\mathbf{A}_3$, with dependent variables calculated at the interface between the two states. Then the matrix $\mathbf{A}$ is split into positive and negative parts:

$$\mathbf{A} = \mathbf{A}^+ + \mathbf{A}^- \tag{2.14}$$

with

$$\mathbf{A}^+ = \mathbf{R}\mathbf{\Lambda}^+\mathbf{L} \quad \text{and} \quad \mathbf{A}^- = \mathbf{R}\mathbf{\Lambda}^-\mathbf{L} \tag{2.15}$$

where $\mathbf{L}$, $\mathbf{R}$ are the left and right eigenvectors of $\mathbf{A}$ and $\mathbf{\Lambda}^+$, $\mathbf{\Lambda}^-$ are the positive and negative diagonal eigenvalue matrices. The flux difference then can be written as:

$$n_x\Delta\mathbf{f} + n_y\Delta\mathbf{g} + n_z\Delta\mathbf{h} = (\mathbf{A}^+ + \mathbf{A}^-)\Delta\mathbf{q} \tag{2.16}$$

For a given control volume with index i, j, k the first order upwind definition of a flux at face $i + \frac{1}{2}$ is

$$\mathbf{F}_{i+\frac{1}{2}} = \frac{1}{2}(\mathbf{F}_i + \mathbf{F}_{i+1}) - \frac{1}{2}|\Delta\mathbf{F}_{i,i+1}| \tag{2.17}$$

and the flux difference over face $s_{i+\frac{1}{2}}$ is:

$$\begin{aligned}\Delta\mathbf{F}_{i,i+1} &= \mathbf{F}_{i+1} - \mathbf{F}_i \\ &= \Delta s_{i+\frac{1}{2}}(n_x\Delta\mathbf{f}_{i,i+1} + n_y\Delta\mathbf{g}_{i,i+1} + n_z\Delta\mathbf{h}_{i,i+1}) \\ &= \Delta s_{i+\frac{1}{2}}\mathbf{A}_{i,i+1}\Delta\mathbf{q}_{i,i+1}\end{aligned} \tag{2.18}$$

Since $\mathbf{A}_{i,i+1}$ can be split into positive and negative parts, the absolute value of the flux difference can be written:

$$|\Delta\mathbf{F}_{i,i+1}| = \Delta s_{i+\frac{1}{2}}(\mathbf{A}^+_{i,i+1} - \mathbf{A}^-_{i,i+1})\Delta\mathbf{q}_{i,i+1} \tag{2.19}$$

The second-order accuracy is achieved through the application of an explicit flux correction (Dick and Linden, 1992; Chakravarthy and Osher, 1985). Additional terms are introduced, and the flux is composed of limited upwind and central fluxes. The second-order upwind flux is as follows:

$$\begin{aligned}\mathbf{F}_{i+\frac{1}{2}} &= \frac{1}{2}(\mathbf{F}_i + \mathbf{F}_{i+1}) \\ &\quad - \frac{1}{2}\sum_n \Delta\mathbf{F}^{n+}_{i,i+1} + \frac{1}{2}\sum_n \Delta\mathbf{F}^{n-}_{i,i+1} \\ &\quad + \frac{1}{2}\sum_n \widetilde{\Delta\mathbf{F}}^{n+}_{i-1,i} - \frac{1}{2}\sum_n \widetilde{\Delta\mathbf{F}}^{n-}_{i+1,i+2}\end{aligned} \tag{2.20}$$

where $\widetilde{\Delta\mathbf{F}}^{n+}_{i-1,i} = \Delta s_{i+\frac{1}{2}}\mathbf{r}^n_{i+\frac{1}{2}}\lambda^n_{i+\frac{1}{2}}\mathbf{l}^n_{i+\frac{1}{2}}\Delta\mathbf{q}_{i-1,i}$, and n refers to the n^{th} eigenvalue and $\mathbf{r}^n$ and $\mathbf{l}^n$ refer to the n^{th} right and left eigenvectors. $\widetilde{\Delta\mathbf{F}}^{n-}_{i+1,i+2}$ follows a similar definition.

The second-order central difference flux is:

$$\mathbf{F}_{i+\frac{1}{2}} = \frac{1}{2}(\mathbf{F}_i + \mathbf{F}_{i+1}) \tag{2.21}$$

To obtain results with a low numerical diffusion but maintain stability, a high-resolution scheme is constructed based on a combination of upwind and central differences flux with the help of limiters:

$$\begin{aligned}\mathbf{F}_{i+\frac{1}{2}} &= \frac{1}{2}(\mathbf{F}_i + \mathbf{F}_{i+1}) \\ &\quad - \frac{1}{2}\sum_n \Delta\mathbf{F}^{n+}_{i,i+1} + \frac{1}{2}\sum_n \Delta\mathbf{F}^{n-}_{i,i+1} \\ &\quad + \frac{1}{2}\sum_n \widetilde{\widetilde{\Delta\mathbf{F}}}^{n+}_{i-1,i} - \frac{1}{2}\sum_n \widetilde{\widetilde{\Delta\mathbf{F}}}^{n-}_{i+1,i+2}\end{aligned} \tag{2.22}$$

where the limited values are:

$$\widetilde{\widetilde{\Delta\mathbf{F}}}^{n+}_{i-1,i} = \mathrm{Lim}(\widetilde{\Delta\mathbf{F}}^{n+}_{i-1,i}, \Delta\mathbf{F}^{n+}_{i,i+1}) \tag{2.23}$$

$$\widetilde{\widetilde{\Delta\mathbf{F}}}^{n-}_{i+1,i+2} = \mathrm{Lim}(\widetilde{\Delta\mathbf{F}}^{n-}_{i+1,i+2}, \Delta\mathbf{F}^{n-}_{i,i+1}) \tag{2.24}$$

and Lim denotes a limited combination of both arguments. The flux limiters are incorporated into the discretization scheme in order to avoid wiggles in the solution that may occur due to not monotonicity-preserving schemes such as central or fully upwind. The limiter functions, Lim, select an appropriate argument based on their mutual relations, which can indicate non-physical oscillations or overshoots to non-realistic values of the solution. Stable results are achieved with the blending of schemes or locally lowering the order of accuracy.

The diffusion term (4) of Eq. 2.1 can be written as:

$$\frac{\partial}{\partial x_j}\left(\nu_E\left(\frac{\partial u_i}{\partial x_j}+\frac{\partial u_j}{\partial x_i}\right)\right) = \underbrace{\frac{\partial}{\partial x_j}\left(\nu_E\frac{\partial u_i}{\partial x_j}\right)}_{1} + \underbrace{\frac{\partial \nu_E}{\partial x_j}\frac{\partial u_j}{\partial x_i}}_{2} \tag{2.25}$$

where $\nu_E = \nu + \nu_T$.

In Eq. 2.25, the first term (1) is discretized with a central difference scheme. The second term (2) is discretized using a finite difference method with a central difference scheme and is added to the right-hand side of the equation system. The turbulence model equations (Eq. 2.3) and (Eq. 2.4) contain the term (4) that is similar to the first term in Eq. 2.25, which is treated in the same way as in the momentum equations.

The production terms (2) in both k and ω equations, (Eq. 2.3) and (Eq. 2.4) as well as the last term (5) of equation 2.4 are treated explicitly. All of them are discretized using a central difference scheme. The dissipation terms (3) are Newton-linearized and treated implicitly (Merci et al., 1985) to avoid negative values of k and ω when solving the set of equations.

2.2.8 Linear equations solver

The momentum and continuity equations are solved in a coupled manner, whereas the turbulent quantities are solved separately. A Krylov-type solver from the Portable, Extensible Toolkit for Scientific Computation (PETSc, 2020c) is used to solve linear equations. Specifically, the GMRES method (PETSc, 2020b), complemented by the block Jacobi preconditioner (PETSc, 2020a), has proven to be particularly efficient in this context, showing rapid convergence and robust stability.

2.3 Added resistance in waves

To calculate the added resistance in waves, a solver based on a nonlinear unsteady potential flow method for free surface flows with floating bodies

subject to 6DOF is used (Coslovich et al., 2021). The free surface is traced by markers using a mixed Eulerian-Lagrangian approach. In the Eulerian step, velocity potential and velocity of each marker are computed with a boundary element method (BEM). In the Lagrangian step, the free surface boundary conditions are integrated in time, and the position and velocity potential of markers are updated. Once the Lagrangian step is finished, a new free surface mesh is generated by interpolating the surface elevation from the updated positions of the markers. In addition, the boundary conditions for the next Eulerian step are obtained by interpolating the velocity potential of the markers. The hull body motions are calculated by summing up the pressure forces on the hull panels and integrating the corresponding rigid body acceleration in time. Bernoulli's equation gives the total pressure on the hull, and for robustness reasons, an acceleration potential is used to obtain the time derivative of the velocity potential. A 4th-order Adams-Bashforth-Moulton predictor-corrector method is utilized for time integration. The method includes a nonlinear decomposition of the solution, separating it into an undisturbed incident wave field and a disturbance field that arises due to the presence of the hull (Ducrozet et al., 2014). This ensures that incident waves far from the hull do not have to be resolved by the BEM, and thereby, larger panels can be used away from the hull without affecting the quality of the incident wave field, which is described analytically by 5th-order Stokes wave theory for regular waves. The code has an automatic way to detect risks for wave breaking and applies additional pressure in such regions of the free surface to mitigate local wave breaking (Mola et al., 2017). Additionally, to avoid wave reflections from the domain boundaries, a damping zone is introduced. A forcing term that eliminates the disturbance, i.e. the difference between the undisturbed incident waves and the total computed wave height, is applied close to the outer boundaries (Kjellberg et al., 2022).

2.4 Propulsion in waves

The propulsion simulations in waves, incorporating all three solvers presented earlier, are elaborated in Paper III. In the RANS simulations, the calm water resistance, added resistance in waves, and viscous resistance are collectively summed. The thrust generated by the propeller then counterbalances the total resistance. This approach significantly reduces computational effort compared to the application of unsteady RANS solvers, which can alternatively be used for propulsion simulations in waves. While the combined approach offers considerable savings in computing time, it might not capture all the interactions and flow details as accurately as a single, complete, unsteady RANS simulation. Thus, it is important to acknowledge its limitations and consider their impact on the results.

2.5 Possible limitations of the approach

The approach used in this work has several approximations and limitations that may restrict the range of applications. The following are identified as key absent features:

- **Viscous effects on wave resistance.** The wave resistance calculations using potential flow methods do not account for the viscous effects, which include the influence of boundary layer growth along the hull. This omission can lead to an overestimation of wave height.

- **Wave effects on viscous resistance.** The free surface elevation along the hull and local velocity variations near the free surface are not incorporated when calculating the boundary layer.

- **Wave breaking.** Owing to the constraints of potential flow, the effects of wave breaking are excluded, and its subsequent influence on the wave pattern and resistance remains unaddressed.

- **Propeller and free surface interactions.** The efficiency of the propeller is affected by the waves generated by the hull. Additionally, the action of the propeller influences the elevation of the free surface, which in turn further alters its efficiency. These interactions are not incorporated into the current approach.

- **Propeller pressure pulses.** In this study, a lifting line method is employed within a steady RANS framework, which does not capture the unsteady effects of pressure pulses caused by the propeller blades as they rotate through the non-uniform wake near both the hull and the free surface.

- **Propeller cavitation.** Vapour cavities may form locally in the water around the propeller due to a significant drop in pressure. When these cavities collapse, they produce shock waves, leading to vibration, noise, reduced propulsion efficiency, and the potential for erosion on the propeller surface. The single-phase, steady RANS method does not capture these details.

- **Time-varying wake.** The wake generated by a ship is inherently unsteady, a characteristic that becomes more pronounced in wave conditions. In the current simulations, this dynamic is not captured, as wave simulations and steady self-propulsion simulations are conducted independently.

- **Time-varying submergence and loading of the propeller.** The hull resistance and motion in waves result in propeller load and rotational speed variation. The propeller submergence will change in time, and an occasional emergence may occur. These effects, which impact engine and propeller performance, could not be captured within the scope of this approach.

- **Simulation of aerodynamic forces.** The aerodynamic resistance of the ship structure above the free surface is estimated using empirical methods in all simulations, potentially introducing inaccuracies in the total resistance calculation.

2.5.1 Wave making and viscous flow

The neglection of the wave making/viscous flow interaction is a critical part of a hybrid double-model RANS/potential flow approach. If this interaction is significant for cases to which the method is applied, the choice of this approach would lead to noticeable inaccuracies. A method such as volume of fluid (VOF), where viscous flow calculations include free surface effects, would be necessary.

In an unpublished validation, the hybrid approach and VOF results are compared to measurements. The model scale resistance of 22 hulls is investigated. The study encompasses tankers, bulk carriers, container ships, and car carriers. These ships range from 150 to 350 meters in length, with block coefficients varying from 0.54 to 0.87. At their respective design speeds, the Froude numbers span from 0.14 to 0.24. In the hybrid approach, the total resistance coefficient, C_T, is composed of two components: the viscous component, C_V, calculated with the RANS method, and the wave resistance component, denoted as C_W, calculated with the potential flow method. Across all studied ships, at the design speed, the mean relative comparison error, $E_{mean}\%D$, is 0.3% for the hybrid and -0.2% for the VOF methods, respectively. The mean absolute relative comparison errors, $|E|_{mean}\%D$, are 1.6% for the hybrid and 1.4% for the VOF methods. Similarly, the relative standard deviations, $\sigma\%D$, are only slightly higher for the hybrid approach at 1.9% compared to 1.6% for VOF. Additionally, the maximum absolute relative comparison errors, $|E|_{max}\%D$, are similar for both methods, at 3.4% and 3.2%, respectively. The statistical data for design conditions are presented in Table 2.2.

Table 2.2: Statistics of total resistance coefficient at design speed evaluated with hybrid and VOF methods.

Method	$E_{mean}\%D$	$\lvert E\rvert_{mean}\%D$	$\lvert E\rvert_{max}\%D$	$\sigma\%D$
Hybrid	0.3	1.6	3.4	1.9
VOF	-0.2	1.4	3.2	1.6

Calculations were also carried out for speeds ranging from approximately 70% to 110% of the ships' design conditions. In Figure 2.1, examples of the total resistance coefficient are presented for four selected cases, each representing a different vessel type. For confidentiality reasons, exact values have been omitted, but error bars of $\pm 3\%$ are included to provide a visual reference. On average, the hybrid approach slightly overpredicts the total resistance, which is an acceptable result from a potential flow method that disregards the viscous effects.

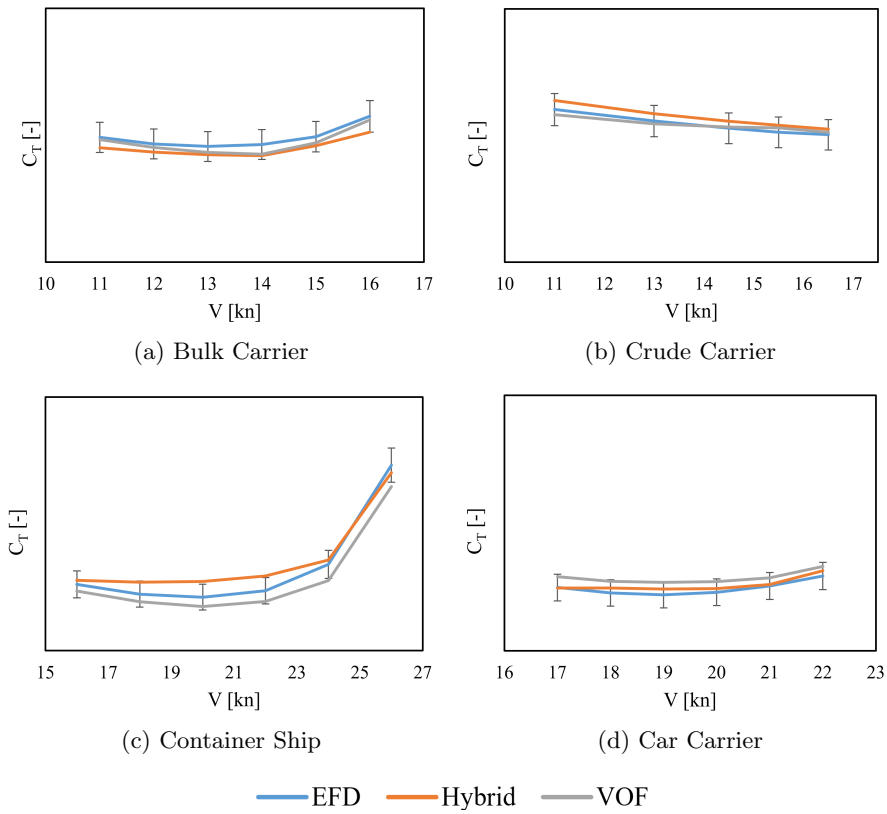

Figure 2.1: Examples of total resistance coefficient evaluated with different methods for four different ship types. Included error bars indicate ±3% range.

2.5.2 Propeller and free surface interactions

For the ships used in the validation described above, the propeller shaft is located between 1.0 and 1.5 propeller diameters below the free surface at the design draft. Additionally, the wave height near the propeller plane at the design speed is relatively low, suggesting that interactions between the free surface and the propeller are likely to be minimal. Although no specific comparisons have been conducted in this work, the computations using the hybrid method are consistent with the measurements. Several comparisons have been presented in Paper IV and Paper V. Figure 2.2 illustrates an example of the total nominal wake calculated by this method and corresponding measurements. The calculations accurately represent the flow features and velocity magnitude.

The propeller is modelled with a lifting line method which takes into account the non-uniform inflow. The computations are steady, resembling a propeller with an infinite number of blades. Therefore, the efficiency losses due to the pressure pulses and cavitation are not considered. It is assumed that these are not significant for cargo vessels at design conditions. The full-scale delivered power validation presented in Paper II and model scale predictions for a similar

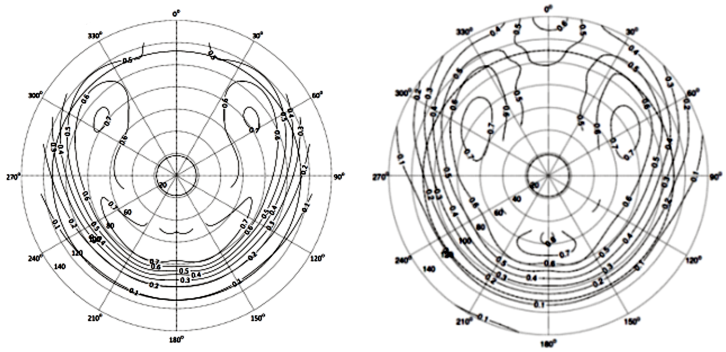

Figure 2.2: Total nominal wake at propeller plane for a VLCC, as presented in Paper V (Kim et al., 2014). Double-model RANS predictions to the left, and measurements to the right.

ship illustrated in Figure 2.3 suggest that the method is sufficiently accurate. Further encouraging results of delivered power predictions using the hybrid method, also including Energy Saving Devices, are presented in Paper IV and Paper V.

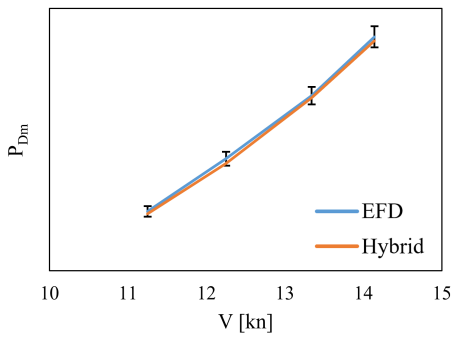

Figure 2.3: Delivered power at model scale evaluated with the hybrid method compared to measurements. Included error bars indicate ±3% range.

2.5.3 Ship motion effects

For the propulsion simulations in waves conducted in this work, the motion amplitude is relatively small. The studied case shows minor pitch and heave responses. This results in little change in propeller submergence and wake variation. In sea state 5 conditions at full scale, the maximum instantaneous vertical velocity of the shaft at the propeller plane induced by the motion of the ship is less than 1% of the blade velocity at 70% of the propeller radius. This estimate does not capture the complexity of the time-varying wake, yet it offers insight into the relatively minimal impact of ship motion on the average performance of the propeller in these conditions. This assumption is also

confirmed in a comprehensive study, where the steady, quasi-steady and fully unsteady approaches are compared (Saettone et al., 2020).

In the context of the specific conditions analyzed in this study, the effect of varying wake in waves on propeller cavitation and pressure pulses can be considered limited. According to another investigation focused on the KVLCC2 ship, it was observed that in short waves, the amount of cavitation does not vary significantly, and the increase in pressure pulses is limited (Taskar et al., 2016).

2.5.4 Aerodynamic resistance

The estimation of air resistance follows a method based on a regression formula (Fujiwara et al., 2005). While this approach may not be as accurate as wind tunnel tests or RANS simulations, it is recommended as a practical method for assessing the added resistance due to wind in weather factor predictions (ITTC, 2021a). The estimated air resistance at a speed of 13.5 knots in sea state 5 and Beaufort 6 conditions is nearly as large as the added resistance due to waves, amounting to 20% of the calm water ship resistance. Therefore, it should be noted that this simplification could lead to noticeable deviations in the calculated delivered power.

Chapter 3

Results

3.1 Verification

Verification is carried out to investigate the numerical uncertainty associated with the integral quantities predicted by the solvers. In this research, a method is adopted that utilizes a least-squares fit to account for variability or scatter in the solution, which is inevitable with complex numerical methods (Eça and Hoekstra, 2014). This process involves analyzing results from a series of geometrically similar grids to determine the order of accuracy, denoted as p, of the computational method and to quantify the discretization uncertainty associated with the solution, represented by U_G. The investigation encompassed the analysis of specific resistance components and propulsive factors at both model-scale and full-scale conditions. Due to the hybrid RANS and potential flow approach, the verification process is divided into numerical uncertainty estimations for the RANS solver and the effects of the potential flow solver results. It is essential to emphasize that the results for the potential flow part must be treated with caution. An inherent challenge is associated with refining the free surface spatial discretization in a potential flow panel method (Orych et al., 2021). It may lead to the point where breaking waves start appearing. This implies that the introduction of a new physical phenomenon, namely wave breaking, emerges within the solution, which is beyond the resolving capability of the potential flow method. Consequently, this leads to the divergence of the solver. The numerical uncertainty includes both the grid and the iterative uncertainties. However, simulations in this study are carried out with strict convergence criteria, ensuring that the iterative errors are negligible. A comprehensive investigation is detailed in the accompanying paper (Orych et al., 2021), while this summary includes only a single example of a full-scale simulation for a small tanker.

To quantify the wave resistance uncertainty associated with the potential flow solution, a series of six systematically refined meshes is prepared. The number of cells, i.e. the spatial resolution, is limited by the onset of wave breaking and, therefore, inevitable convergence issues. The resulting wave resistance from each mesh is combined with one selected RANS configuration

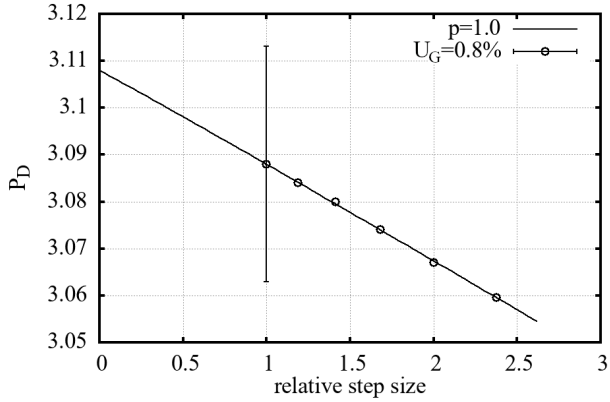

Figure 3.1: Potential flow mesh variation. Effect on delivered power.

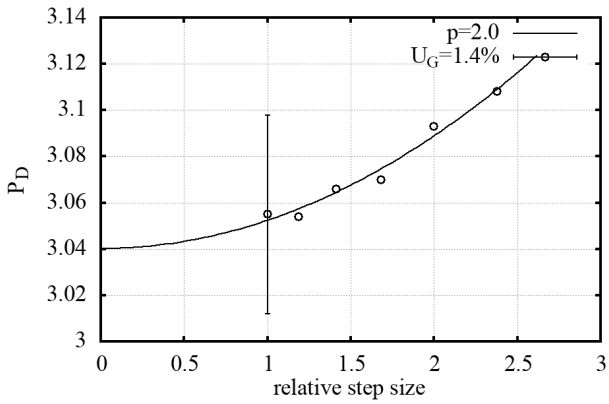

Figure 3.2: RANS grid convergence of delivered power, full-scale.

in the propulsion simulations. The delivered power, P_D, uncertainty due to the potential flow mesh size in this setup is below 1% for the finest mesh. See Figure 3.1.

When assessing the grid convergence for the RANS solver, the wave resistance is computed using the potential flow method with the finest mesh. Six geometrically similar, systematically refined volume grids are used. For the finest grid, the delivered power grid uncertainty denoted as $U_G\%S_1$, is 1.4%. The difference between the computed result and the value extrapolated to an infinitely fine grid, represented as $|P_{D1} - P_{D0}|\,\%P_{D0}$, is 0.49%.

The verification results illustrated here are for a smooth hull. Calculations incorporating hull roughness indicate that the roughness effects and the employed modelling approach do not increase the scatter in the solutions, and the uncertainties remain comparable.

3.2 Roughness modelling

The roughness effect is an essential aspect of the full-scale simulations since it affects the resistance of the ship and the inflow to the propeller. In the wall-resolved RANS solver, roughness is modelled by adjusting the boundary conditions for turbulent kinetic energy and its specific dissipation rate (Orych et al., 2022). Several roughness models were implemented in the solver: Hellsten (Hellsten, 1998), Knopp (Knopp et al., 2009), Aupoix – Nikuradse, and Aupoix – Colebrook (Aupoix, 2014). The performance of each model is tested at Reynolds numbers ranging from 6.9×10^6 to 2.89×10^9. Through a series of simulations involving flat plates and ship hulls, the most accurate model in terms of its ability to predict the resistance increase due to surface roughness is selected.

The topological characteristics of rough surfaces are often characterized by just a single parameter. In ship hydrodynamics, the Average Hull Roughness, *AHR*, is commonly used (Townsin et al., 1981). This metric represents the arithmetic average of the measured mean height of roughness at a number of locations on the hull. However, RANS solvers use the equivalent sand-grain roughness height, k_S, to normalize irregular and diverse rough surfaces. There is no universal correlation factor between the *AHR* and the k_S. One of the important investigations within this work is focused on selecting an appropriate conversion factor specifically for ship hulls.

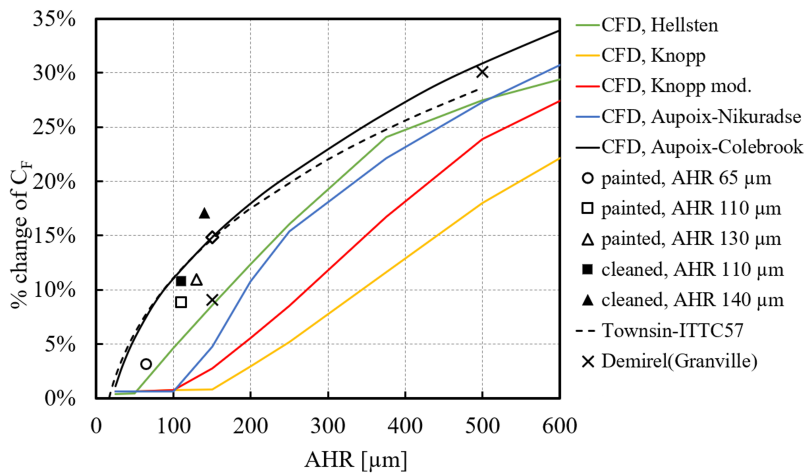

Figure 3.3: Comparison of CFD simulations ($AHR/k_S = 5$) with Granville/Grigson extrapolated rough flat plate measurements and Townsin estimated increase of C_F. KCS conditions, Lpp = 230 m, $Re = 2.89\times10^9$.

Here, model test data for flat plates is used to determine a suitable factor. The measurements of several painted surfaces are extrapolated to full-scale length with Granville's method and adjusted for relevant speeds with Grigson's method with the help of SSPA's Skin Friction Database tool (Leer-Andersen, 2020). Both freshly painted plates and those cleaned after deployment in

the sea are considered. Applying an AHR/k_S factor of 5 gives a satisfactory agreement between the extrapolated measurements and current simulations with the Aupoix-Colebrook model, as seen in Figure 3.3.

A similar factor applicable to *AHR* up to 150 µm has been reported earlier (Schultz and Flack, 2007). It is important to emphasize that the rough surface topology cannot be adequately represented by a single number. The same *AHR* may yield a different resistance increase depending on the surface texture. It should be noted that there is a significant difference in C_F between newly painted surfaces and those that have undergone cleaning post-sea exposure, even when they have comparable *AHR* values, as depicted in the figure.

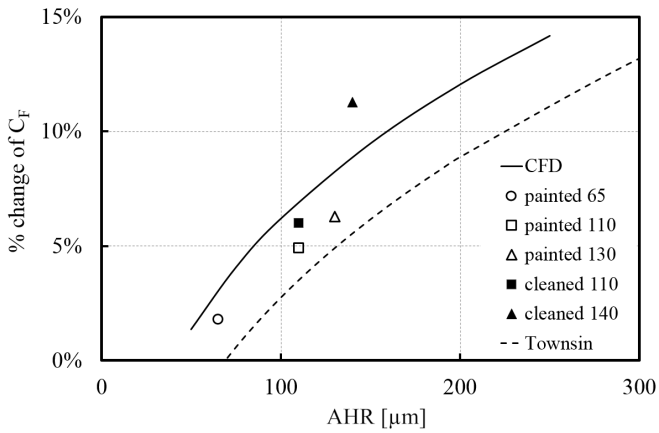

Figure 3.4: Comparison of CFD simulations ($AHR/k_S = 5$) with Granville/Grigson extrapolated rough flat plates and Townsin estimated increase of C_F. Current hull conditions, Lpp = 180 m, $Re = 9.7{\times}10^8$.

The added resistance due to roughness from the simulations conducted in this study is also compared to Townsin's approximation used in the ITTC extrapolation method (ITTC, 2017b). For a flat plate with length and speed corresponding to the KRISO Container Ship (KCS) (Larsson et al., 2015), the correlation between the Aupoix-Colebrook model (Aupoix, 2014) and Townsin's method is demonstrated to be very good, Figure 3.3. However, for a ship that is shorter and slower, the results are quite different, as depicted in Figure 3.4, where Townsin's formula appears to underestimate the roughness effect. This trend is even more evident if the length and the speed are decreased further. This highlights a notable limitation in the ITTC-78 extrapolation method. The roughness effects are not limited to friction alone; they also influence the viscous pressure resistance and the wake. For the KCS case, these three effects are illustrated in Figure 3.5.

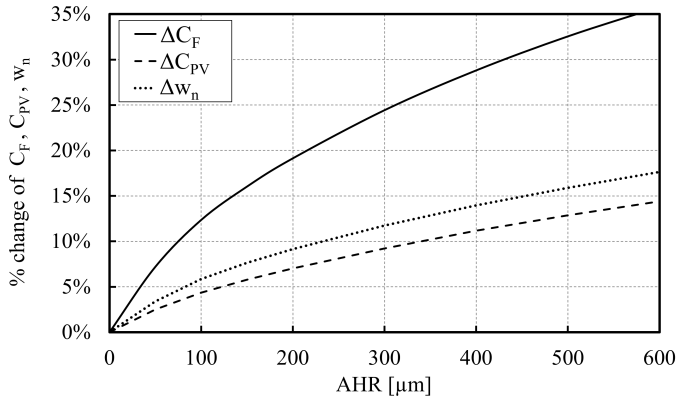

Figure 3.5: Resistance components and nominal wake increase due to roughness for KCS.

3.3 Full scale validation

It is remarkably difficult to obtain sea trial data from a shipyard or a shipowner. Securing high-quality materials with accurate measurements and detailed records of the procedure is even more challenging. In this case, the authors are fortunate to gain access to a well-documented set of measurements for 12 similar tankers.

The sea trials are conducted in accordance with the ITTC procedure (ITTC, 2017c), a method that is also incorporated into the ISO 15016 standard. Three power settings are included, and data is acquired for power, speed, propeller rate of revolution, wind, waves, current and temperature, among other parameters. Corrections are made for the effects of wind, waves, current, and temperature. In connection with the trial runs, the Average Hull Roughness is measured. Considering the conditions present at the time of these measurements, three sister vessels were selected for this validation study. These vessels are evaluated at design draught under nearly perfect weather conditions, thereby minimizing the errors in measurement and reducing the need for extensive corrections. The favourable conditions during the trial runs have ensured a low level of measurement uncertainty, thus providing a robust basis for the precise validation of the CFD simulations' accuracy. The validation of full-scale self-propulsion is conducted across a speed range of 12.5, 13.5, and 14.5 knots. This encompasses the range of speeds for which sea trial data are available for the selected vessels under investigation. In the computations, the roughness effects are considered, and the *AHR* is set to 100 μm, which reflects the average obtained from empirical measurements. The windage resistance is calculated using the frontal area of the ship and applying a resistance coefficient as recommended by the towing tank that conducted the model tests. Additionally, the drag contribution of the bilge keels is estimated by considering their wetted surface area along with the frictional resistance coefficient of the bare hull. The windage and bilge keel contributions are both accounted for as additional resistance

components during the self-propulsion simulation. To account for the propeller roughness, a value of 30 µm, as indicated by the ITTC extrapolation method, is used. The delivered power from the sea trials and SHIPFLOW simulations is presented in Figure 3.6.

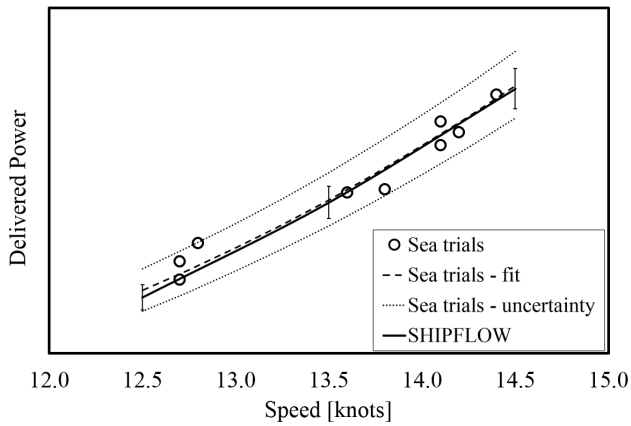

Figure 3.6: Delivered power for sea trials and CFD simulations.

The curve fitting of the sea trial data is done according to the ITTC recommendations (ITTC, 2017c). Thus, a curve representing the mean value of the two available towing tank full-scale predictions is shifted vertically such that the Root-Mean-Square (RMS) error of the sea trial data points is minimised. The Normalised RMS Error is 2.8%. Included in the plot are also the uncertainties estimated for the sea trials and the CFD results. A band of ±6.1% represents the experimental uncertainty, U_D, which can be expected from these sea trials. It is computed based on the sea trial uncertainties published earlier (Werner and Gustafsson, 2020), where, for acceptable weather conditions during trials, the precision uncertainty is 8% for each individual point. The uncertainty of the mean value is obtained by dividing by the square root of the number of sister ships (Farrance and Frenkel, 2012), resulting in a precision error, P, of 4.6% for this case. Furthermore the expected bias error, B, for delivered power, is about 4% (Insel, 2008). P and B can be combined to obtain $U_D = \sqrt{P^2 + B^2}$. Considering the computational effort, the fourth finest grid is used for validation. The difference in delivered power between the finest setup with over 44 million cells and the selected one with about 10 million cells is less than 0.5%. The numerical uncertainty associated with the delivered power, denoted as U_{SN}, is quantified at 3.65% for the selected grid size, which falls within an acceptable range for this type of simulation study. A computational simulation is considered validated at the U_{Val} level if the absolute comparison error, $|E|$, is less than the validation uncertainty, U_{Val} (ITTC, 2017d):

$$|E| < U_{Val} = \sqrt{{U_{SN}}^2 + {U_D}^2}$$

Table 3.1: Measurement uncertainty and differences between CFD simulations and sea trial data fit for delivered power.

Speed [knots]	P_D	
	$\|E\|\,\%D$	$U_{Val}\%D$
12.5	1.9	7.1
13.5	0.6	-
14.5	0.5	-

To assess the comparison error, E, for the validation, the differences between the computed results and the sea trial data are calculated. These differences are then expressed as a percentage of the sea trial data, D. The results of these calculations can be found in Table 3.1. The computed errors in delivered power are significantly smaller than the validation uncertainty, which allows us to consider the simulations validated at the U_{Val} level of 7.1%. It is worth noting that the numerical uncertainty is not only lower than the experimental uncertainty but is also encompassed by it, as seen in Figure 3.6.

3.4 Seakeeping

In marine hydrodynamics, the reduction in ship speed due to adverse sea conditions can be quantified by a non-dimensional weather factor, f_w. This factor is derived by comparing the speed of the ship in specified wave and wind scenarios to its speed in calm waters, both at identical delivered power. The ITTC guidelines (ITTC, 2021a) define the calculation of f_w in accordance with the 2014 Guidelines on the method of calculation of the attained energy efficiency design index (EEDI) for new ships, a methodology endorsed and further refined by the International Maritime Organization (IMO). Essentially, f_w serves as an indicator of how factors such as wave height, frequency, and wind speed can impact the speed of a ship operating at constant engine power.

In this hybrid Boundary Element Method (BEM)/RANS approach, the added resistance in waves is computed separately, and then the average resistance force is introduced into the RANS self-propulsion simulations. Additionally, the wind resistance is estimated using an empirical method (Fujiwara et al., 2005).

The KVLCC2 tanker serves as the test case in this part of the work. To estimate the accuracy of the seakeeping simulations, the computed added resistance coefficient in regular head waves is compared with the corresponding test data, as depicted in Figure 3.7. These tests were conducted at Maritime Dynamics Laboratory of SSPA and included multiple series across all wave lengths. The numerical results presented in this study are within the scatter found in the measurements, except for the longest waves in the series. This observation indicates that under the tested conditions, viscous effects have a minimal impact on added resistance in waves. The observed scatter in the measurement data, especially for shorter wave lengths, indicates potential

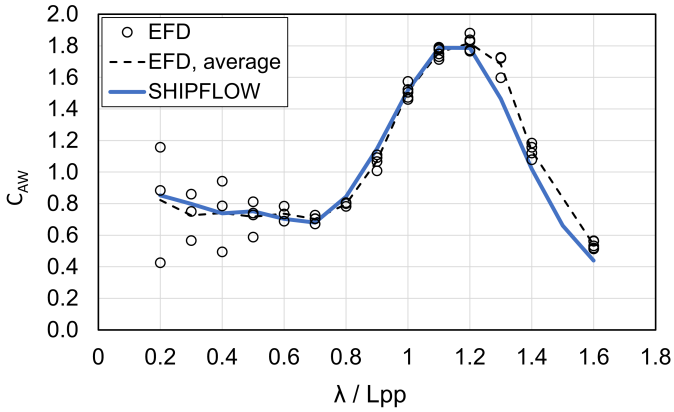

Figure 3.7: Coefficient of added resistance due to regular, head sea waves from simulations and multiple measurements.

experimental challenges due to significant fluctuations in the measured forces relative to their mean values.

To predict speed loss, the added resistance in waves across three speeds, 12.5, 13.5, and 14.5 knots, is computed. This is done for three wave directions: 0° (representing head waves), 30°, and 60°. The evaluations span a range of wave lengths, from 0.2 to 1.8 times the ratio of λ/L_{PP}. The mean resistance in irregular waves is determined by integrating the transfer function of the added resistance observed in regular waves with the specified wave spectrum. For short regular waves, specifically those below the $\lambda/L_{PP} = 0.2$ threshold, the response is estimated using the STAwave-II method (ITTC, 2021b). Capturing the effect of these short waves presents challenges in both model testing and simulations. However, they significantly influence the resulting resistance in irregular waves and have to be taken into account. When calculating the weather factor, the ITTC spectrum is used, with a significant wave height, H_S, set at 3.0 m and a zero up-crossing period, T_Z, of 6.16 s. When plotting this spectrum alongside C_{AW}, it becomes evident that, for this particular sea state, the wave energy is predominantly concentrated in the region spanning 0.1 to 0.8 λ/L_{PP}. Consequently, the mean added resistance attributed to the waves will be primarily influenced by wave reflection and diffraction rather than by radiation, which relates to the motion-induced resistance.

The weather factor, denoted as f_w, represents the proportion of calm water speed a ship can maintain when faced with Beaufort 6 weather conditions and the associated waves (Gerhardt and Kjellberg, 2017). To estimate this factor, one must predict the power in both calm water and waves. The resistance due to the waves and the apparent wind is incorporated as an external force in the self-propulsion simulations. The delivered power is computed for both scenarios, and the speed loss corresponding to the given P_D is determined, as illustrated in Figure 3.8.

In the present analysis, the weather factor is 0.88. This value is roughly 6.5% greater than the conservative standard curve for the weather factor in

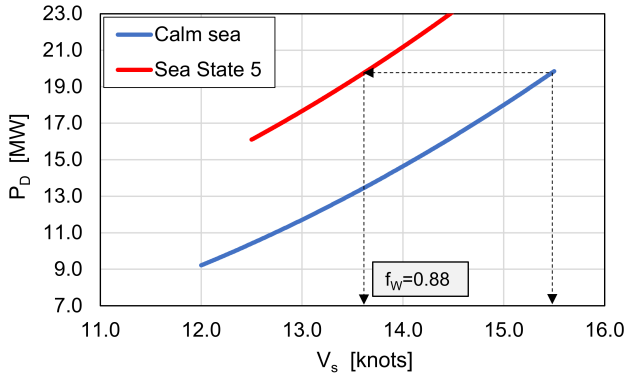

Figure 3.8: Speed-power curves for calm water and in State 5 head seas with Beaufort 6 wind.

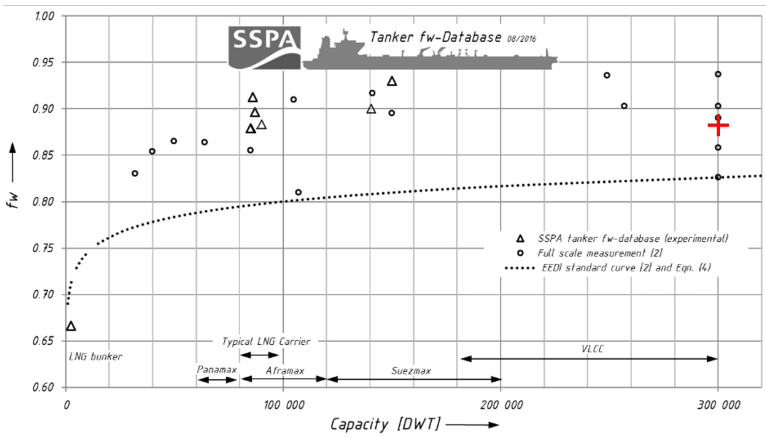

Figure 3.9: f_w database for tankers, (Gerhardt and Kjellberg, 2017). The result from the current method is marked with red "+" symbol.

EEDI, which encapsulates the impacts of both wind and waves on the energy efficiency of a vessel (IMO, 2012). Furthermore, the outcome of the simulation closely aligns with the tanker database from SSPA, as depicted in Figure 3.9.

3.5 Energy Saving Devices

The hydrodynamic effects of Energy Saving Devices (ESDs) are often studied at the model scale Reynolds number in towing tanks. The performance of ships with ESDs at full scale is typically evaluated using extrapolation methods, such as the ITTC-78 (ITTC, 2017a), with additional wake scaling correction discussed by ITTC in 1999. However, the local flow details at the model scale can differ significantly from those at full scale, particularly in the wake region where the ESDs are positioned. Therefore, a simple wake scaling modification

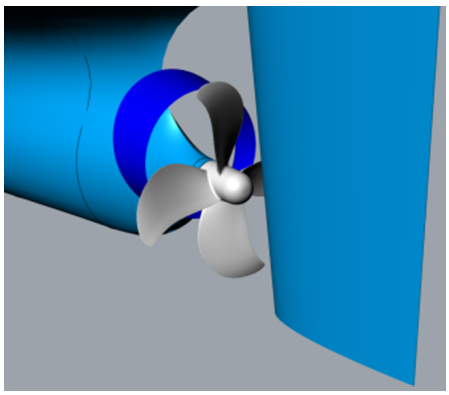

(a) Wake equalizing duct (Duct)

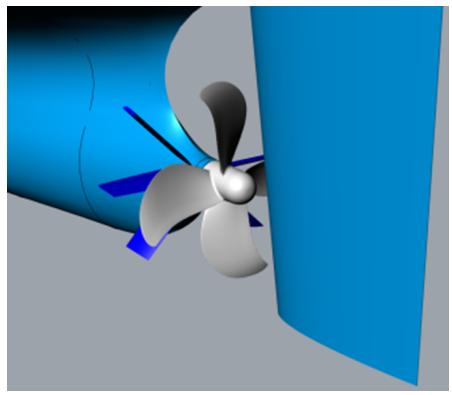

(b) Pre-swirl stator (PSS)

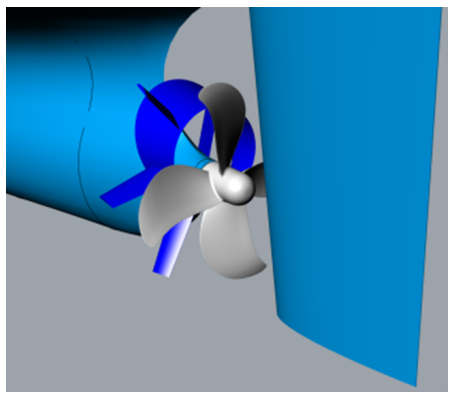

(c) SSPA generic ESD (GKD)

Figure 3.10: Rendered views of investigated Energy Saving Devices

may not reflect all the differences. As a result, predictions might not always be accurate, and the power savings attributed to the ESDs can sometimes be overstated. The hydrodynamics of various devices is examined to understand their working principles and optimize them for peak efficiency at full scale. The investigation includes an analysis of a duct, a pre-swirl stator, and their integrated designs shown in Figure 3.10(a), 3.10(b), and 3.10(c). Verification and validation are carried out to increase confidence in the results.

In this study, a very large crude carrier (VLCC) is used. A reference computation is conducted for the bare hull. The predicted thrust, torque, and propeller rate of revolutions at the model scale for the reference case are compared with the measured data. The prediction accuracy is high, with comparison errors being 1.3% for the torque (Q) and 0.8% for the number of revolutions (n). Although examining power at model scale is uncommon, it is utilized for benchmarking purposes. The resulting comparison error is 0.45%. The PSS configuration, which includes four stator blades, and the duct solutions

are both examples of designs that have been optimized with the support of towing tank measurements. By combining the benefits of both configurations, an alternative is introduced under the name SSPA generic ESD. In this summary, the focus is exclusively on the final versions optimized for the model scale (denoted as GKDm) and full scale (denoted as GKDf). A comprehensive description, including the design methodology, can be found in the appended papers (Kim et al., 2012; Kim et al., 2014). The fundamental principle behind the energy-saving capabilities of ducts lies in enhancing propulsion efficiency through the uniformity of propeller inflow. Concurrently, these devices aim to reduce the total drag of the ship by decreasing hull resistance and/or generating thrust through their special configurations.

In this study, the duct decreases the overall resistance by 1.4% and the delivered power by 4.3% at the model scale. This effect arises from the acceleration of the flow and the delay of potential separation, particularly evident at the model scale. The duct generates a small forward thrust component capable of overcoming its resistance when the angle of attack is advantageous. However, the effect of the duct is highly dependent on the development of the boundary layer. At full-scale Reynolds numbers, the boundary layer becomes thinner and more stable, which could reduce the extent or likelihood of flow separation. The duct then encounters fluid with a higher velocity, and the flow direction changes slightly. This may not be optimal for a duct designed for model scale. There is a noticeable increase in the resistance of the duct, and the benefits of reduced separation become less pronounced. Consequently, the advantages gained from the duct diminish.

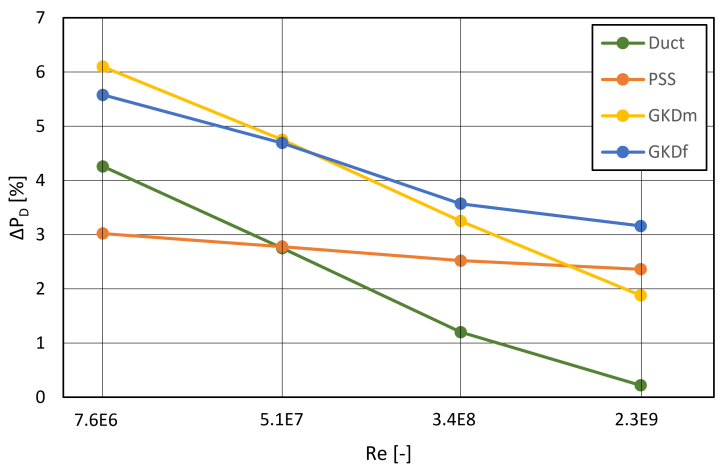

Figure 3.11: Power reduction by Duct, PSS and optimized GKD at different Reynolds numbers.

The gain in propulsion efficiency achieved with a PSS can be attributed to two factors: the increased wake fraction and the counter-rotating pre-swirl flow. These elements cause an increase in the angle of attack of inflow to the propeller. Fitting a PSS is observed to result in an increase in resistance,

measured at 0.45% at model scale and 2.74% at full scale in the current analysis. The increase in drag resulting from including a PSS represents an unfavourable effect, one that should be counterbalanced by improvement of propulsion efficiency. By increasing the angle of attack on the propeller, it can deliver the same thrust at a reduced rate of revolution. The computation at the model scale shows 3% power reduction compared to the bare hull. At full scale, the delivered power is reduced by 2.4%, indicating that the PSS is less susceptible to scale effects than the duct.

The GKD design aims at combining the advantageous hydrodynamic effects of both a duct and a pre-swirl stator. In the model scale simulations, the GKD outperforms the other two devices by 2-3%. The scale effects observed with the GKD are similar to those experienced with the duct, with the reduction in delivered power at full scale being marginally higher than that observed with the PSS alone. However, an additional benefit of the GKD configuration is the increased structural integrity. A comparison of the delivered power decrease due to the PSS, the Duct, the GKDm and GKDf for a range of Reynolds numbers is shown in Figure 3.11. The significant disadvantage of the duct is clearly visible. It is important to note that a slight additional improvement in performance can be obtained for both devices at higher Reynolds numbers by optimizing their geometries. However, the larger sensitivity of the duct to scale effects remains. Although the performance gain of the GKD decreases similarly to the duct, this is offset by the additional advantages of the pre-swirl component.

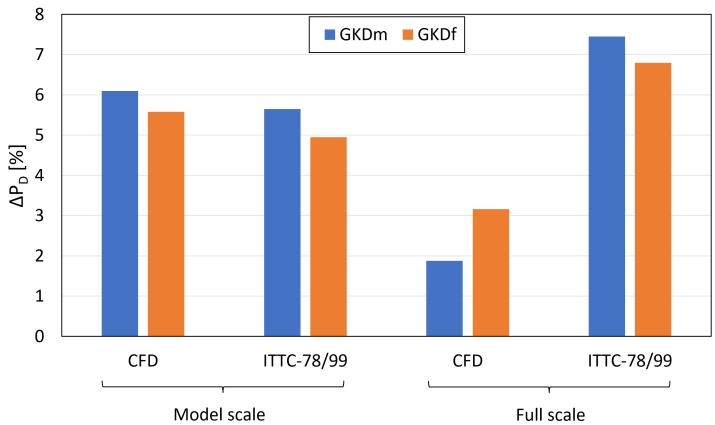

Figure 3.12: Power reduction estimated by model tests and CFD for GKDm and GKDf.

Based on the evaluation of power reduction and a detailed analysis of flow characteristics, the GKDm and GKDf were selected for physical testing. Scaled models of the ship, propeller, and GKD were manufactured, and tests were conducted at SSPA's towing tank. Comparative measurements were conducted under design conditions. The test methods and calculation principles for resistance and self-propulsion tests followed the ITTC-78 method. This also

incorporated the modified wake scaling for pre-swirl stators, as suggested by the Specialist Committee on Unconventional Propulsors during the 21st ITTC in 1999. The power reduction resulting from the ESD installation is illustrated in Figure 3.12. Extrapolation of the model test results suggests a power reduction that is much higher than what the CFD simulations and sea trial experiences indicate. Given the challenges associated with accurately predicting the full-scale performance of energy-saving devices from model tests alone, it is highly recommended to conduct comprehensive full-scale CFD simulations to evaluate the performance of ships equipped with ESDs.

Chapter 4

Summary of Included Papers

4.1 Paper I

M. Orych, S. Werner, L. Larsson. (2022). Roughness effect modelling for wall resolved RANS – Comparison of methods for marine hydrodynamics. *Ocean Engineering,* 266. https://doi.org/10.1016/j.oceaneng.2022.112778

Division of work

All authors participated in stating the aim and the scope of the paper. The literature study, selection of suitable models, implantation in the RANS code, simulations, post-processing, analysis of the results and original draft writing were done by M. Orych. All authors were involved in reviewing and correcting the manuscript.

Motivation and Aim

Considering roughness effects is crucial in full-scale numerical simulations, as hulls are not hydraulically smooth, even when brand new. The objective of this work is to identify and implement an appropriate roughness model for a wall-resolved RANS solver, and to establish a suitable correlation between the average hull roughness and the equivalent sand-grain roughness height for this model.

Results and Contribution

In this work, five roughness models are implemented within the CFD code. These are evaluated using three test cases: a flat plate at both model and full-scale Reynolds numbers and a ship hull. The Aupoix-Colebrook formulation yields the most promising results, demonstrating consistent performance across the full range of Reynolds numbers for all test cases. An investigation into the

correlation between Average Hull Roughness and equivalent sand roughness height indicates that a value of five is appropriate for moderate roughness heights, which are typical for well-maintained ships. This work contributes to the field by suggesting a roughness model and establishing a correlation between average hull roughness and equivalent sand roughness height, which are suitable for application in numerical ship hydrodynamics using wall-resolved RANS solvers.

4.2 Paper II

M. Orych, S. Werner, L. Larsson. (2021). Validation of full-scale delivered power CFD simulations. *Ocean Engineering,* 238. https://doi.org/10.1016/j.oceaneng.2021.109654

Division of work

All authors participated in stating the aim and the scope of the paper. S. Werner provided the validation case. The simulations, post-processing, analysis of the results and original draft writing were done by M. Orych. All authors were involved in reviewing and correcting the manuscript.

Motivation and Aim

Numerical simulations at model scale are well-established for resistance and self-propulsion applications, supported by the extensive availability of experimental data that is publicly accessible. However, access to sea-trial results is often limited due to confidentiality concerns. Another challenge lies in the data quality, which may be compromised by the demanding and uncertain conditions of collection outside the well-controlled laboratory environment. This paper presents the verification and validation of full-scale self-propulsion CFD simulations against carefully selected sea-trial results, with the main aim of demonstrating the reliability of the CFD method.

Results and Contribution

The verification of the numerical method is demonstrated through systematic grid refinement studies for both model-scale and full-scale simulations. Numerical uncertainties have been quantified for total resistance and its components, propulsive factors, and delivered power. When using a grid comprising ten million cells, the numerical uncertainty associated with the delivered power is 2.3% for model-scale simulations and 3.7% for full-scale simulations. In the full-scale validation, special emphasis is placed on assessing the impact of surface roughness on the accuracy of the simulations. The validation relies on sea trial results, with the experimental uncertainty estimated at 6%. For the speed range of 12.5 to 14.5 knots, the average comparison error is found to be 1%, which is considerably smaller than the validation uncertainty of 7%—a figure that includes both numerical and experimental uncertainties. The paper underscores the reliability and accuracy attainable in full-scale CFD simulations, thereby increasing confidence in the presented method.

4.3 Paper III

M. Orych, M. Östberg S., M. Kjellberg, S. Werner, L. Larsson. (2023). Speed and delivered power in waves—Predictions with CFD simulations at full scale. *Ocean Engineering,* 285. https://doi.org/10.1016/j.oceaneng.2023.115289

Division of work

All authors participated in the conceptualisation, the development of the methodology, and the review and editing of this paper. M. Kjellberg and M. Östberg implemented the seakeeping code. The original draft was written by M. Orych except for the description of the numerical method for the seakeeping code which was written by M. Östberg. All authors participated in testing and validating the code. The simulations, post-processing, and analysis of the results were done by M. Orych.

Motivation and Aim

One of the critical aspects in selecting an engine capable of ensuring safe and efficient ship navigation is the consideration of incoming wave and wind-added resistance components. Although full-scale self-propulsion simulations with incoming waves are feasible using state-of-the-art unsteady RANS codes, they remain time-consuming and costly due to significant computational demands as of the time this paper is written. The aim of this paper is to establish a procedure for estimating the required power or speed loss for a ship sailing in waves, potentially bridging the gap between the rapid, simple methods commonly employed and the more complex, unsteady RANS simulations. The proposed procedure includes two main steps: initially, it involves calculating the added resistance in waves utilizing a newly developed non-linear, unsteady potential flow solver tailored for free surface flows with floating bodies under six degrees of freedom (6DOF) conditions. Subsequently, it integrates these calculations with self-propulsion simulations performed using a steady RANS code.

Results and Contribution

The numerical results for resistance, delivered power, and added resistance in waves are accurate when compared to the experimental data. Under the conditions considered, comparison errors for both resistance and delivered power are around 1%. Additionally, the estimated weather factor shows consistency with the results from sea trials of similar vessels. However, when dealing with larger waves, it might be important to account for potential accuracy challenges brought about by the time-varying wake, propeller submergence, and loading. Within the constraints of the inherent approximations, the presented method maintains accuracy and provides a faster alternative to unsteady RANS simulations.

4.4 Paper IV

K. Kim, M. Leer-Andersen, S. Werner, M. Orych, Y. Choi. (2012, August). Hydrodynamic Optimization of Pre-swirl Stator by CFD and Model Testing. *29th Symposium on Naval Hydrodynamics, Gothenburg, Sweden*

Division of work

All authors participated in the conceptualisation, the development of the methodology, and the review and editing of this paper. S. Werner evaluated the model test experiments. The literature study, post-processing, visualisation and writing of the original draft were performed by the first author. Both the first author and M. Orych prepared the CFD configuration and executed the computations.

Motivation and Aim

As the global maritime industry experiences mounting pressures from environmental concerns and economic challenges, there is a growing urgency to enhance the efficiency of ships. Fuel consumption remains one of the highest operational costs for ship owners and contributes directly to greenhouse gas emissions. By improving the efficiency of the propulsive system, not only can ships reduce their operational costs but also make a tangible contribution to environmental sustainability. The primary focus of this work is to present the developmental stages of a pre-swirl stator (PSS) as an energy-saving device. Beginning with the evaluation of the initial design, a CFD-based approach is used, followed by a transition to the optimization phase. During this phase, adjustments are made to the number of blades, their span, angular position, and angle of attack. This computational methodology is benchmarked against empirical results, with model test confirmations and subsequent validation via sea trial evaluations.

Results and Contribution

This study of the hydrodynamic effects of PSS shows that the significant propulsion efficiency gain from the PSS is largely due to the increased angle of attack on the propeller blades. This benefit is further amplified by the increase in wake fraction and the inception of a counter-rotating pre-swirl flow generated by the PSS. An important observation was that the working propeller profoundly affects the flow over the PSS, emphasising the importance of self-propulsion simulations in designing and evaluating energy-saving devices. For the investigated PSS design, computational results indicate an approximate power decrease of 4% relative to the baseline configuration, with model testing showing an efficiency improvement of about 5.7%. Subsequent full-scale assessments confirmed the consistent hydrodynamic benefits of the PSS. This research contributes to the maritime community by presenting a viable approach for the design optimization of pre-swirl stator (PSS) devices through comprehensive CFD simulations.

4.5 Paper V

K. Kim, M. Leer-Andersen, M. Orych. (2014, November). Hydrodynamic Optimization of Energy Saving Devices in Full Scale. *30th Symposium on Naval Hydrodynamics, Hobart, Tasmania, Australia*

Division of work

All authors participated in the conceptualisation, the development of the methodology, and the review and editing of this paper. The first author performed the literature study, post-processing, visualisation, and writing of the original draft. The first author and M. Orych performed the CFD configuration and computations.

Motivation and Aim

Energy Saving Devices (ESD) are commonly evaluated at model scale in towing tanks; however, the flow characteristics at this scale may significantly differ from those at full scale, particularly within the wake region. Consequently, considerable discrepancies often emerge between the predicted power savings from model-scale tests and the actual performance, underscoring the challenges of accurately replicating full-scale flow characteristics in smaller-scale environments. A significant challenge arises from the scarcity of readily accessible and reliable full-scale data, attributed to limited operational experience with these devices, the inaccuracies inherent in full-scale measurements, and the lack of transparency concerning actual operational savings. Computational Fluid Dynamics (CFD) emerges as a promising approach to bridge this gap, offering a means to evaluate full-scale performance accurately. This study aims to highlight the effects of scaling and describe a development process that employs numerical simulations to refine ESD designs. The methodology is designed to optimize ESD development using CFD methods supported by model scale validations.

Results and Contribution

The findings of the study highlight a substantial discrepancy between the efficiency of Energy Saving Devices (ESDs) in model-scale conditions compared to full-scale conditions. This variation is attributed to the dependency on the Reynolds number, which affects the performance of ESDs. Furthermore, the difference in efficiency changes depending on the type of Energy Saving Device (ESD) used. The research contributes valuable insights into the hydrodynamic effects of ESDs over a range of Reynolds numbers, spanning from model to full scale. A clear understanding of these differences is crucial for the design and testing of more reliable ESDs in future research projects. Additionally, the study emphasizes the importance of full-scale Computational Fluid Dynamics (CFD) simulations, highlighting their role in advancing the field.

Chapter 5

Conclusions and Future Work

This research work aims to introduce a methodology capable of delivering accurate and fast predictions of power requirements for ships sailing in both calm waters and waves. A hybrid approach is presented that combines steady free-surface potential flow, unsteady potential flow in waves, and steady RANS self-propulsion simulations at full scale. On average, simulations in waves require approximately 1.5 hours per case, and self-propelled cases take about 2 hours each, when utilizing a single computer equipped with a 24-core CPU. Assuming that the assessment of speed loss involves computing added resistance for eight different wave lengths, and executing six self-propelled cases to estimate the delivered power, the total computational time amounts to approximately one day. The time required for the same simulations using unsteady RANS is significantly longer.

The initial model scale validation study, which includes tankers, bulk carriers, container ships, and car carriers, shows that the mean absolute relative comparison error of the resistance is 1.6% for the hybrid approach and 1.4% for the VOF method. Full-scale, calm water self-propulsion predictions for the case detailed in Paper II indicate that the delivered power can be predicted with comparison errors not exceeding 2%. Moreover, this error is considerably lower than the validation uncertainty, which is quantified at 7.1%, with the numerical uncertainty contribution being 3.65% according to the verification study. The added resistance in waves, as presented in Paper III, shows that the average comparison error for wave lengths ranging from 0.2 to 1.0 of the ship length, is 3% relative to the averaged measurements. This is significantly lower than the standard deviation of the measurements, which averages 11% and varies from 1% to 37% in the corresponding range. These results suggest that the selected approach is robust and sufficiently accurate for both model and full-scale simulations to provide useful results across a practical range of applications.

Defining strict limits of application for the hybrid approach presents a significant challenge. Establishing the boundaries within which the method

remains reliable and valid requires expertise. Users must possess the capability to interpret the data, recognize potential anomalies, and understand the constraints of the method under various conditions.

The proposed method could be further improved or extended in several areas to provide reliable results for a broader range of applications. The included propeller model, which is based on lifting line theory, performs well for the presented cases. However, its application to conditions far from the design loading will result in decreased accuracy. Additionally, further development is required for ships with ducted propellers. Another critical area is seakeeping. While the current method demonstrates robustness and accuracy in estimating ship motion and added resistance in moderate wave conditions, further enhancements are required to improve its reliability in conditions with steeper waves and larger amplitude ship motions.

Bibliography

Abdel-Maksoud, M., Hellwig, K., & Menter, F. R. (2000). Calculation of the turbulent flow around a model and full scale VLCC ship hull. *A Workshop on Numerical Ship Hydrodynamics. Chalmers University of Technology, Gothenburg.*

Aupoix, B. (2014). Wall roughness modelling with $k-\omega$ SST model. *10th International ERCOFTAC Symposium on Engineering Turbulence Modelling and Measurements.* https://onera.hal.science/hal-01071701

Bhushan, S., Xing, T., Carrica, P., & Stern, F. (2009). Model- and full-scale URANS simulations of Athena resistance, powering, seakeeping, and 5415 maneuvering. *Journal of Ship Research*, *54*(4), 179–198.

Broberg, L., Zhang, D.-H., Larsson, L., & Schöön, J. (1991). SHIPFLOW predictions of the flow around two tanker sterns. *Proceedings of 1990 SSPA-CTH-IIHR Workshop.*

Castro, A. M., Carrica, P., & Stern, F. (2011). Full scale self-propulsion computations using discretized propeller for the KRISO container ship KCS. *Computers & Fluids*, *51*, 35–47.

Chakravarthy, S., & Osher, S. (1985). A new class of high accuracy TVD schemes for hyperbolic conservation laws. *23rd Aerospace Sciences Meeting, Reno, NV, U.S.A., AIAA paper No*, *85-0363.*

Coslovich, F., Kjellberg, M., Östberg, M., & Janson, C.-E. (2021). Added resistance, heave and pitch for the KVLCC2 tanker using a fully nonlinear unsteady potential flow boundary element method. *Ocean Engineering*, *229*. https://doi.org/https://doi.org/10.1016/j.oceaneng.2021.108935

Deng, G. B., Queutey, P., & Visonneau, M. (2005). Three-dimensional flow computation with Reynolds Stress and Algebraic Stress Models. *Proceedings of the ERCOFTAC International Symposium on Engineering Turbulence Modelling and Measurements; ETMM6, Sardinia, Italy, 23–25 May, 2005*, 389–398.

Deng, G. B., & Visonneau, M. (2000). Comparison of explicit algebraic stress models and second-order turbulence closures for steady flows around the KVLCC2 ship at model and full scales. *A Workshop on Numerical Ship Hydrodynamics. Chalmers University of Technology, Gothenburg.*

Dick, E., & Linden, J. (1992). A multigrid method for steady incompressible navier-stokes equations based on flux difference splitting. *International Journal for Numerical Methods in Fluids*, *14*, 1311–1323.

Ducrozet, G., Engsig-Karup, A. P., Bingham, H. B., & Ferrant, P. (2014). A non-linear wave decomposition model for efficient wave-structure interaction. part a: Formulation, validation and analysis. *Journal of Computational Physics*, *257*, 863–883.

Eça, L., & Hoekstra, M. (1997). Numerical calculations of ship stern flows at full-scale reynolds numbers. *21st Symposium on Naval Hydrodynamics, Trondheim, Norway, June 24–28, 1996*.

Eça, L., & Hoekstra, M. (2001). Numerical prediction of scale effects in ship stern flows with eddy-viscosity turbulence models. *23rd Symposium on Naval Hydrodynamics, Val de Reuil, France, September 17–22, 2000*.

Eça, L., & Hoekstra, M. (2014). A procedure for the estimation of the numerical uncertainty of CFD calculations based on grid refinement studies. *Journal of Computational Physics*, *262*, 104–130.

Farrance, I., & Frenkel, R. (2012). Uncertainty of measurement: A review of the rules for calculating uncertainty components through functional relationships. *Clin. Biochem. Rev.*, *33*, 49–75.

Fujiwara, T., Ueno, M., & Ikeda, Y. (2005). A new estimation method of wind forces and moments acting on ships on the basis of physical component models. *J. JASNAOE*, *2*.

Gerhardt, F. C., & Kjellberg, M. (2017). Determining the EEDI 'weather factor' fw. *Influence of EEDI on Ship Design & Operation, 13 September 2017, London*.

Hänninen, S., & Mikkola, T. (2006). Computation of ship-hull flows at model- and full-scale Reynolds numbers. *EFFORT Repoert*.

Hellsten, A. (1998). Some improvements in Menter's $k-\omega$ SST turbulence model. *29th AIAA Fluid Dynamics Conference, Albuquerque, New Mexico, June 15-18, 1998*, 1–11.

Hess, J. L., & Smith, A. M. O. (1964). Calculation of nonlifting potential flow about arbitrary three-dimensional bodies. *Journal of Ship Research*, *8*(04), 22–44. https://doi.org/10.5957/jsr.1964.8.4.22

IMO. (2012). Interim guidelines for the calculation of the coefficient f_w for decrease in ship speed in a representative sea condition for trial use. *IMO Circular MEPC.1/Circ.796*.

Insel, M. (2008). Uncertainty in the analysis of speed and powering trials. *Ocean Engineering*, *35*, 1183–1193.

ITTC. (2017a). 1978 ITTC Performance Prediction Method. *ITTC – Recommended Procedures and Guidelines*, *7.5-02-03-01.4*.

ITTC. (2017b). Final Report and Recommendations to the 25th ITTC. *Proceedings of 25th ITTC, Fukuoka, Japan*.

ITTC. (2017c). Preparation, conduct and analysis of speed/power trials. *ITTC – Recommended Procedures and Guidelines*, *7.5-04-01-01.1*.

ITTC. (2017d). Uncertainty analysis in CFD verification and validation methodology and procedures. *ITTC – Recommended Procedures and Guidelines*, *7.5-03-01-01*.

ITTC. (2021a). Calculation of the weather factor f_w for decrease of ship speed in wind and waves. *ITTC – Recommended Procedures and Guidelines*, *7.5-02-07-02.8*.

ITTC. (2021b). Preparation, conduct and analysis of speed/power trials. *ITTC – Recommended Procedures and Guidelines, 7.5-04-01-01.1.*

Janson, C.-E. (1997). *Potential flow panel methods for the calculation of free-surface flows with lift.* PhD Thesis, Chalmers University of Technology.

Janson, C.-E., & Spinney, D. (2004). A comparison of four wave cut analysis methods for wave resistance prediction. *Ship Technology Research, 51*(4), 173–184. https://doi.org/10.1179/str.2004.51.4.004

Jasak, H., Vukčević, V., Gatin, I., & Lalović, I. (2019). CFD validation and grid sensitivity studies of full scale ship self propulsion. *International Journal of Naval Architecture and Ocean Engineering, 11*(1), 33–43. https://doi.org/10.1016/j.ijnaoe.2017.12.004

JoRes. (2023). *Joint research project.* Retrieved November 21, 2023, from https://jores.net.

Kim, K., Leer-Andersen, M., & Orych, M. (2014). Hydrodynamic optimization of energy saving devices in full scale. *30th Symposium on Naval Hydrodynamics, Hobart, Tasmania, Australia.*

Kim, K., Leer-Andersen, M., Werner, S., Orych, M., & Choi, Y. (2012). Hydrodynamic optimization of pre-swirl stator by CFD and model testing. *29th Symposium on Naval Hydrodynamics Gothenburg, Sweden.*

Kjellberg, M., Gerhardt, F., & Werner, S. (2022). Sailing in waves : A numerical method for analysis of seakeeping performance and dynamic behavior of a wind powered ship. *SNAME 24th Chesapeake Sailing Yacht Symposium, CSYS 2022.*

Knopp, T., Eisfeld, B., & Calvo, J. B. (2009). A new extension for $k-\omega$ turbulence models to account for wall roughness. *International Journal of Heat and Fluid Flow, 30*(1), 54–65. https://doi.org/https://doi.org/10.1016/j.ijheatfluidflow.2008.09.009

Larsson, L., Patel, V. C., & Dyne, G. (1991). Ship viscous flow. *Proceedings of 1990 SSPA-CTH-IIHR Workshop.*

Larsson, L., Stern, F., & Bertram, V. (2000). *A Workshop on Numerical Ship Hydrodynamics. Chalmers University of Technology, Gothenburg.*

Larsson, L., Stern, F., Visonneau, M., Hino, T., Hirata, N., & Kim, J. (2015). Proceedings, Tokyo 2015 Workshop on CFD in Ship Hydrodynamics.

Leer-Andersen, M. (2020). Skin friction database, https://www.sspa.se/en/skin-friction-database.

Menter, F. (1993). Zonal two equation $k-\omega$ turbulence models for aerodynamic flows. In *23rd fluid dynamics, plasmadynamics, and lasers conference.* https://doi.org/10.2514/6.1993-2906

Merci, B., Vierendeels, J., Reimslaugh, K., & Dick, E. (1985). Computational treatment of source terms in two-equation turbulence models. *AIAA Journal, 38*(11).

Mikkelsen, H., & Steffensen, M. (2016). *Full scale validation of CFD model of self-propelled ship.* MSc Thesis. DTU.

Mola, A., Heltai, L., & DeSimone, A. (2017). Wet and dry transom stern treatment for unsteady and nonlinear potential flow model for naval hydrodynamics simulations. *J. Ship Res., 61*, 1–14.

Murakami, N., & Hino, T. (2017). Validation of full-scale ship CFD simulation by the direct comparison with sea trials results. *Proceedings of the Japan Society of Naval Architects and Ocean Engineers Conference, Japan*.

Orych, M., Östberg, M., Kjellberg, M., Werner, S., & Larsson, L. (2023). Speed and delivered power in waves—predictions with CFD simulations at full scale. *Ocean Engineering*, *285*. https://doi.org/10.1016/j.oceaneng.2023.115289

Orych, M., Werner, S., & Larsson, L. (2021). Validation of full-scale delivered power CFD simulations. *Ocean Engineering*, *238*. https://doi.org/10.1016/j.oceaneng.2021.109654

Orych, M., Werner, S., & Larsson, L. (2022). Roughness effect modelling for wall resolved RANS – comparison of methods. *Ocean Engineering*, *266*. https://doi.org/10.1016/j.oceaneng.2022.112778

Pena, B., Muk-Pavic, E., Thomas, G., & Fitzsimmons, P. (2020). An approach for the accurate investigation of full-scale ship boundary layers and wakes. *Ocean Engineering*, *214*. https://doi.org/https://doi.org/10.1016/j.oceaneng.2020.107854

PETSc. (2020a). PETSc documentation, preconditioners.

PETSc. (2020b). PETSc documentation, solvers.

PETSc. (2020c). PETSc web page, https://www.mcs.anl.gov.

Ponkratov, D. (2017). 2016 workshop on ship scale hydrodynamic computer simulations. *Proceedings: Lloyd's Register's full-scale numerical modelling workshop*.

Ponkratov, D., & Zegos, C. (2015). Validation of ship scale CFD self-propulsion simulation by the direct comparison with sea trials results. *Proceedings: Fourth International Symposium on Marine Propulsors SMP'15, Austin, Texas, USA*.

Raven, H. C., & Hoekstra, M. (1985). A parabolised navier-stokes solution method for ship stern flow calculations. *2nd International Symposium on Ship Viscous Resistance, Gothenburg, Sweden, March 1985*.

Raven, H. C., van der Ploeg, A., Starke, A. R., & Eça, L. (2008). Towards a CFD-based prediction of ship performance - progress in predicting full-scale resistance and scale effects. *Transactions of the RINA, Part A: International Journal of Maritime Engineering*, *150*, 31–42.

Raven, H. C., van der Ploeg, A., & Starke, B. (2004). Computation of free-surface viscous flows at model and full scale by a steady iterative approach. *25th Symposium on Naval Hydrodynamics, St. John's, Newfoundland and Labrador, CANADA, 8-13 August 2004*.

Roe, P. L. (1981). Approximate Riemann solvers, parameter vectors, and difference schemes. *Journal of Computational Physics*, *43*, 357.

Saettone, S., Tavakoli, S., Taskar, B., Jensen, M. V., Pedersen, E., Schramm, J., Steen, S., & Andersen, P. (2020). The importance of the engine-propeller model accuracy on the performance prediction of a marine propulsion system in the presence of waves. *Applied Ocean Research*, *103*, 102320. https://doi.org/https://doi.org/10.1016/j.apor.2020.102320

Schultz, M., & Flack, K. (2007). The rough-wall turbulent boundary layer from the hydraulically smooth to the fully rough regime. *Journal of Fluid Mechanics*, *580*, 381–405. https://doi.org/10.1017/S0022112007005502

Song, K., Guo, C., Sun, C., Wang, C., Gong, J., Li, P., & Lianzhou, W. (2021). Simulation strategy of the full-scale ship resistance and propulsion performance. *Engineering Applications of Computational Fluid Mechanics*, *15*(1), 1321–1342. https://doi.org/10.1080/19942060.2021.1974091

Starke, A. R., & Bosschers, J. (2012). Analysis of scale effects in ship powering performance using a hybrid RANS-BEM approach. *29th Symposium on Naval Hydrodynamics Gothenburg, Sweden*.

Starke, A. R., Drakapoulos, K., Toxopeus, S. L., & Turnock, S. R. (2017). RANS-based full-scale power predictions for a general cargo vessel, and comparison with sea-trial results. *VII International Conference on Computational Methods in Marine Engineering, MARINE 2017*.

Taskar, B., Steen, S., Bensow, R. E., & Schröder, B. (2016). Effect of waves on cavitation and pressure pulses. *Applied Ocean Research*, *60*, 61–74. https://doi.org/https://doi.org/10.1016/j.apor.2016.08.009

Townsin, R. L., Byrne, D., Svensen, T. E., & Milne, A. (1981). Estimating the technical and economic penalties of hull and propeller roughness. *Transactions of the Society of Naval Architects and Marine Engineers*, *89*, 295–318.

Verkuyl, J.-B., & Raven, H. C. (2003). Joint EFFORT for validation of full-scale viscous-flow predictions. *The Naval Architect*, *1*.

Werner, S. (2021). (personal communication, february 2, 2021).

Werner, S., & Gustafsson, L. (2020). Uncertainty of speed trials. *Proceedings of the HullPIC 2020, Hamburg, Germany*, 26–28.

Wieleman, V. A. (2018). *Verification and validation of full-scale propulsion analysis using CFD*. Master Thesis, Delft University of Technology.

Zhang, D. H. (1990). *Numerical computation of ship stern/propeller flow*. PhD Thesis, Chalmers University of Technology.

Part II

Appended Papers

Paper I

Roughness effect modelling for wall resolved RANS – Comparison of methods for marine hydrodynamics

M. Orych, S. Werner, L. Larsson

Ocean Engineering 266 (2022)

10.1016/j.oceaneng.2022.112778

Ocean Engineering 266 (2022) 112778

Contents lists available at ScienceDirect

Ocean Engineering

journal homepage: www.elsevier.com/locate/oceaneng

Roughness effect modelling for wall resolved RANS – Comparison of methods for marine hydrodynamics

Michal Orych [a,c,*], Sofia Werner [b], Lars Larsson [c,d]

[a] FLOWTECH International AB, Gothenburg, Sweden
[b] SSPA AB, Gothenburg, Sweden
[c] Department of Mechanics and Maritime Sciences, Chalmers University of Technology, Gothenburg, Sweden
[d] International School of Yacht Design – ISYD AB, Sweden

ARTICLE INFO

Keywords:
CFD
RANS
Roughness
Ship
Hull
Full-scale
Uncertainty
Verification

ABSTRACT

This paper deals with several aspects of surface roughness modelling in RANS codes applied to full-scale ship simulations. To select a method that is suitable for wall-resolved RANS solvers and gives reliable results at high Reynolds numbers, five different roughness models are compared. A grid uncertainty analysis is performed and the sensitivity to the grid resolution close to the wall (y^+) is investigated. The results are compared to extrapolated results of experiments carried out with rough plates with various heights and roughness types. A correlation factor between the Average Hull Roughness and the equivalent sand roughness height is investigated, and a value of five is deemed the most suitable. The work suggests that the Aupoix-Colebrook roughness model gives the best results for full-scale ship simulations, at least with the current code, and that the near-wall grid resolution required for smooth surfaces can be applied also for the rough case.

1. Introduction

Computational Fluid Dynamics (CFD) simulations are widely used by ship designers to minimise fuel consumption. Until recently, such simulations have been carried out at model scale, the scale traditionally used in towing tank tests. The best insight into the current state-of-the-art of such model scale calculations is given by the series of Workshops on CFD in Ship Hydrodynamics. This series was initiated in 1980 and has been held every five years until 2015, Hino et al. (2020). Presently, CFD is applied more and more at full-scale, see e.g., the Joint Research Project, JoRes (2022), which focuses primarily on full-scale ship hydrodynamics.

Full-scale CFD predictions present some challenges compared to model scale. One is the small flow scales (relative to the hull length), which calls for very small cells, particularly near the hull surface. To avoid excessively large grids the cells must have a high aspect ratio. This has often caused numerical problems and has prevented the use of CFD at full-scale. However, with the present development of the numerical methods in CFD, this problem can be solved, see e.g., Orych et al. (2021).

Another challenge of full-scale CFD simulations is the roughness, i.e., the micro-scale surface deviations from the nominal shape. If the roughness is within the viscous sublayer, it does not affect the shear stress and the surface may be considered hydraulically smooth. This is the case for ships at model scale and therefore roughness is irrelevant. Hence little work on roughness models for ships has been carried out. For applications at Reynolds numbers typical for full-scale ships, the surface roughness leads however to increased drag and thickening of the boundary layer. The added resistance can be significant, and the operation of appendages and propellers may be affected.

The skin friction of a rough ship hull surface can be estimated using the extrapolation of model scale experimental data with the similarity-law scaling procedure of Granville (1987). It can also be calculated using formulas derived from integral boundary layer methods such as the one proposed by Townsin, ITTC (2017). Alternatively, roughness models can be used within CFD methods to simulate the roughness effects on skin friction, pressure resistance, and boundary layer development. Simulations with the roughness geometrically resolved are also possible on small surface samples, Atencio and Chernoray (2019), but are too expensive computationally to be applied to general cases.

The present paper deals with surface roughness in practical ship applications. Three problems are addressed. The first problem is the selection of a suitable roughness model for ship applications. In practical applications of CFD, the discretized surface of a body, around which the flow is being computed, is idealized and does not include micro-scale irregularities. In the Reynolds-Averaged Navier Stokes (RANS)

* Corresponding author. FLOWTECH International AB, Gothenburg, Sweden.
E-mail address: michal@flowtech.se (M. Orych).

https://doi.org/10.1016/j.oceaneng.2022.112778
Received 2 May 2022; Received in revised form 30 September 2022; Accepted 1 October 2022
Available online 17 October 2022

Nomenclature

β	Turbulence model closure constant, 0.09
κ	von Kármán constant, 0.41
ν	Kinematic viscosity
ρ	Density
τ_w	Wall shear stress
u_τ	Friction velocity
ω	Specific turbulence dissipation
AHR	Average Hull Roughness
C_F	Frictional resistance coefficient
C_P	Pressure resistance coefficient
C_T	Total resistance coefficient
k	Turbulent kinetic energy
k_S	Equivalent sand grain roughness height
U	Velocity or uncertainty
p	Observed order of accuracy
w_n	Nominal wake fraction
y	Wall distance
$(\,)^+$	Non-dimensional value
$(\,)_w$	Wall value

methods, the roughness effects are considered by numerical modelling. For RANS methods where wall functions are used to describe the innermost region of the boundary layer, the roughness effect is considered by the roughness function dU^+, Nikuradse (1950). A very comprehensive summary of this approach can be found in Andersson et al. (2020). However, for wall-resolved RANS methods, in which the flow is computed down to the wall, the roughness is simulated by modification of the boundary values of the turbulent kinetic energy, k, and the specific rate of dissipation of the turbulent kinetic energy, ω. Several models of this type have been proposed, see Wilcox (1998), Hellsten (1998), Knopp et al. (2009), and Aupoix (2014), all of which propose different relations between k, ω, and the roughness height. In the present paper, we will consider roughness models for the wall-resolved approach. Five different roughness models are compared at different Reynolds numbers and a range of roughness heights.

The next problem discussed in the paper is that the roughness measure commonly used in CFD, the equivalent sand roughness height, k_s, is not easily translated into the Average Hull Roughness, AHR, which is used in the marine industry. Correlations for several representative surface conditions are proposed by Schultz and Flack (2007) based on measurements, but these correlations cannot be generalized to all types of coatings and fouling types, or numerical roughness models.

The third problem considered is the dependence on y^+, defined below. This is the non-dimensional distance from the wall to the first cell centre off the wall. A noticeable influence of y^+ for wall-resolved methods is indicated by Eça et al. (2010) and Eça et al. (2018). The first paper suggests that y^+ lower than 0.2 is needed for y^+ independence, especially for larger roughness heights, while the second paper indicates that values as low as 0.1 are necessary in the case of the k-ω SST turbulence model, even for hydraulically smooth surfaces. Therefore, special attention is paid below to the sensitivity of the computations to the grid resolution at the no-slip boundaries.

In the next section, we introduce the flow solver in which the roughness models are implemented. Then the five different models are presented. The test cases are described, and a numerical uncertainty analysis is presented for a flat plate and a ship hull. Additionally, the sensitivity of the solution to y^+ is investigated. In the results sections, the performance of the different roughness models is compared. A qualitative benchmark against flat plate measurement data extrapolated to a high Reynolds number and a result of another CFD code is presented. No formal validation for a full-scale ship is possible at present due to the lack of experimental data for which the effects of the roughness can be properly isolated. The final part of the paper highlights the problem of converting the Average Hull Roughness to the equivalent sand roughness height. A suggestion for a conversion factor for a selected model is given.

2. Flow solver

The software used for the present computations is SHIPFLOW. This is commercial software that includes several flow solvers, Janson (1997), Broberg et al. (2007). The RANS solver (XCHAP) is used in the present study. XCHAP solves the steady incompressible Reynolds Averaged Navier-Stokes equations using a finite volume method. There are two available turbulence models, k-ω SST, Menter (1993), and an explicit algebraic stress model, EASM, Deng, et al. (2005). No wall functions are used, and the equations are integrated down to the wall. The equations are discretized using the Roe (1981) scheme for the convection while a central scheme is used for the diffusive fluxes. An explicit flux correction is applied to achieve second-order accuracy. XCHAP is based on structured grids. Multi-block structured or overlapping grids are used for more complex geometries.

The momentum and continuity equations are solved in a coupled manner while the turbulent quantities are solved separately. A Krylov-type solver, PETSc (2020a) is used for linear equations. The Generalized Minimal Residual, GMRES, method PETSc (2020b) with the block Jacobi preconditioner PETSc (2020c) is in this case very efficient both in terms of convergence speed and stability.

3. Roughness modelling

In RANS methods with wall resolved boundary layers the roughness effect is modelled by a modification of the boundary conditions for the specific dissipation rate of turbulent kinetic energy, ω, alone or together with the turbulent kinetic energy, k. The k and ω values are fulfilled at the no-slip wall using two layers of ghost cells outside of the grid boundaries. In the implementation presented, the roughness is expressed using the equivalent sand grain roughness height, k_S, Schlichting (1936). The relation between k_S and the physical surface roughness characteristics is discussed below.

For this study, several roughness models that are suitable for k-ω SST and EASM turbulence models are implemented and tested. Dirichlet boundary conditions for k and ω are specified by the roughness models based on the roughness height, k_S. The models were developed based on experimental data and use different functions to represent the effects of the roughness. We investigate the suitability of the models for naval architecture applications, but the approach is not limited to this area and could be used in aerodynamics as well. Note that the designations used here are only to indicate the origin of each method and may not represent its proper naming.

3.1. Hellsten

A "slightly-rough-surface" boundary condition proposed by Wilcox (1998) can be applied to the k-ω SST turbulence model. The wall value of ω is expressed as a function of the non-dimensional roughness height, ks^+. In the extension of this method, Hellsten (1998) introduced a lower limit for ks^+ which depends on y^+. This limit makes the result more grid-independent for hydraulically smooth walls.

To obtain the wall value of ω the following equations are used:

$$y^+ = \frac{u_\tau}{\nu}\, y, \text{where } u_\tau = \sqrt{\frac{\tau_w}{\varrho}}$$

$$ks^+ = \frac{u_\tau}{\nu}\, ks$$

$$ks^+_{min} = 4.3\ y^{+0.85}$$

$$ks^+ = \max\ (ks^+, ks^+_{min})$$

$$SR = \begin{cases} \left(\dfrac{50}{ks^+}\right)^2 & ks^+ \le 25 \\ \dfrac{100}{ks^+} & ks^+ > 25 \end{cases}$$

$$\omega_w = \frac{u_\tau^2}{\nu} SR\ .$$

In this roughness model, the wall value of k is set to zero.

3.2. Knopp

In the method proposed by Knopp et al. (2009), both k and ω are based on ks^+. The model is calibrated with the Ligrani and Moffat correlation, Ligrani and Moffat (1986), and should work well in the fully rough regime, $ks^+ > 100$. Schlichting (1979). However, in the transitional regime, the frictional resistance coefficient could be underestimated.

Here ω at the wall is obtained from:

$$d_0 = 0.03\ ks\ \min\left(1, \left(\frac{ks^+}{30}\right)^{\frac{2}{3}}\right)\ \min\left(1, \left(\frac{ks^+}{45}\right)^{\frac{1}{4}}\right)\ \min\left(1, \left(\frac{ks^+}{60}\right)^{\frac{1}{3}}\right)$$

$$\omega_w = \min\left(\frac{u_\tau}{\sqrt{\beta}\ \kappa\ d_0}, \frac{60\ \nu}{\beta\ y^2}\right)\ .$$

The wall value of k is defined by

$$k_w = \min\left(1, \frac{ks^+}{90}\right)\ \frac{u_\tau^2}{\sqrt{\beta}}\ .$$

3.3. Knopp - modified

A modification to the Knopp model is made by Queutey and Visonneau (2021) to improve the results in the transitional regime. An additional relation between ω and k^+_S is added.

The additional parameter is

$$c_0 = 0.025\left(0.5 + 0.5\cos\left(\frac{\min(ks^+, 90)}{90}\ \pi\right)\right),$$

which depends on the $ks^+$is introduced in

$$d_0 = (0.03 + c_0\ )\ ks\ \min\left(1, \left(\frac{ks^+}{30}\right)^{\frac{2}{3}}\right)\ \min\left(1, \left(\frac{ks^+}{45}\right)^{\frac{1}{4}}\right)\ \min\left(1, \left(\frac{ks^+}{60}\right)^{\frac{1}{4}}\right)$$

and the final expression for the wall value of ω is

$$\omega_w = \min\left(\frac{u_\tau}{\sqrt{\beta}\ \kappa\ d_0}, \frac{60\ \nu}{\beta\ y^2}\right)\ .$$

The wall value of k is the same as in the original Knopp model.

3.4. Aupoix – Nikuradse

The first model derived by Aupoix (2014) addresses the poor transition region predictions of the models above and should give reasonable results for large roughness heights. It is based on Nikuradse's correlation, Nikuradse (1950), and referred to in the present paper as Aupoix-Nikuradse.

The expression for the wall value of ω is as follows:

$$\omega_w = \min\left(\left(\frac{400000}{ks^{+4}}\left(\tanh\left(\frac{10000}{3ks^{+3}}\right)\right)^{-1} + \frac{70}{ks^+}\left(1 - \exp\left(\frac{-ks^+}{300}\right)\right)\right)\frac{u_\tau^2}{\nu}, \frac{60\nu}{\beta y^2}\right).$$

The wall value of k is obtained from:

$$k_w = \max\left(0, \frac{1}{\sqrt{\beta}}\tanh\left(\left(\frac{\log\left(\frac{ks^+}{30}\right)}{\log(8)} + 0.5\left(1 - \tanh\left(\frac{ks^+}{100}\right)\right)\right)\tan\left(\frac{ks^+}{75}\right)\right)\right)u_\tau^2.$$

3.5. Aupoix – Colebrook

The second model derived by Aupoix (2014) should have similar capabilities as the first one but is based on Grigson's representation of Colebrook's results, Grigson (1992). It is further referred to as Aupoix-Colebrook.

To obtain the wall value of ω the following function is used:

$$\omega_w = \min\left(\left(\frac{300}{ks^{+2}}\left(\tanh\left(\frac{15}{4\ ks^+}\right)\right)^{-1} + \frac{191}{ks^+}\left(1 - \exp\left(\frac{-ks^+}{250}\right)\right)\right)\frac{u_\tau^2}{\nu}, \frac{60\nu}{\beta\ y^2}\right)$$

and the wall value of k is defined by

$$k_w = \max\left(0, \frac{1}{\sqrt{\beta}}\tanh\left(\left(\frac{\log\left(\frac{ks^+}{30}\right)}{\log(10)} + \left(1 - \tanh\left(\frac{ks^+}{125}\right)\right)\right)\tan\left(\frac{ks^+}{125}\right)\right)\right)u_\tau^2\ .$$

4. Test cases

The simulations are performed for a flat plate and a container vessel hull. In the first case, both low and high Reynolds numbers are investigated, while in the second case only full-scale is considered.

4.1. Flat plate

There are two flat plate cases investigated in 2D. The first one is a plate that was tested in a towing tank at SSPA, Leer-Andersen et al. (2018) and the second one is a hypothetical plate with the same length and Reynolds number as a full-scale container vessel.

The physical length of the first plate is 6.921 m and is simulated with a water temperature of 20 °C giving the viscosity $\nu = 1.0023 \times 10^{-6}$ m^2/s and the density $\rho = 998.2$ kg/m^3. The lowest towing speed is 1 m/s and the highest is 11 m/s. The Reynolds number range is from 6.9×10^6 to 7.6×10^7.

4.2. Ship hull

The ship hull used in this investigation is the KRISO Container Ship (KCS), a standard test case in ship hydrodynamics, Hino et al. (2020). The simulations are performed at a ship speed of 24 knots (12.35 m/s). With a length between the perpendiculars of 230 m, this corresponds to a Reynolds number of 2.89×10^9.

5. Numerical uncertainty

The numerical uncertainty and the order of accuracy are estimated using the method by Eça and Hoekstra (2014). The method can be applied to estimate the grid uncertainty of solutions where scatter is difficult to avoid. Implementation in the convenient form of a software tool is provided by MARIN (2018).

The uncertainty estimation is carried out for the 2D flat plate at both Reynolds numbers and for the ship hull at full scale. All computations presented in this section are performed with the EASM turbulence model

and with the Aupoix-Colebrook roughness model.

Numerical uncertainty includes both grid and iterative uncertainty, but all simulations are carried out with very strict convergence criteria. In the worst cases, the standard deviations calculated for the last 10% of the iterations are at most 5.0×10^{-3}% for the viscous pressure and 1.0×10^{-3}% for the frictional resistance. This means that the iterative uncertainty is 2–3 orders of magnitude smaller than the grid uncertainty, and it is not included in the analysis.

5.1. Flat plate

For the flat plate, a series of six geometrically similar grids is generated. The grid refinement ratio is $\sqrt[6]{2}$ in the directions parallel with, and normal to the wall. In the transverse direction, the number of cells is always three. Applying proper boundary conditions, three cells in the transverse direction are enough to simulate a 2D case. The total number of cells ranges from 0.28×10^6 to 1.38×10^6 and y^+ varies from about 1.0 to 0.4, see Table 1. The calculations are performed at the Reynolds numbers 6.9×10^6 and 2.89×10^9. Two different roughness heights are simulated, $k_S = 0$ and $k_S = 300$.

The domain is divided into three sections describing the part in front of the plate, along the plate, and behind it. It should be noted that the plate thickness is zero. The boundary conditions are set to no-slip on the part of the domain face representing the plate, and the rest of this face has a slip condition applied. The sides and the top of the domain are also slip boundaries. A schematic representation of the grid is shown in Fig. 1.

The numerical uncertainty of the frictional resistance coefficient, C_F, for the finest grid at Reynolds number 6.9×10^6 is 0.8% for the smooth plate. See Fig. 2. For the rough plate, it is 0.4%, as seen in Fig. 3. At Reynolds number 2.89×10^9, the uncertainties are 1.8% and 0.6%, respectively. The relatively similar uncertainty levels regardless of the Reynolds number can be explained by the fact that similar y^+ values were used, and the highly stretched mesh provided sufficient flow resolution.

As a separate study, the sensitivity to y^+ is studied. Three sets of grids with y^+ values 0.1, 0.5, and 1.0 are tested. All grids have the same number of cells and are similar to grid number one in Table 1. The computations are performed with the EASM turbulence model and the Aupoix-Colebrook roughness model. At a Reynolds number of 6.9×10^6 and y^+ dependency is visible. The difference between y^+ 0.1 and 1.0 is about 2% on average in the k_S range between 0 and 200 μm, Fig. 4. At Re 7.6×10^7 the sensitivity is much smaller, about 1% on average, see Fig. 5.

5.2. SHIP hull

A series of six geometrically similar grids is generated to study the numerical uncertainty and select a suitable grid for simulations with various roughness models. The grid refinement ratio is $\sqrt[6]{2}$ in each direction and the total number of cells ranges from 1.15×10^6 to 14.4×10^6. The calculations are performed for $k_S = 0$ and $k_S = 300$.

The numerical uncertainty of C_F for the finest grid and smooth hull is 0.6%, see Fig. 6. For the rough hull, it is 0.5%, Fig. 7. The total resistance coefficient, C_T, shows larger but still reasonable uncertainties: 2.8% and 1.4% respectively, due to the larger sensitivity of the viscous pressure resistance component, Figs. 8 and 9.

Apart from the main series of grids an additional series is run to investigate the y^+ dependence. The third finest grid is refined only in the direction normal to the hull. For these grids y^+ is 0.1, 0.5 and 1.0, respectively. See Table 2. The calculations are performed for $k_S = 0$ and $k_S = 300$.

As seen in Fig. 10, the sensitivity of C_F to y^+ is insignificant below $k_S = 500$ μm for the k-ω SST turbulence model. Similar results have been obtained for the EASM model.

For larger roughness heights k-ω SST is considerably less sensitive than EASM, Figs. 11 and 12. The latter starts to show differences above

Table 1
Total number of cells and number in each direction for the flat plate.

Grid	y^+	No. of Cells	Longitudinal	Spanwise	Normal
1	0.40	1382375	2038	3	226
2	0.48	976816	1712	3	190
3	0.57	689472	1440	3	160
4	0.67	487618	1210	3	134
5	0.80	345255	1018	3	113
6	0.95	242496	856	3	94

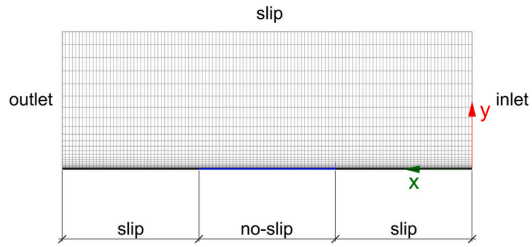

Fig. 1. A schematic representation of the grid domain and boundary conditions for the flat plate simulations.

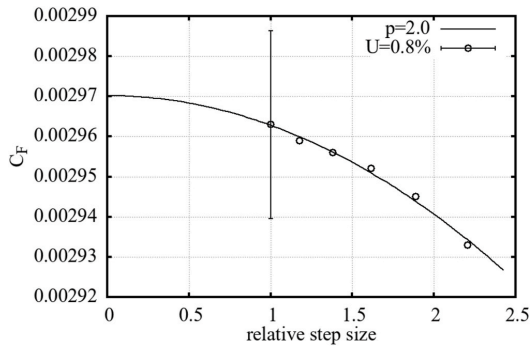

Fig. 2. Grid convergence of C_F, flat plate at Re $= 6.9 \times 10^6$ and $k_S = 0$. Computed uncertainty of the finest grid: 0.8%, shown as a bar.

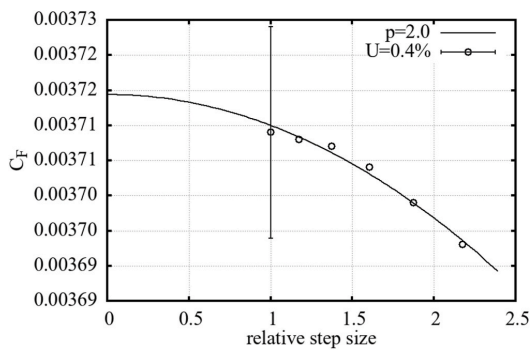

Fig. 3. Grid convergence of C_F, flat plate at Re $= 6.9 \times 10^6$ and $k_S = 300$. Computed uncertainty of the finest grid: 0.4%, shown as a bar.

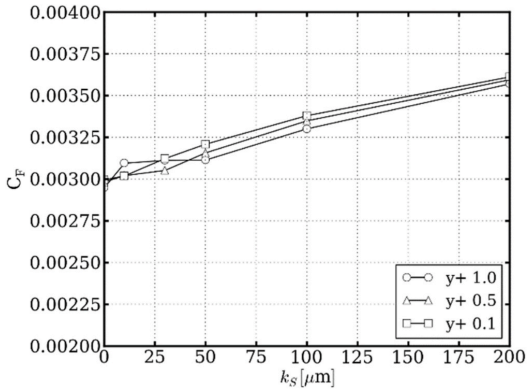

Fig. 4. y + sensitivity for EASM turbulence model with Aupoix-Colebrook roughness model at Re = 6.9×10^6.

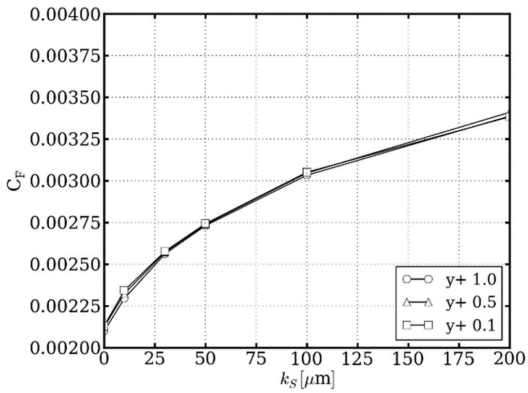

Fig. 5. y + sensitivity for EASM turbulence model with Aupoix-Colebrook roughness model at Re = 7.6×10^7.

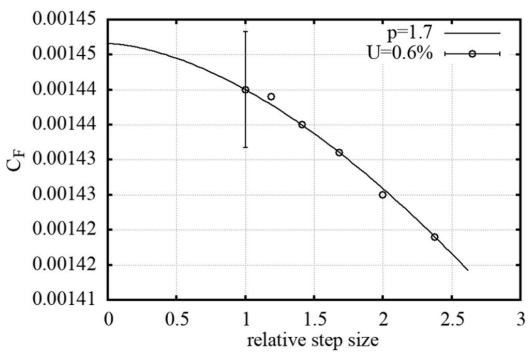

Fig. 6. Grid convergence of C_F, KCS hull at Re = 2.89×10^9 and $k_S = 0$. Computed uncertainty of the finest grid: 0.6%, shown as a bar.

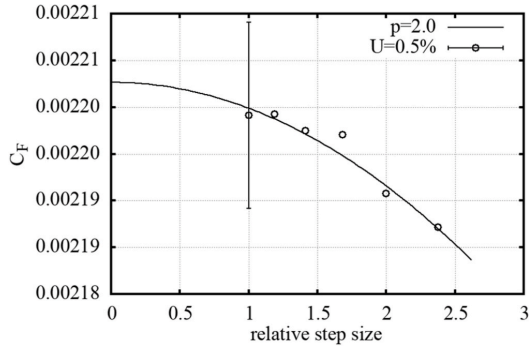

Fig. 7. Grid convergence of C_F, KCS hull at Re = 2.89×10^9 and $k_S = 300$. Computed uncertainty of the finest grid: 0.5%, shown as a bar.

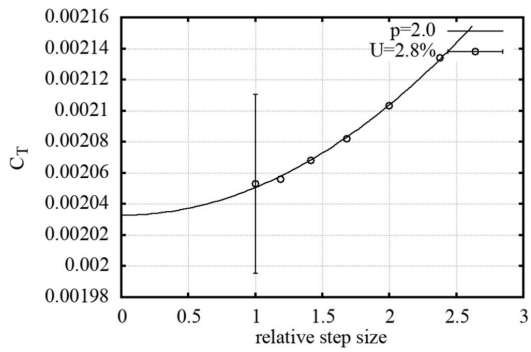

Fig. 8. Grid convergence of C_T, KCS hull at Re = 2.89×10^9 and $k_S = 0$. Computed uncertainty of the finest grid: 2.8%, shown as a bar.

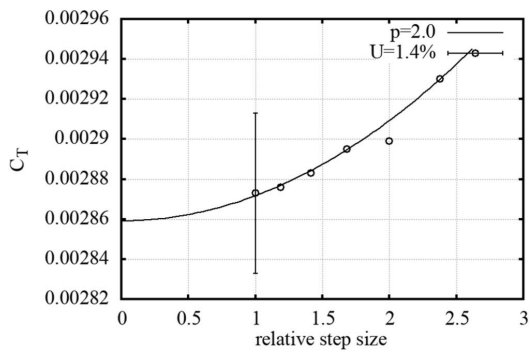

Fig. 9. Grid convergence of C_T, KCS hull at Re = 2.89×10^9 and $k_S = 300$. Computed uncertainty of the finest grid: 1.4%, shown as a bar.

Table 2
Total number of cells and number in each direction.

y^+	No. of Cells	Longitudinal	Girth wise	Normal
0.1	4.19×10^6	380	69	160
0.5	3.98×10^6	380	69	152
1.0	3.90×10^6	380	69	149

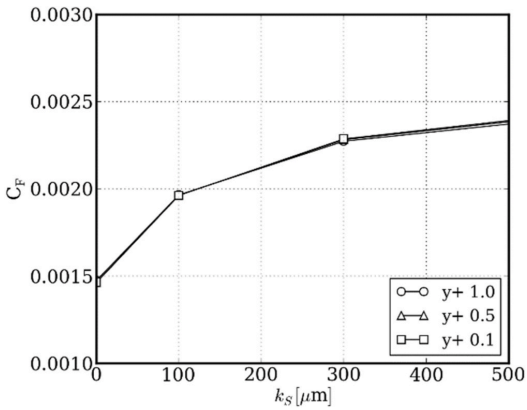

Fig. 10. Influence of y + on C_F, k-ω SST, Aupoix-Colebrook, range 0–500 μm.

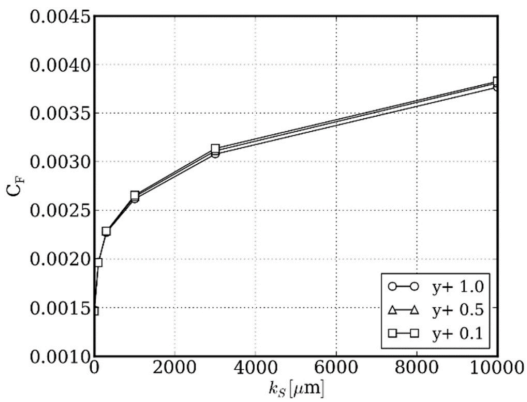

Fig. 11. Influence of y + on C_F, k-ω SST, Aupoix-Colebrook, range 0–10 000 μm.

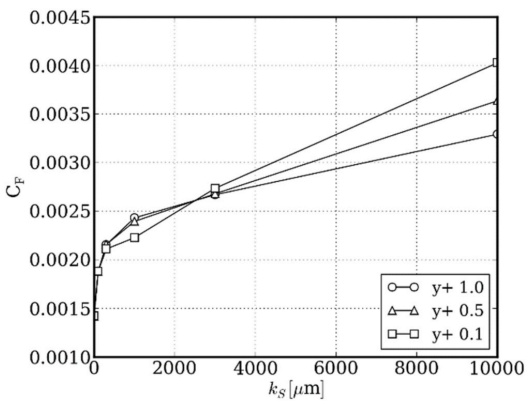

Fig. 12. Influence of y + on C_F, EASM, Aupoix-Colebrook, range 0–10 000 μm.

$k_S = 1000$ μm. However, for a typical ship in service, the equivalent sand roughness height is in a range from 20 to 100 μm. Note that k_S is not equivalent to average hull roughness, AHR, as will be discussed below.

The viscous pressure resistance coefficient, C_{PV}, is less sensitive to y^+ variations. The difference across the given k_S range is 1–2% for k-ω SST, Fig. 13. For EASM, at the highest considered k_S, the difference between y^+ 0.1 and 1.0 is about 6% and drops to less than 1% below $k_S = 1000$ μm, Fig. 14. In general, the sensitivity to y^+ is considerably smaller than in the earlier work by Eça mentioned above.

The general conclusion from the uncertainty analysis is that numerical errors are considerably smaller than the differences between the roughness models presented in Section 6. For the simulations of Section 6, the third finest grid with 5.2×10^6 cells and $y^+ = 0.5$ is selected.

6. Results

This section presents the skin friction coefficient for all described roughness models. For the container vessel, the effect of surface roughness on the viscous pressure resistance and the nominal wake is also included.

6.1. Flat plate – model-scale Reynolds number

Fig. 15 shows the frictional resistance coefficient for $Re = 6.9 \times 10^6$. For small k_S values, the wall values of k and ω are below the minimum values described by the equations in Section 3. Hence, the results are constant for small roughness heights in the case of the Knopp, modified Knopp, and Aupoix-Nikuradse models. The k_S^+ values are just above the limit for a hydraulically smooth surface suggested by Nikuradse (1950), Schlichting (1979), and Schultz and Flack (2007). The Hellsten model shows only a small increase in C_F with roughness height. In the case of Aupoix-Colebrook, the C_F increase is larger. For the flat plate, both investigated turbulence models show qualitatively similar results. Only a shift in values is observed, with a lower level for the EASM. Therefore, results are presented for only one turbulence model.

At $Re = 7.6 \times 10^7$, the differences in C_F increase between the roughness models are visible, Fig. 16. All models except Aupoix-Colebrook have a concave beginning of the $C_F(k_S)$ curves. The modified Knopp indicates a little higher C_F than the original one at k_S = 50–100 μm.

6.2. Flat plate - full-scale Reynolds number

The second series of simulations is done as a reference. It is a flat

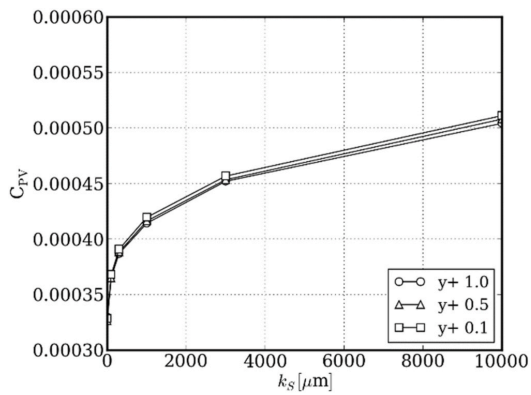

Fig. 13. Influence of y + on CPV, k-ω SST, Aupoix-Colebrook, range 0–10 000 μm.

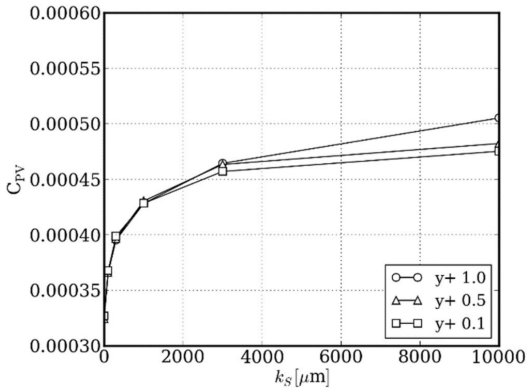

Fig. 14. Influence of y + on C_{PV}, EASM, Aupoix-Colebrook, range 0–10 000 μm.

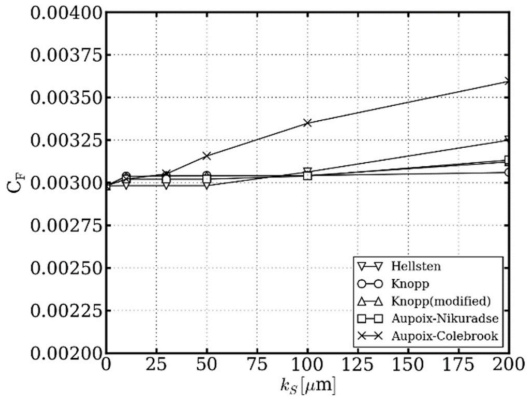

Fig. 15. Frictional resistance coefficient at Re = 6.9 × 10^6, EASM.

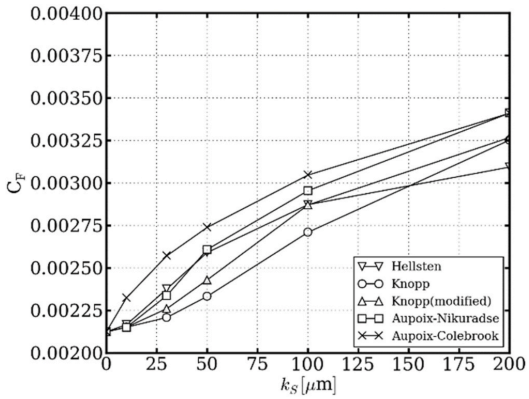

Fig. 16. Frictional resistance coefficient at Re = 7.6 × 10^7, EASM.

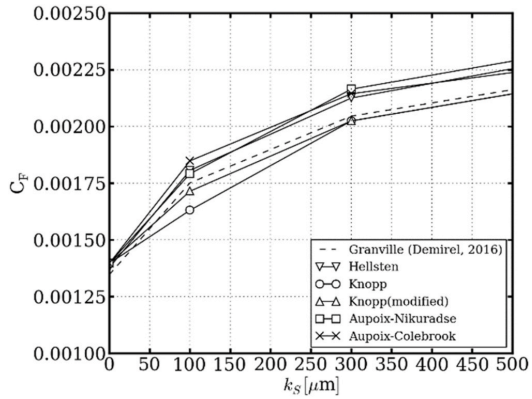

Fig. 17. Roughness model comparison for a flat plate at Re = 2.89 × 10^9, k-ω SST, k_S range 0–500 μm.

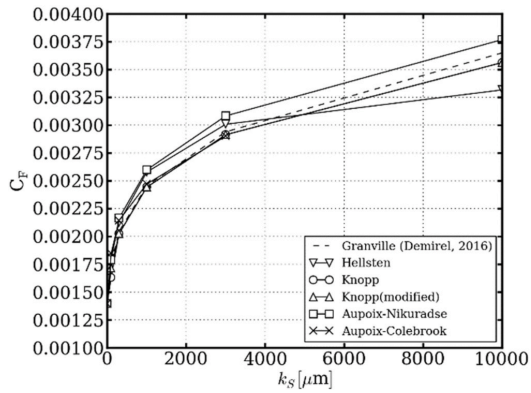

Fig. 18. Roughness model comparison for a flat plate at Re = 2.89 × 10^9, k-ω SST, k_S range 0–10 000 μm.

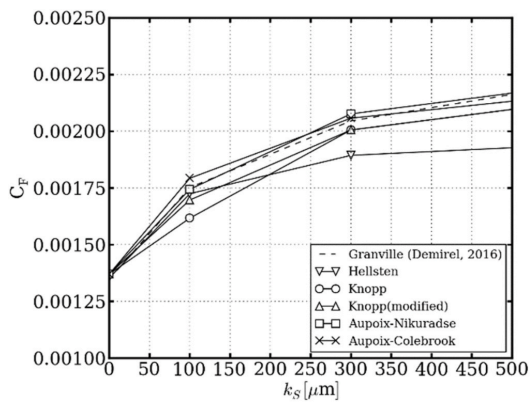

Fig. 19. Roughness model comparison for a flat plate at Re = 2.89 × 10^9, EASM, k_S range 0–500 μm.

plate with a length and Reynolds number corresponding to the KCS ship.

All roughness models are tested both with k-ω SST and EASM turbulence models, see Fig. 17 through Fig. 20. The figures also include a calculation based on Granville's method presented in Demirel et al. (2017). To illustrate the entire k_S range with sufficient clarity separate plots are created for k_S from 0 to 500 μm and from 0 to 10 000 μm. In general, EASM shows lower C_F than k-ω SST. The k-ω SST results are generally consistent with Granville in the entire range while the EASM starts deviating considerably for k_S above 1000 μm for all roughness models except Hellsten which indicates problems as early as 300 μm. For the k_S values up to 500 μm, the increase in C_F due to roughness is well captured. At $k_S = 100$ μm, one can also recognize the improvement of the modified Knopp. This model shows the best agreement with the Granville reference for k-ω SST and is within a 3% difference for k_S up to 10 000 μm. For the EASM the Aupoix-Nikuradse is closest to Granville and performs well up to $k_S = 1000$ μm (see Fig. 19) (see Fig. 18).

6.3. Container Ship – full-scale

The KRISO Container Ship, KCS, is selected for an evaluation of the roughness models. There is no full-scale data available. However, there is a possibility to cross-check the results with other researchers who also performed similar simulations. This comparison is only intended to illustrate the general behaviour of the codes and various roughness models.

For each roughness model, plots are presented of the frictional resistance coefficient, C_F, viscous pressure resistance coefficient, C_{PV}, and the nominal wake fraction, w_n. The k_S range is first restricted to 0–500 μm for a better presentation of lower roughness heights and then the entire range of 0–10 000 μm is shown. The results of the EASM turbulence model are given for all quantities, while the k-ω SST results are shown only for those that exhibit a larger difference compared with the EASM.

The present C_F predictions from SHIPFLOW are compared with the results from STAR-CCM + utilizing a wall function approach and the scaling procedure of Granville presented by Demirel et al. (2017).

The frictional resistance coefficient for the KCS, Fig. 21, follows a pattern very similar to that of the flat plate results at the same Reynolds number. The modified Knopp is in the best agreement with the other CFD code while Aupoix-Colebrook has the highest C_F increase in the lower range of k_S. Also, the Hellsten model seems to flatten out the quickest, starting already at k_S about 100 μm.

The viscous pressure resistance coefficient is presented in Fig. 22. The pattern for various roughness models follows the same relative trends as the friction coefficient. There is no external reference for these simulations, but it can be observed that the original Knopp shows the lowest value of all at $k_S = 100$ indicating problems in the transitional regime. This is improved with the modified version and other roughness

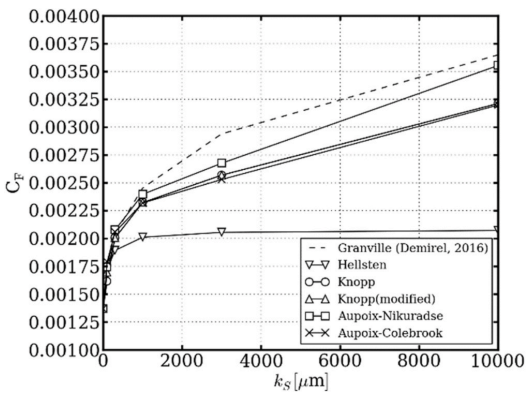

Fig. 20. Roughness model comparison for a flat plate at Re = 2.89 × 10^9, EASM, k_S range 0–10 000 μm.

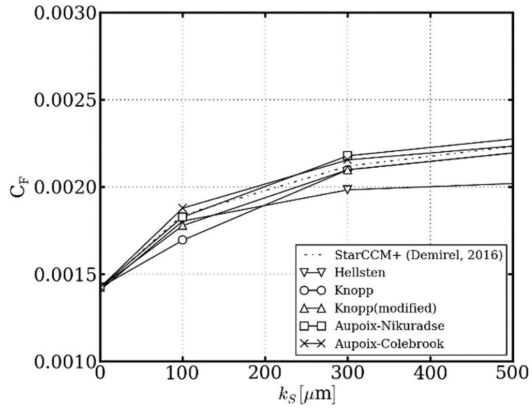

Fig. 21. C_F for KCS at Re = 2.89 × 10^9, EASM, k_S range 0–500 μm.

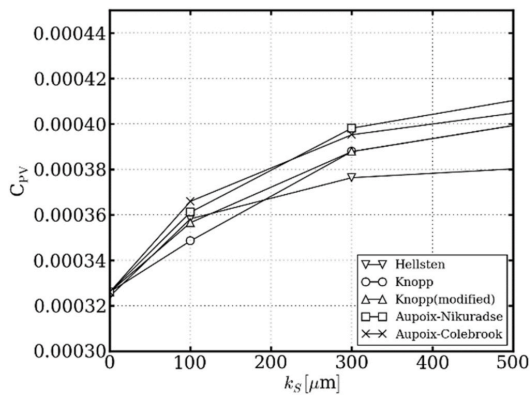

Fig. 22. C_{PV} for KCS at Re = 2.89 × 10^9, EASM, k_S range 0–500 μm.

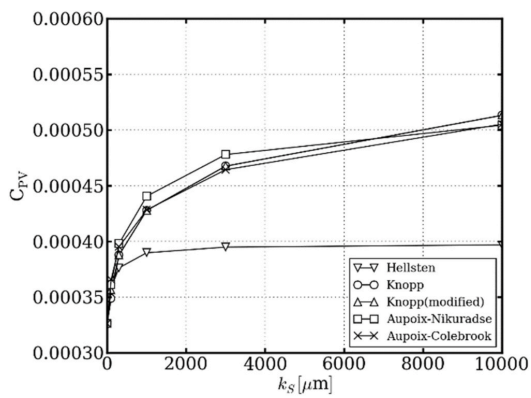

Fig. 23. C_{PV} for KCS at Re = 2.89 × 10^9, EASM, k_s range 0–10 000 μm.

models including the simplest Hellsten which fails for higher k_S.

The large difference between Hellsten and the other models is visible when the k_S is increased further, see Fig. 23. There is nearly no visible resistance increase above $k_S = 1000$. The other models show consistent behaviour, with only small differences, up to $k_S = 10\,000$.

The nominal wake values are consistent with the viscous pressure and frictional resistance results indicating a close relationship between them. See Figs. 24 and 25 for the range up to k_S 500 and 10 000 μm, respectively.

7. Equivalent sand roughness and average hull roughness correlation

The final problem to be discussed is the correlation between the roughness measures. There is no universal way to convert the Average Hull Roughness, AHR, for all types of roughness found on various surfaces to a single k_S value. In fact, a given AHR may yield different resistance increases depending on the surface texture. However, through tests that are more specific to our applications, it is possible to find a reasonable correlation. An example of such a procedure is shown here. It is based on measurements with several painted surfaces which are extrapolated to full-scale length with Granville's method and to appropriate speed with Grigson's method using SSPA's Skin Friction Database tool, Leer-Andersen et al. (2018). The extrapolated data is plotted in Fig. 26 together with computational results for all roughness models, as well as with results from Demirel et al. (2017), and from Townsin's formula for added resistance due to roughness, ITTC (2017). The roughness height for the simulations is scaled to find a good correlation with the measurements and an AHR/k_S factor of 5 gives the most reasonable match for the Aupoix-Colebrook model. The other models are well below the measurements with this factor and adjusting it does not improve the results. It should be noted that this is based on specific measurement samples for roughness types like those on a ship's hull with anti-fouling paint and no severe biofouling.

The correlation factor is also investigated in Orych et al. (2021) for another ship with similar conclusions. Schultz (2007) proposes a variable AHR/k_S factor which depends on roughness height and type. It is equal to five for AHR = 150 μm, that is representing a typical anti-fouling coating. The factor is three for a deteriorated surface or a light slime at AHR = 300 μm. Applying that to our CFD simulations gives a frictional resistance increase of more than 30% (diamonds in Fig. 26) compared to 23% with the factor five, assuming anti-fouling coating surface texture. For higher roughness, the factor is reduced even more and goes to one at 1000 μm. This indicates that the different sources

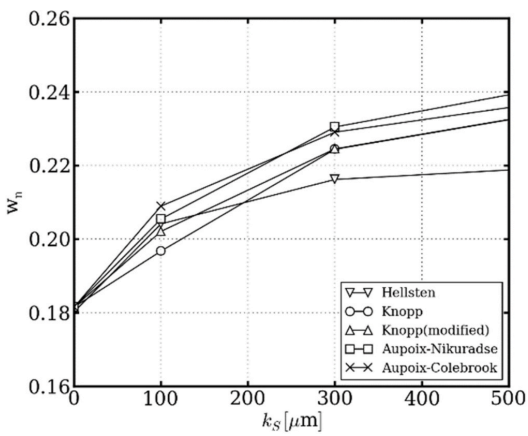

Fig. 24. w_n for KCS at Re = 2.89 × 10^9, EASM, k_S range 0–500 μm.

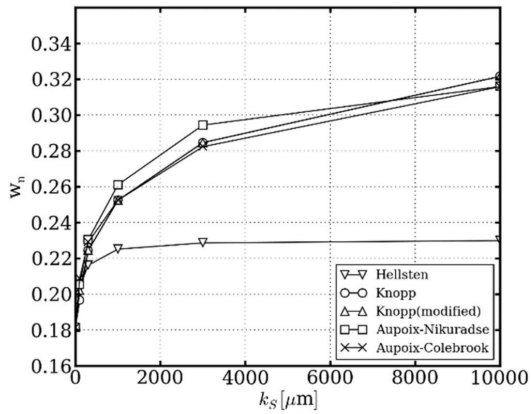

Fig. 25. w_n for KCS at Re = 2.89 × 10^9, EASM, k_S range 0–10 000 μm.

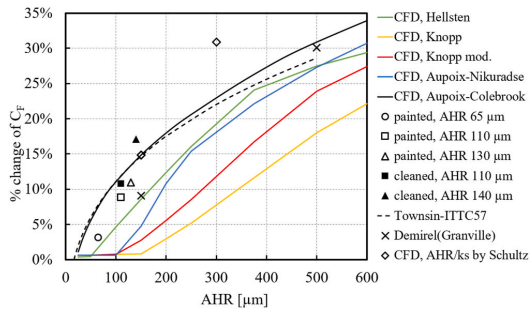

Fig. 26. Comparison of extrapolated measured values, simulations with correlation factor 5, and Townsin's formula for a flat plate at Re = 2.89 × 10^9.

agree in predicting the resistance increase for ships with normal surface conditions. The roughness height typical of a well-maintained ship in service is less than 100 μm after the cleaning, and below 300 μm for most of the time, Oliveira et al. (2020). With severe fouling, the roughness texture is different, and the numerical methods tuned for anti-fouling conditions may not be applicable. A single parameter such as AHR cannot describe all roughness types. Further research is needed to investigate the applicable range, but there is a lack of accurate full-scale measurements for such cases.

8. Conclusions

Five roughness models are implemented in two wall-resolved turbulence models of a RANS solver: Hellsten, Knopp, modified Knopp, Aupoix – Nikuradse, and Aupoix – Colebrook. Three test cases are studied and qualitative comparisons between the models are made. A correlation between the Average Hull Roughness, AHR, and the equivalent sand roughness, k_S, is discussed based on measurement data extrapolated to full-scale is used to correlate the AHR and k_S.

The objective of the paper has been to investigate three problems related to the modelling of roughness in wall-resolved RANS computations. The following conclusions may be drawn:

- The performance of the selected roughness models shows that Aupoix-Colebrook yields the most reasonable results when compared to extrapolated model scale experiments and another CFD method.

- In the present implementation, the y^+ sensitivity is small. Values in the range 0.5–1.0 are sufficient.
- The Aupoix-Colebrook roughness model together with the AHR/k_S correlation factor of 5 is suitable for roughness heights typical for well-maintained ships in service.

CRediT authorship contribution statement

Michal Orych: Conceptualization, Methodology, Software, Validation, Visualization, Writing – original draft. **Sofia Werner:** Writing – review & editing. **Lars Larsson:** Supervision, Writing – review & editing.

Declaration of competing interest

The authors declare the following financial interests/personal relationships which may be considered as potential competing interests: Michal Orych reports financial support was provided by Energimyndigheten (Swedish Energy Agency). Michal Orych reports a relationship with FLOWTECH International AB that includes: board membership and employment.

Data availability

Data will be made available on request.

Acknowledgements

The authors would like to thank Swedish Energy Agency for the financial support. The computations were enabled by resources provided by the Swedish National Infrastructure for Computing (SNIC) at C3SE, partially funded by the Swedish Research Council through grant agreement no. 2016–07213.

References

Andersson, J., Oliveira, D., Yeginbayeva, I., Leer-Andersen, M., Bensow, R., 2020. Review and comparison of methods to model ship hull roughness. Appl. Ocean Res. 99 https://doi.org/10.1016/j.apor.2020.102119. ISSN 0141-1187.

Atencio, B.N., Chernoray, V., 2019. A resolved RANS CFD approach for drag characterization of antifouling paints, 2019 Ocean. Eng. 171, 519–532. ISSN 0029-8018.

Aupoix, B., 2014. Wall roughness modelling with k-w STT model. In: 10th International ERCOFTAC Symposium on Engineering Turbulence Modelling and Measurements, Sep 2014. MARBELLA, Spain.

Broberg, L., Regnström, B., Östberg, M., 2007. XCHAP - Theoretical Manual. FLOWTECH International AB.

Demirel, Y.K., Turan, O., Incecik, A., 2017. Predicting the effect of biofouling on ship resistance using CFD. Appl. Ocean Res. 62, 100–118.

Deng, G.B., Queutey, P., Visonneau, M., 2005. Three-dimensional flow computation with Reynolds stress and algebraic stress models. Proceed. ERCOFTAC Int. Symp. Eng. Turb. Model. Measure. ETMM6, Sardinia, Italy, 23–25 May, 2005.

Eça, L., Hoekstra, M., Raven, H.C., 2010. Quantifying roughness effects by ship viscous flow calculations, 28th symposium on naval hydrodynamics. Pasadena, Califor. September 16, 2010.

Eça, L., Hoekstra, M., 2014. A procedure for the estimation of the numerical uncertainty of CFD calculations based on grid refinement studies. J. Comput. Phys. 262, 104–130. April 2014.

Eça, L., Pereira, F., Vaz, G., 2018. Viscous flow simulations at high Reynolds numbers without wall functions: is $y+ \simeq 1$ enough for the near-wall cells? Comput. Fluids 170. https://doi.org/10.1016/j.compfluid.2018.04.035.

Granville, P.S., 1987. Three indirect methods for the drag characterization of arbitrarily rough surfaces on flat plates. J. Ship Res. 31, 70–77.

Grigson, J., 1992. Drag losses of new ships caused by hull finish. J. Ship Res. 36, 182–196, 02.

Hellsten, A., 1998. Some Improvements in Menter's K-Omega SST Turbulence Model. 29th AIAA, Fluid Dynamics Conference. Fluid Dynamics and Co-located Conferences. https://doi.org/10.2514/6.1998-2554.

Hino, T., Stern, F., Larsson, L., Visonneau, M., Hirata, N., Kim, J., 2020. Numerical ship hydrodynamics. An assessment of the tokyo 2015 workshop. In: Lecture Notes in Applied and Computational Mechanics, vol. 94. Springer Nature, Switzerland. https://doi.org/10.1007/978-3-030-47572-7, 978-3-030-47571-0.

ITTC, 2017. Proceedings of 25th ITTC - Volume II, Final Report and Recommendations to the 25th ITTC. The Specialist Committee on Powering Performance Prediction, Fukuoka, Japan.

Janson, C.-E., 1997. Potential Flow Panel Methods for the Calculation of Free-Surface Flows with Lift. PhD Thesis. Chalmers University of Technology, Göteborg, Sweden.

JoRes, 2022. Development of an industry recognised benchmark for ship energy efficiency solutions. https://jores.net/.

Knopp, T., Eisfeld, B., Calvo, J.B., 2009. A new extension for k-ω turbulence models to account for wall roughness. Int. J. Heat Fluid Flow 30 (1), 54–65, 101016/jijheatfluidflow200809009.

Leer-Andersen, M., Werner, S., Kim, K., 2018. Slutrapport För "Ytfriktionsdatabas För Maritima Sektorn. SSPA Report No RE40147243-02-00-A.

Ligrani, P.M., Moffat, R.J., 1986. Structure of transitionally rough and fully rough turbulent boundary layers. J. Fluid Mech. 69–98.

Marin, 2018. Numerical Uncertainty Analysis - User Manual. MARIN, The Netherlands.

Menter, F.R., 1993. Zonal two equation k-ω turbulence models for aerodynamic flows. In: 24th Fluid Dynamics Conference, Orlando. July 1993, AIAA paper-93-2906.

Nikuradse, J., 1950. Laws of Flow in Rough Pipes. Translation. National advisory committee for aeronautics, Washington, USA.

Oliveira, D.R., Granhag, L., Larsson, L., 2020. A novel indicator for ship hull and propeller performance: examples from two shipping segments. Ocean. Eng. 205, 107229. ISSN 0029-8018.

Orych, M., Werner, S., Larsson, L., 2021. Validation of full-scale delivered power CFD simulations, 2021 Ocean. Eng. 238, 109654. ISSN 0029-8018.

PETSc, 2020a. Petsc web page. https://www.mcs.anl.gov/petsc/index.html.

PETSc, 2020b. Petsc documentation, solvers. https://www.mcs.anl.gov/petsc/petsc-current/docs/manualpages/KSP/KSPGMRES.html.

PETSc, 2020c. Petsc documentation, preconditioners. https://www.mcs.anl.gov/petsc/petsc-current/docs/manualpages/PC/PCBJACOBI.html.

Queutey, P., Visonneau, M., 2021. Email Correspondence by the Author.

Roe, P.L., 1981. Approximate riemann solvers, parameter vectors, and difference schemes. J. Comput. Phys. 43, 357.

Schlichting, H., 1936. Experimental Investigation of the Problem of Surface Roughness. NACA TM-832.

Schlichting, H., 1979. Boundary-layer Theory, seventh ed. McGraw-Hill, New York.

Schultz, M., Flack, K., 2007. The rough-wall turbulent boundary layer from the hydraulically smooth to the fully rough regime. J. Fluid Mech. 580, 381–405. https://doi.org/10.1017/S0022112007005502.

Wilcox, D.C., 1998. Turbulence Modeling for CFD, second ed. DCW Industries Inc., LaCañada, California.

Paper II

Validation of full-scale delivered power CFD simulations

M. Orych, S. Werner, L. Larsson

Ocean Engineering 238 (2021)

10.1016/j.oceaneng.2021.109654

Ocean Engineering 238 (2021) 109654

Contents lists available at ScienceDirect

Ocean Engineering

journal homepage: www.elsevier.com/locate/oceaneng

Validation of full-scale delivered power CFD simulations

Michal Orych [a,c,*], Sofia Werner [b], Lars Larsson [a]

[a] Department of Mechanics and Maritime Sciences, Chalmers University of Technology, Gothenburg, Sweden
[b] SSPA AB, Gothenburg, Sweden
[c] FLOWTECH International AB, Gothenburg, Sweden

ARTICLE INFO

Keywords:
Delivered power
Full-scale
Hull roughness
Self-propulsion
Uncertainty
Validation
Verification
CFD

ABSTRACT

Verification and Validation of CFD simulations of delivered power at full-scale are carried out for a single screw cargo vessel. Numerical simulations are performed with a steady-state RANS method coupled with a body force propeller model based on a lifting line theory. There are no significant differences in the uncertainty levels between model and full-scale computations. The finest grid exhibits the numerical uncertainty of 1.40% at full-scale. Computed results are compared with sea trial data for three sister ships. Special attention is paid to the effect of roughness on the hull and propeller. The comparison error for the delivered power is about 1% which is significantly lower than the experimental uncertainty.

1. Introduction

The ship speed-power performance is usually one of the most important factors for a ship operator. At the moment, only model test based predictions are widely accepted for large and expensive projects. In the marine industry computational fluid dynamics, CFD, has been successfully applied to model scale simulations for many years. The availability of validation data, both open and proprietary, makes it relatively easy to develop the best practice and use the method for ship design. It is more difficult to predict the propulsion power at full-scale. In some cases, it is necessary to simulate at the correct Reynolds number due to the flow characteristics, while in other cases the designers wish to achieve better designs without extrapolating from a model scale. Accessible full-scale measurements of good quality are still scarce. Most data comes from sea trials, which are often carried out only at ballast draught, or from monitoring systems on ships in operation. In principle, both can be used for validation purposes. The problems are that the data is most of the time strictly confidential and/or difficult to process due to the uncertainties linked to the measurement accuracy and condition details. In recent years, an increased interest is observed in full-scale simulations. This is due to advancements in numerical methods, more powerful computers as well as trust that the CFD has gained through for example the series of Workshops on CFD in Ship Hydrodynamics initiated in 1980, Hino et al. (2020). However, even as recently as in 2008 (Raven et al., 2008) concluded that a prediction of the full-scale power entirely based on CFD is still not reliable enough when high accuracy is required. The importance of CFD simulations at full-scale was highlighted later in Hochkirch and Mallol (2013) and a practical example illustrated by Kim et al. (2014). In both papers the advantage of full-scale simulations and optimizations of hulls and appendages are shown. Lloyd's Register's full-scale numerical modelling workshop has recently contributed with an open test case for validations. The workshop results were summarized by Ponkratov (2017). Further analysis of the published results, shows that the mean comparison error of the predicted power is 13% for all submitted results and 3 out of 27 participants had errors below 3% for all considered speeds. A thorough study of the numerical accuracy both at model and full-scale can be found in Eça et al. (2010) and Pereira et al. (2017) for a large number of turbulence models without wall functions. However, the papers contain no full-scale validation.

In this work, carefully selected data from an established operator for a large number of sister ships is collected and used for validation. The RANS method, used for simulations, incorporates the wall roughness modelling without the need for wall functions. Therefore, the numerical challenge is greater than the works presented earlier. However, there is also a potential for more accurate predictions. An uncertainty study is presented, which is often lacking in other publications.

The paper first gives a brief introduction to the numerical method used in the code. Thereafter, the case and computational setup are described. The verification, a process which is used to determine numerical errors, is presented. In the validation section only full-scale measurements are used. Model-scale data are not shown for the confidentiality reasons. In connection with the validation, the hull roughness

* Corresponding author at: Department of Mechanics and Maritime Sciences, Chalmers University of Technology, Gothenburg, Sweden.
E-mail address: michal@flowtech.se (M. Orych).

https://doi.org/10.1016/j.oceaneng.2021.109654
Received 3 March 2021; Received in revised form 3 July 2021; Accepted 7 August 2021
Available online 1 September 2021

Nomenclature

ω	Specific turbulence dissipation
C_F	Frictional resistance coefficient
C_P	Pressure resistance coefficient
C_T	Total resistance coefficient
C_W	Wave resistance coefficient
E	Comparison error
k	Turbulent kinetic energy
K_Q	Torque coefficient
k_S	Equivalent sand grain roughness height
K_T	Thrust coefficient
n	Propeller revolution rate
n_g	Number of grid cells
p	Observed order of accuracy
P_D	Delivered power
U_D	Experimental uncertainty
U_G	Grid uncertainty
U_{SN}	Numerical uncertainty
U_{Val}	Validation uncertainty
w_n	Nominal wake

is discussed and an explanation of the current approach is given. The full-scale delivered power CFD predictions are presented and compared to the collected sea trial measurements. The final section discusses additional errors resulting from the numerical methods, physical modelling and input data.

2. Numerical method

The commercial CFD software SHIPFLOW is used for the simulations. It includes several flow solvers, Broberg et al. (2007). The potential flow solver (XPAN) and the RANS solver (XCHAP) were used in the present study.

XPAN is a non-linear Rankine source panel method, Janson (1997). It uses higher-order panels and singularity distributions. Non-linear boundary conditions are used for the free surface. Dynamic sinkage and trim are computed during the iterative procedure for the non-linear free surface boundary condition. During each iteration, the ship is repositioned and the panellization of the hull and free surface is regenerated.

XCHAP solves the steady, incompressible Reynolds Averaged Navier–Stokes equations using a finite volume method. The explicit algebraic stress turbulence model, EASM, Deng et al. (2005), is used in the present paper. No wall functions are used, and the equations are integrated down to the wall. The equations are discretized using the Roe scheme, Roe (1981), for the convection, while a central scheme is used for the diffusive fluxes. An explicit flux correction is applied to achieve second-order accuracy, Dick and Linden (1992) and Chakravarthy and Osher (1985).

The hull roughness effect is modelled by a modification of the boundary conditions for the specific dissipation of the turbulent kinetic energy, ω and the turbulent kinetic energy, k, Orych et al. (2021). The roughness is quantified using the equivalent sand grain roughness height, k_S .

XCHAP uses structured grids. A single block grid is typically generated for a bare hull case. Multi-block structured or overlapping grids are applied for more complex geometries such as hulls with appendages, and local grid refinements. The solver is flexible in terms of H/C/O grid topologies, and it can handle grid point and line singularities at the boundary surfaces, as well as folded and periodic grids.

To simulate the effect of the propeller, body forces are introduced. When the flow passes through the propeller swept volume, its linear and angular momentum increase as if it had passed a propeller with an infinite number of blades. The forces vary in space, but are independent of time, and generate a propeller induced steady flow. The body forces are computed with a built-in lifting line propeller analysis program, Zhang (1990). Additionally, a friction resistance component is accounted for that contributes to the propeller torque. This simple modelling is also used to take into account the blade roughness.

The computation of the body forces is embedded in an iterative procedure, where first the current approximation of the velocity field is extracted at a representative propeller plane. The effective wake is thereafter obtained by subtracting the induced propeller wake. This is the function of the propeller code and is computed by the circulation from the previous iteration in the lifting line method. The new circulation and forces are computed in the effective wake. Thereafter the forces are distributed over the volume cells in the cylindrical grid. The body forces are added to the right-hand side of the flow equations. This will give a new velocity field after solving the equations. The body forces are updated in every iteration. At convergence, the total wake computed by the RANS solver and the lifting line method should match in the selected propeller plane.

To simulate self-propulsion, the program automatically adjusts the propeller rotational speed to achieve a balance between resistance and thrust. For the model scale simulations, an allowance force can be given or computed according to the 1978 ITTC Performance Prediction Method, ITTC (2017a).

The momentum and continuity equations are solved in a coupled manner, while the turbulent quantities are solved separately. A Krylov type solver from the PETSc software suite, PETSc (2020a), is used to solve the linear equations. The selected GMRES, PETSc (2020b), with the block Jacobi preconditioner, PETSc (2020c), is in this case very efficient, both in terms of convergence speed and stability.

3. Case description

The test case for this validation was carefully selected to get a high-quality reference. It is a conventional single screw cargo vessel with Lpp about 180 m, beam 30 m and block coefficient of 0.78. However, most of the data is confidential. Therefore, not all details can be included in the paper. A full set of towing tank and sea trial measurements is available. The model tests are performed for both resistance and self-propulsion with a hull length of 7 m.

A large number of these ships were built, and the measurements for the validation come from 12 sister ships. This substantially increases the reliability of the full-scale data. The collected measurements were obtained during the sea trials upon delivery from the yard. They are post-processed according to the ITTC procedure for sea trials analysis, ITTC (2017a). Environmental effects such as wind, waves and currents are eliminated for a fair comparison with the numerical predictions, performed with a steady-state code. The design draught and the 12.5 knots speed corresponding to Reynolds number of approximately 8.5×10^6 and 9.6×10^8 in model and full scale respectively are used in the verification computations. For the validation, additional speeds are added, 13.5 and 14.5 knots.

4. Computational setup

The computational setup follows the current best practice for SHIPFLOW. Two different methods are used to obtain the solution. The nonlinear potential flow method, XPAN module, is used to compute the wave pattern, dynamic sinkage and trim. The wave resistance is evaluated using a wave-cut integration method.

The viscous pressure resistance and friction are computed using the RANS method XCHAP. For this computation, an H-O structured background grid describing the hull is complemented with overlapping

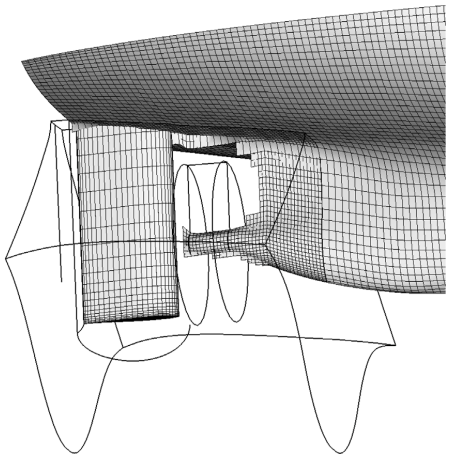

Fig. 1. Overlapping grid assembly. Surface mesh for hull, local refinement and rudder are visualized. Grid block outlines are visible for rudder, local refinement and propeller components.

component grids. The domain extends 0.8 Lpp in front of and behind the hull and the outer radius of the semi-cylindrical domain is 3.0 Lpp. Behind the submerged part of the transom a separate grid block is used. An additional cylindrical domain represents the propeller. The separate rudder grid is of O-O type. Both the propeller and the rudder are encapsulated within a local refinement that is based on the background grid, where each cell is split to generate eight new cells. Bilge keel geometry is not included in the simulations. An example grid assembly is shown in Fig. 1. It should be noted that in the RANS simulations the free surface effects are not taken into account and a double-model approach with a slip boundary condition at the water plane is used. Simulations performed using a viscous free-surface flow variant of the code confirm a limited interaction between the wave pattern and the viscous flow. Therefore, the double-model approximation can be applied in this case. However, the dynamic sinkage and trim computed by the potential flow method is taken into account. A detailed description of the applied boundary conditions is given in Broberg et al. (2007).

The simulations are performed with the fluid properties corresponding to the towing tank test conditions at model scale, and 15 °C seawater at full scale. In both model and full scale, the hull is considered hydraulically smooth in the grid dependency study. The hull roughness modelling at full scale is used in the final validation only.

5. Verification

Verification is carried out to investigate the numerical accuracy. It covers towed and self-propelled cases at a model and full scale. Although, the main focus of the paper is the full-scale, the verification at both scales is presented since there is much more experience from model scale simulations in the ship hydrodynamics community. Therefore, one can easily judge the quality of the presented results. The second reason is that the code behaviour at full scale can be compared to the model scale for reference.

Due to the hybrid RANS and potential flow approach the verification process is divided into numerical uncertainty estimations for the RANS solver and the potential flow solver separately. In all RANS computations, the potential flow meshing is unchanged. A separate test, described in the discussion section, is done to estimate the potential flow mesh sensitivity. This approach is adopted since there might be a reason to question mesh refinement studies for free surface potential flow solvers. The problem is that refining the free surface spatial discretization in a potential flow panel method will lead to the point where breaking waves start appearing. This means that a new physical phenomenon appears in the solution, which cannot be resolved with the potential flow method and causes the solver to fail.

Table 1
Cell sizes in selected regions for the optimized cell distribution, non-dimensionalized with Lpp.

Grid	Length-wise		Girth-wise	y^+
	forebody	aftbody	midship	midship
1	0.58×10^{-3}	0.41×10^{-3}	1.50×10^{-3}	0.495
6	1.38×10^{-3}	0.97×10^{-3}	3.57×10^{-3}	1.177

For the RANS grid dependency study, the calculations are performed in several steps to find the most suitable grid distribution and also to investigate the effect of overlapping grids on the results. Before generating the set of geometrically similar grids the sensitivity of the solution to a varying number of cells in the girth-wise, normal and length-wise directions in several regions along the hull is studied. In this way, a more balanced distribution of cells is found, that provides a good description of the flow without the need to overspend the computational resources. Thereafter, two sets of systematically varied grids are studied for initial and optimized cell distributions. It is found that the results converge with an increasing number of cells to similar values for both sets of grids. However, the optimized one shows monotonic convergence for a lower total amount of cells.

The grid refinement ratio is $\sqrt[4]{2}$ in each direction and the total number of cells range from 2.03×10^6 to 25.54×10^6, and from 3.77×10^6 to 44.14×10^6 at model and full scale respectively. The cell sizes in selected regions for the optimized cell distribution for the finest (#1) and coarsest (#6) grids are given in Table 1. The length and girth-wise sizes are non-dimensionalized by Lpp. It should be noted that the aftbody cell size in the length-wise direction is given in a region where the overlapping grid refinement is used. The number of cells in the normal direction for the full-scale simulations is about 65% larger compared to the model scale, to compensate for the clustering of cells close to the hull, due to the stretching necessary to keep y^+ according to the requirements of the turbulence model.

The simulations are executed for a bare hull grid first, then the rudder and refinement grids are added in subsequent steps. In all cases a similar level of uncertainties is observed, leading to the conclusion that the overlapping grid algorithm has a very limited impact on the overall result quality. One very important observation, that confirms earlier experience, Korkmaz (2015), is that for self-propulsion computations the refinement in the volume surrounding the propeller is necessary to avoid a scatter, visible as an oscillatory grid convergence. If the embedding grid is not fine enough, especially in the axial direction, the insufficiently accurate interpolation of the forces introduced by the propeller leads to increased uncertainty of the propulsive factors.

The least square root, LSR, method is used to determine the numerical uncertainty and the order of accuracy, Eça and Hoekstra (2014). A software tool prepared by MARIN, MARIN (2018), is used to process the results.

5.1. Model scale

The model scale towed condition results are given in Table 2. The total resistance coefficient, as well as frictional and viscous pressure components and nominal wake fraction, are presented. C_F increases, while C_P decreases with grid size, which seems to be a feature of the solver. All variables converge well with limited scatter. In the case of C_F and C_T the observed order of accuracy, p, is above the limit suggested by Eça; hence it is set to 2.0. See, Eça and Hoekstra (2014). The grid uncertainty, U_G, is expressed as a percentage of the solution from the finest grid, S_1.

Table 2
Resistance component coefficients and nominal wake of towed hull, model scale.

Grid	$C_F \times 10^{-3}$	$C_P \times 10^{-3}$	$C_T \times 10^{-3}$	w_n
1	3.043	0.470	3.631	0.2135
2	3.034	0.477	3.628	0.2136
3	3.024	0.480	3.621	0.2145
4	3.002	0.494	3.613	0.2153
5	2.968	0.506	3.592	0.2165
6	2.910	0.522	3.549	0.2175
p	2.0	1.2	2.0	1.5
$U_G\%S_1$	3.1	7.0	1.7	0.9

Table 3
Uncertainty and deviations of total resistance coefficient, model scale.

Grid	$n_g \times 10^6$	$C_T \times 10^{-3}$	$U_G\%S_i$	$\lvert C_{Ti} - C_{T0}\rvert \%C_{T0}$
0	∞	3.652	–	–
1	8.99	3.631	1.7	0.6
2	5.42	3.628	2.1	0.7
3	3.27	3.621	3.0	0.9
4	1.97	3.613	4.3	1.1
5	1.19	3.592	5.8	1.6
6	0.73	3.549	8.2	2.8

Table 4
Resistance component coefficients of self-propelled hull, model scale.

Grid	$C_F \times 10^{-3}$	$C_P \times 10^{-3}$	$C_T \times 10^{-3}$
1	3.150	0.794	4.061
2	3.142	0.800	4.059
3	3.136	0.812	4.065
4	3.124	0.819	4.060
5	3.109	0.851	4.077
6	3.093	0.868	4.077
p	1.4	1.7	1.1
$U_G\%S_1$	1.1	3.6	1.3

Table 3 contains C_T results obtained for all grid sizes, n_g, as well as the value extrapolated to an infinite number of cells. Since it is often not practical to use the finest grid that was included in the verification study, the uncertainties for coarser grids are also very important, here expressed as a percentage of the solution for each grid, S_i. The last column can be of particular interest to the designers. It shows a difference between C_{T0}, the value extrapolated to zero step size, and each grid result, C_{Ti}, in percent of C_{T0}. The total resistance average comparison error, $|E|$%D, is about 1% for all three speeds that are considered.

The propeller action in the self-propulsion case seems to stabilize the flow and the resistance components show lower uncertainty, Table 4. For a better perception of the data, the results are also plotted in Fig. 2. The horizontal axis represents the relative step size between the grids. The resistance coefficients indicate monotonous grid convergence with small uncertainties and limited scatter.

Also, the propulsive factors behave well, and the delivered power converges at a nearly theoretical rate for this method and with small scatter, Table 5.

The deviation from the value extrapolated to the infinitesimally fine grid is 0.15% for the finest grid and the maximum is 0.67% for the second coarsest one, Table 6. The last column shows a difference between the extrapolated value of P_{D0} and each grid result, P_{Di}, in percent of P_{D0}. The same values of $U_G\%S_i$ for all grids are the result of the used verification method and its specific evaluation process. For a detailed description the reader is referred to Eça and Hoekstra (2014).

5.2. Full scale

The resistance components and nominal wake for the "towed" full-scale case are given in Table 7 only for reference, as these quantities

Table 5
Propulsive factors, model scale.

Grid	K_T	$K_Q \times 10^{-1}$	n [rps]	P_D [W]
1	0.13885	0.1957	6.576	35.03
2	0.13886	0.1957	6.573	34.99
3	0.13888	0.1958	6.580	35.11
4	0.13930	0.1963	6.564	34.94
5	0.13991	0.1970	6.573	35.21
6	0.14041	0.1975	6.561	35.12
p	2.0	2.0	2.0	1.8
$U_G\%S_1$	1.0	0.8	0.6	2.3

Table 6
Uncertainty and deviations of delivered power, model scale.

Grid	$n_g \times 10^6$	P_D [W]	$U_G\%S_i$	$\lvert P_{Di} - P_{D0}\rvert \%P_{D0}$
0	∞	34.98	–	–
1	25.54	35.03	2.3	0.15
2	15.27	34.99	2.3	0.04
3	9.17	35.11	2.3	0.38
4	5.54	34.94	2.3	0.10
5	3.32	35.21	2.3	0.67
6	2.03	35.12	2.3	0.41

Table 7
Resistance component coefficients and nominal wake of towed hull, full scale.

Grid	$C_F \times 10^{-3}$	$C_P \times 10^{-3}$	$C_T \times 10^{-3}$	w_n
1	1.616	0.257	1.991	0.1270
2	1.612	0.265	1.993	0.1276
3	1.609	0.270	1.996	0.1286
4	1.600	0.289	2.006	0.1304
5	1.593	0.311	2.021	0.1324
6	1.582	0.340	2.039	0.1342
p	1.6	2.0	2.0	1.3
$U_G\%S_1$	0.9	8.7	1.9	3.8

Table 8
Resistance component coefficients of self-propelled hull, full scale.

Grid	$C_F \times 10^{-3}$	$C_P \times 10^{-3}$	$C_T \times 10^{-3}$
1	1.655	0.532	2.304
2	1.650	0.538	2.305
3	1.647	0.549	2.312
4	1.638	0.566	2.321
5	1.629	0.592	2.337
6	1.617	0.619	2.353
p	1.5	1.9	2.0
$U_G\%S_1$	1.1	5.5	1.6

are in practice not measured. The uncertainties are at a similar level to those observed at model scale.

In Table 8 the results from the grid dependence study for resistance components of a self-propelled case are shown. The results are also plotted in Fig. 3. It can be noticed that the scatter at full-scale is not larger than in the model-scale.

Small uncertainties can also be observed for all propulsive factors, see Table 9. Values well below 1% are seen for K_T, K_Q and n.

For the finest grid the delivered power grid uncertainty, $U_G\%S_1$ is 1.4% and the deviation from the extrapolated value, $\lvert P_{D1} - P_{D0}\rvert \%P_{D0}$, is 0.49%, see Table 10.

The results for K_T, K_Q and n are plotted for all grids as a function of the relative grid size in Fig. 4, and P_D in Fig. 5.

All the above verification results are given for a smooth hull. Further calculations with roughness show that the applied modelling does not seem to increase the scatter in the solutions and the uncertainties are very similar, therefore only one set of data is presented.

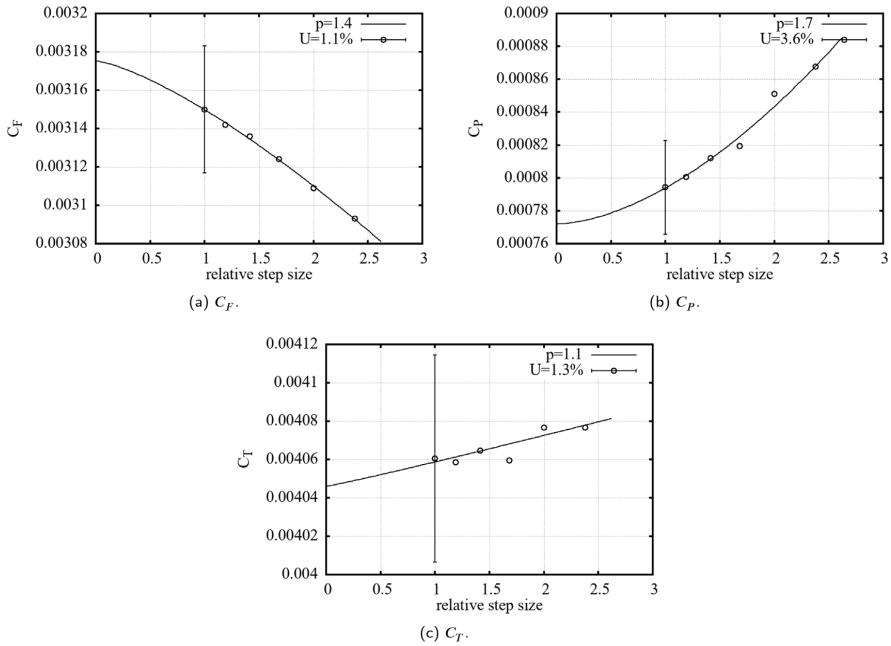

Fig. 2. Grid convergence of frictional, viscous pressure and total resistance coefficients, self-propelled case, model-scale.

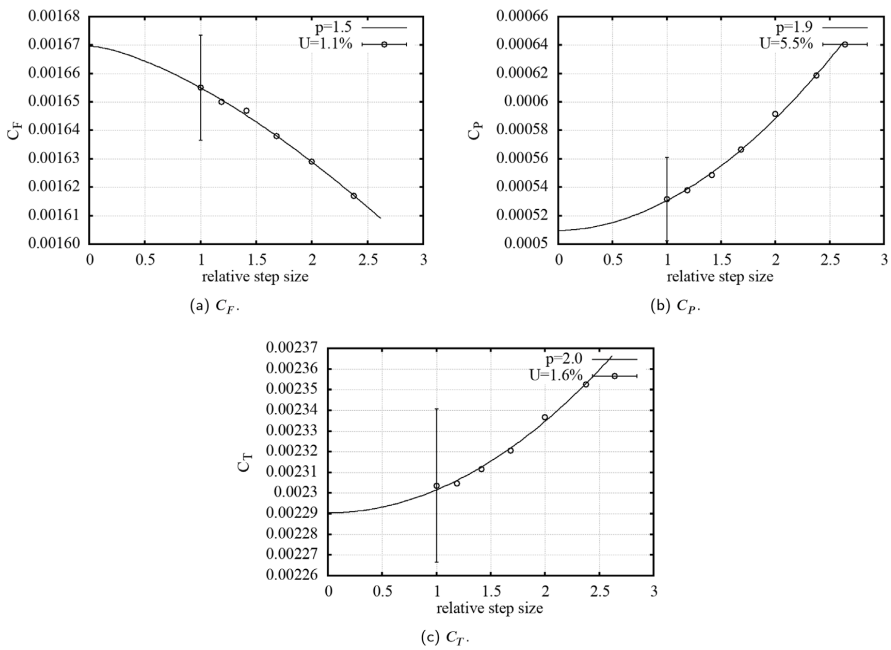

Fig. 3. Grid convergence of frictional, viscous pressure and total resistance coefficients, self-propelled case, full-scale.

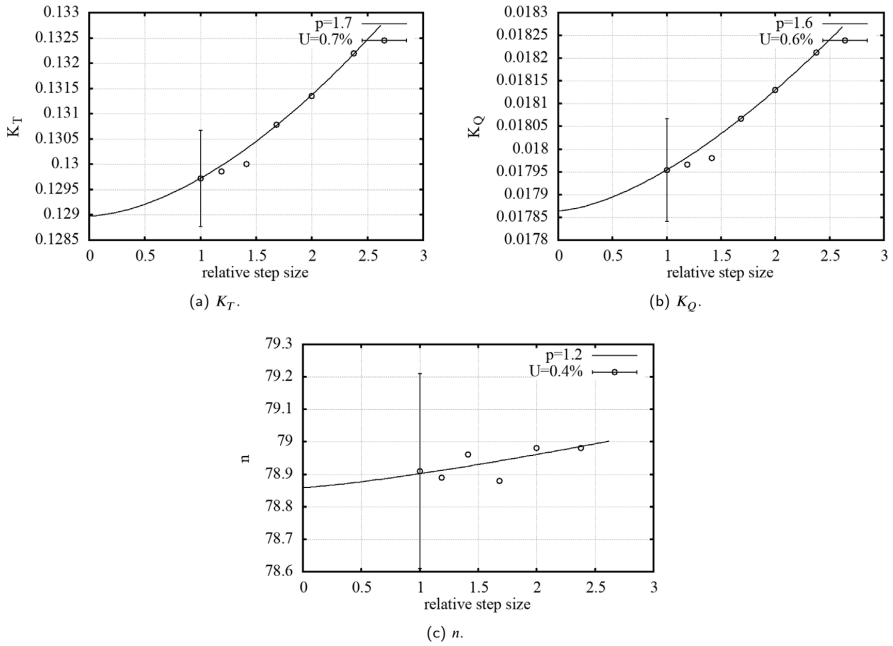

(a) K_T. (b) K_Q. (c) n.

Fig. 4. Grid convergence of propulsive factors, full scale.

Table 9
Propulsive factors, full scale.

Grid	K_T	$K_Q \times 10^{-1}$	n [rpm]	P_D [MW]
1	0.1297	0.1795	78.91	3.055
2	0.1299	0.1797	78.89	3.054
3	0.1300	0.1798	78.96	3.066
4	0.1308	0.1807	78.88	3.070
5	0.1313	0.1813	78.98	3.093
6	0.1322	0.1821	78.98	3.108
p	1.7	1.6	1.2	2.0
$U_G\%S_1$	0.7	0.6	0.4	1.4

Table 10
Uncertainty and deviations of delivered power, full scale.

Grid	$n_g \times 10^6$	P_D [MW]	$U_G\%S_i$	$\lvert P_{Di} - P_{D0}\rvert \%P_{D0}$
0	∞	3.040	–	–
1	44.14	3.055	1.40	0.49
2	26.61	3.054	1.92	0.45
3	16.26	3.066	2.56	0.85
4	9.97	3.070	3.65	0.98
5	6.02	3.093	5.03	1.74
6	3.77	3.108	6.90	2.23

6. Validation

The computations for the verification part are performed with some simplifications to isolate potential sources of scatter in the numerical solution. To validate the computed results with the measurements the ship geometry and conditions have to be represented as accurately as possible and the missing drag sources need to be recognized and included in the final results. The roughness effects on the hull and propeller at full scale are computed using the model implemented in the RANS code. The aerodynamic resistance is added using the ship frontal area and a coefficient provided by the model testing facility. There is also an addition of the bilge keel drag.

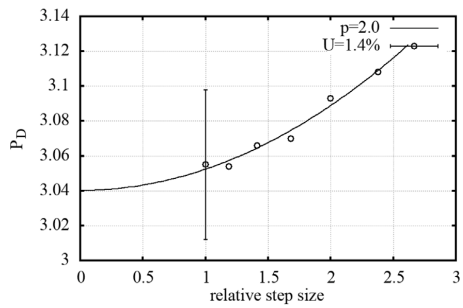

Fig. 5. Grid convergence of delivered power, full-scale.

Considering the computational effort the fourth finest grid is used in the validation. The delivered power difference between the finest setup with over 44×10^6 cells and the selected one with about 10×10^6 is less than 0.5%, Table 10.

6.1. Hull roughness

The added resistance due to the hull roughness can significantly increase the power demand. Even a newly painted surface may exhibit roughness large enough to raise the fuel consumption a few percent compared to a hydraulically smooth surface.

The topological properties of the rough surfaces are often described with only a single parameter. One example used in ship hydrodynamics is the average hull roughness, *AHR*, see Townsin et al. (1981). In many CFD methods, the roughness models also use a single number description in the form of an equivalent sand roughness, k_S. The numerical models are often tuned to represent certain measurements.

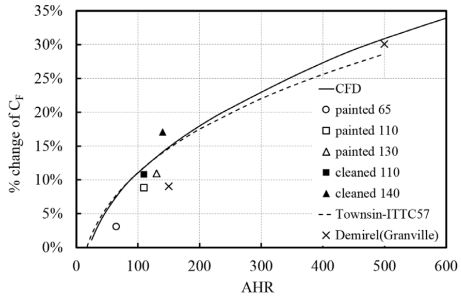

Fig. 6. Comparison of CFD simulations ($AHR/k_S = 5$) with Granville/Grigson extrapolated rough flat plates and Townsin estimated increase of C_F. KCS conditions, L = 230 m, $Rn = 2.89 \times 10^9$.

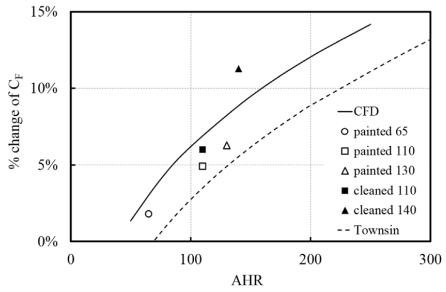

Fig. 7. Comparison of CFD simulations ($AHR/k_S = 5$) with Granville/Grigson extrapolated rough flat plates and Townsin estimated increase of C_F. Current hull conditions, L = 180 m, $Rn = 9.7 \times 10^8$.

Therefore, there is a large number of models available and more are being developed to suit specific surface types and conditions. Some of them were studied in Orych et al. (2021), where their different behaviours were presented. For the currently available models, the remaining challenge is the correlation between the two measures, namely *AHR* and k_S.

In the ITTC extrapolation method, Townsin's formula for added resistance due to roughness is used, ITTC (2017b). It is quite instinctive for a naval architect to cross-check the CFD results against this solution. Plotting the increase in frictional resistance as a function of average hull roughness, $\Delta C_F(AHR)$, based on Townsin's method together with computed increase as a function of equivalent sand roughness, $\Delta C_F(k_S)$, should help to find the relation between the *AHR* and k_S. As the first example, a flat plate with length and speed corresponding to the Kriso Container Ship (KCS), Hino et al. (2020), is considered. Using the AHR/k_S factor of 5 yields nearly perfect correlation between the Aupoix-Colebrook model, Aupoix (2014) and Townsin's method up to the suggested maximum of 230 μm for the latter one, see Fig. 6. However, repeating the exercise for the present ship, which is shorter and slower, the results are disappointing. Quite different curves are noticeable in Fig. 7. Decreasing length and speed further, shows that the roughness limit for a "hydraulically smooth surface" based on Townsin's formula is unreasonably high and may lead to underestimation of the resistance due to roughness in such applications.

The second approach to find the AHR/k_S correlation is based on experimental results for a flat plate. The measurements of several painted surfaces are extrapolated to full-scale length with Granville's method and to appropriate speed with Grigson's method with help of SSPA's Skin Friction Database tool, Leer-Andersen (2020). In this case, both newly painted plates and cleaned ones after deployment in the sea are used. The *AHR* for these samples is from 65 to 140 μm. For the same correlation factor that seemed to be suitable for Townsin's formula in case of the conditions similar to the KCS, the extrapolated measured values and CFD results show a good level of consistency for both ships, Figs. 6 and 7. Considering the fact that the experiments which constitute the basis of the roughness models implemented in the CFD code are based on different surface roughness types, the agreement is satisfactory and seems more reliable than Townsin's formula. For the KCS case, the results from other extrapolated measurements described by Demirel et al. (2017) are shown in Fig. 6.

It has to be highlighted that there is no universal AHR/k_S correlation factor, not only due to the numerical models but also since the rough surface topology cannot be adequately represented by a single number. A good example of that is the significant difference in C_F change between the newly painted, aged and subsequently cleaned surfaces with the same *AHR*, which can also be seen in the figures. The full-scale data considered in this work is based on delivered power measurements of ships during sea trials. The average hull roughness was reported but there is no detailed description of the surface texture. Therefore, the Aupoix-Colebrook roughness model with $AHR/k_S = 5$, which indicates conservative values of resistance increase is selected.

6.2. Full-scale measurements and post-processing

It is notoriously difficult to obtain sea trial data from a shipowner by a third party. Even more problematic is to get good quality materials with accurate measurements and proper records of the procedure. In this case, the authors are fortunate to gain access to a well-documented set of measurements for 12 sister ships.

The trials are performed according to the ITTC procedure, ITTC (2017c), also included in ISO 15016 standard. Three power settings are included and data acquired for power, speed, propeller rate of revolution, wind, waves, current and temperature, among others. Corrections are applied for wind, waves, current and temperature effects. In connection to the trial runs the Average Hull Roughness is measured.

Three sister vessels are selected based on the conditions during the measurements. These are tested at design draught in nearly perfect weather conditions, which minimize the measurement and correction errors. Therefore, the resulting measurement uncertainty is at a level allowing for proper validation of the CFD simulations.

6.3. Full-scale predictions

The most important part of this investigation is a full-scale self-propulsion simulation. It is performed at speeds of 12.5, 13.5 and 14.5 knots. This range includes the available sea trial runs for the selected cases. In the computations, the roughness effects are taken into account and the *AHR* is set to 100 μm, according to the average of the measured values. The windage is computed using the frontal ship area and a resistance coefficient suggested by the towing tank performing the model tests. To estimate the drag of the bilge keels, their wetted area and the frictional resistance coefficient for the bare hull are used. Both are added as an additional resistance during the self-propulsion simulation. To account for the propeller roughness a value of 30 μm, indicated by ITTC extrapolation method is used. The delivered power from the sea trials and SHIPFLOW simulations are presented in Fig. 8.

The curve fitting of the sea trial data is done according to the ITTC recommendations, ITTC (2017c). Thus, a curve representing the mean value of the two available towing tank predictions is shifted vertically such that the Root-Mean-Square (RMS) error of the data points is minimized. The Normalized RMS Error is 2.8%. Included in the plot are also the uncertainties estimated for the sea trials and the CFD results. A band of ±6.1% represents the experimental uncertainty, U_D, which can be expected from these sea trials. It is computed based on the sea trial uncertainties presented by Werner and Gustafsson (2020), where, for

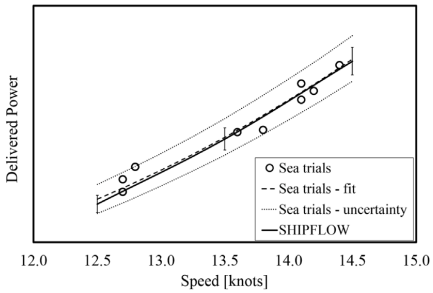

Fig. 8. Delivered power for sea trials and CFD simulations.

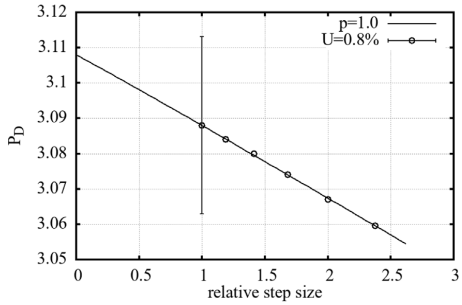

Fig. 9. Potential flow grid variation. Effect on delivered power.

Table 11
Measurement uncertainty and differences between CFD simulations and sea trial data fit for delivered power.

Speed	P_D	
[knots]	$\|E\|$%D	U_{Val}%D
12.5	1.9	7.1
13.5	0.6	–
14.5	0.5	–

good weather conditions during trials, the precision uncertainty is 8% for each individual point. The uncertainty of the mean value is obtained by dividing by the square root of the number of sister ships, Farrance and Frenkel (2012), resulting in a precision error, P, of 4.6% for this case. Furthermore, according to, Insel (2008) the expected bias error, B, for delivered power is at a level of 4%. P and B can be combined to obtain $U_D = \sqrt{P^2 + B^2}$. As it can be recalled from the verification part in this paper, the delivered power numerical uncertainty, U_{SN}, is 3.65% for the grid size used in the simulations. It is estimated at 12.5 knots of speed and is assumed to be similar at 13.5 and 14.5 knots.

According to the ITTC (2017d) a computation is considered validated at the U_{Val} level if the comparison error, $|E|$, is smaller than U_{Val}:

$$|E| < U_{Val} = \sqrt{{U_{SN}}^2 + {U_D}^2}$$

To assess the comparison error of the validation, E, the differences between computed results and the sea trial data fit are calculated and expressed in percent of the latter one, D, Table 11. The computed delivered power errors are much smaller than the validation uncertainty. Therefore, the simulations may be considered validated at the U_{Val} level (7.1%). It is worth noting that the numerical uncertainty is lower than, and entirely within, the experimental uncertainty.

No validation of the propeller rate of revolution is presented since there is not sufficient data to estimate the bias error and there is a strong impression that the propeller pitch was modified compared to the initial design to adjust the RPM to better match the engine characteristics.

7. Discussion

There are three types of errors in a computation, Coleman (2009): numerical errors, physical modelling errors and errors in input data. The numerical errors (including discretization scheme) are investigated through grid dependence studies. The physical errors stem from different sources: turbulence model, boundary conditions, propeller model, free surface approximation, roughness modelling and in the present case the modelling of bilge keels, and air resistance. The input data errors are related to the CAD description of the hull. All these errors but the turbulence model and the boundary conditions are discussed here.

The grid dependency study presented in Verification section is done only for the RANS part of the solution. The wave resistance is computed with a separate potential flow method. In the verification and the validation described earlier, it is computed with a mesh that is set up based on many validations carried out since the method was developed. To complete the study and quantify the uncertainties associated with the potential flow solution a series of six meshes is prepared ranging from 9409 to 53 908 panels. The upper limit of this range is set by the onset of wave breaking and therefore inevitable convergence issues. This series of potential flow meshes is combined with the RANS grid with 10×10^6 cells. The P_D uncertainty due to the potential flow mesh size is in this setup 0.81% for the finest mesh, see Fig. 9. For the validation part where the fourth finest RANS and potential flow solutions are used the total P_D uncertainty is 3.90%. It is evaluated using the root sum of the squares with contributions from the viscous part that is 3.65% and potential flow part, 1.38%. Therefore, the uncertainty increase of 0.25% associated with the potential flow part of the solution does not change the overall conclusions. This is also in part due to the small wave resistance contribution to the total resistance, approximately 5% at 12.5 knots speed.

The numerical uncertainty includes both grid and iterative uncertainties. However, the simulations are carried out with very strict convergence criteria until the iterative errors are insignificant. For the grid with 10×10^6 cells the standard deviations of the integrated values calculated for the last 10% of iterations are below 0.03% for C_P, 0.01% for C_T, 0.005% for C_F, K_T, K_Q, n and P_D. This indicates that the iterative uncertainty is very small, and it is not included in the analysis.

When it comes to the hull roughness, the uncertainties lay on both experimental and numerical sides. The measured Average Hull Roughness is a single number that describes the hull condition. It does not take into account the local surface geometry, which influences the efficiency of the roughness elements to create disturbance in the flow. As seen in Figs. 6 and 7, a surface with the same AHR can give noticeably different resistance depending on whether the hull was freshly painted or cleaned. Also, the paint type would affect the resistance. The current numerical methods usually use an equivalent sand roughness that is not universally translatable from AHR. For these reasons, it is important to check how large an effect the AHR and AHR/k_S correlation factor would have on the results. Here, the AHR is varied by ±25% which is a spread between sister ships observed in the measurements. If this variation is associated with the correlation factor it creates an envelope in the change of C_F that contains all of the markers in Figs. 6 and 7. The delivered power change due to this variation is ±1.5%.

A similar study is also applied to the propeller roughness. This is realized by modification of the blade frictional coefficient introduced to the lifting line. The nominal propeller roughness is varied by as much as ±20% corresponding to the blades C_F change of ±5%. This results in ±0.9% difference in delivered power.

The estimation of air resistance is approximate as there are no wind tunnel measurements available. However, the air resistance is just 2.5% of the total resistance and therefore the contribution to the total uncertainty is expected to be less than 0.25% assuming the range of possible air resistance coefficients. In the same way, the resistance from the bilge keels is only roughly estimated. They contribute to 0.7% of the total resistance and the uncertainty introduced by this coarse approximation is considered marginal.

At the simulation preparation stage, it became obvious that the hull geometry described in the CAD model is not smooth and requires small corrections. This is not uncommon, and the computed hull shape and the built ship differ slightly. Furthermore, there is a small change introduced at the stern to the otherwise similar sister ships after several completed builds. This means that two slightly different hulls are used in the selected sea trials. The differences between the original, smoothened and modified hull shapes are investigated with CFD and the delivered power discrepancy between them is about 1.3%.

The above complementary studies of sensitivity to several important simulation parameters substantiate the confidence in the validity of the achieved numerical predictions accuracy at full scale.

8. Conclusions

The main objective of this paper is to present a validation of CFD simulations of delivered power for a full-scale ship. In addition, a verification of the numerical method through systematic grid refinement studies is presented both for model-scale and full scale. Numerical uncertainties are determined for the total resistance and its components, the propulsive factors, and the delivered power. The numerical uncertainty of the delivered power at model scale is 2.3% and at full-scale 3.7% for a medium size grid with ten million cells. In the full-scale validation, special emphasis is placed on the effect of the surface roughness, both of the hull and the propeller. The validation is based on sea trial results, where the experimental uncertainty is estimated to 6%. Together with the numerical uncertainty this gives a validation uncertainty of 7%. For the speed range from 12.5 to 14.5 knots the average comparison error is 1%, i.e. considerably smaller than the validation uncertainty.

CRediT authorship contribution statement

Michal Orych: Conceptualization, Methodology, Software, Validation, Visualization, Writing – original draft. **Sofia Werner:** Data Curation, Writing - review & editing. **Lars Larsson:** Supervision, Writing – review & editing.

Declaration of competing interest

Michal Orych reports financial support was provided by Energimyndigheten (Swedish Energy Agency). Michal Orych reports a relationship with FLOWTECH International AB that includes: board membership and employment.

Acknowledgements

The authors would like to thank: Energimyndigheten (Swedish Energy Agency) for the financial support and SSPA for providing highly valuable input on full-scale measurements. The computations were enabled by resources provided by the Swedish National Infrastructure for Computing (SNIC) at C3SE, partially funded by the Swedish Research Council through grant agreement no. 2016-07213.

References

Aupoix, B., 2014. Wall roughness modelling with $k-\omega$ SST model. In: 10th International ERCOFTAC Symposium on Engineering Turbulence Modelling and Measurements, Marbella, Spain.

Broberg, L., Regnström, B., Östberg, M., 2007. XCHAP – Theoretical Manual. FLOWTECH International AB, Gothenburg, Sweden.

Chakravarthy, S., Osher, S., 1985. A new class of high accuracy TVD schemes for hyperbolic conservation laws. In: 23rd Aerospace Sciences Meeting, Reno, NV, U.S.A.. AIAA paper No 85–0363.

Coleman, H., 2009. ASME V&V 20-2009 Standard for Verification and Validation in Computational Fluid Dynamics and Heat Transfer. The American Society of Mechanical Engineers, New York.

Demirel, Y.K., Turan, O., Incecik, A., 2017. Predicting the effect of biofouling on ship resistance using CFD. Appl. Ocean Res. 62, 100–118.

Deng, G.B., Queutey, P., Visonneau, M., 2005. Three-dimensional flow computation with Reynolds stress and algebraic stress models. In: Procedings of the ERCOFTAC International Symposium on Engineering Turbulence Modelling and Measurements; ETMM6, Sardinia, Italy, 23–25 May, 2005. pp. 389–398.

Dick, E., Linden, J., 1992. A multigrid method for steady incompressible Navier-Stokes equations based on flux difference splitting. Internat. J. Numer. Methods Fluids 14, 1311–1323.

Eça, L., Hoekstra, M., 2014. A procedure for the estimation of the numerical uncertainty of CFD calculations based on grid refinement studies. J. Comput. Phys. 262, 104–130.

Eça, L., Hoekstra, M., Raven, H., 2010. Quantifying roughness effects by ship viscous flow calculations. In: 28th Symposium on Naval Hydrodynamics, Pasadena, California, September 16, 2010.

Farrance, I., Frenkel, R., 2012. Uncertainty of measurement: A review of the rules for calculating uncertainty components through functional relationships. Clin. Biochem. Rev. 33, 49–75.

Hino, T., Stern, F., Larsson, L., Visonneau, M., Hirata, N., Kim, J., 2020. Numerical Ship Hydrodynamics. An Assessment of the Tokyo 2015 Workshop. In: Lecture Notes in Applied and Computational Mechanics, vol. 94, Springer Nature, Switzerland, http://dx.doi.org/10.1007/978-3-030-47572-7.

Hochkirch, K., Mallol, B., 2013. On the importance of full-scale CFD simulations for ships. In: 12th Conf. Computer and IT Applications in the Maritime Industries (COMPIT), Cortona, Italy. pp. 85–95.

Insel, M., 2008. Uncertainty in the analysis of speed and powering trials. Ocean Eng. 35, 1183–1193.

ITTC, 2017a. 1978 ITTC Performance Prediction Method, ITTC Quality System Manual, Recommended Procedures and Guidelines. Propulsion Committee of the 28th ITTC.

ITTC, 2017b. Proceedings of 25th ITTC – Volume II, Final Report and Recommendations to the 25th ITTC. The Specialist Committee on Powering Performance Prediction, Fukuoka, Japan.

ITTC, 2017c. Preparation, Conduct and Analysis of Speed/Power Trials, ITTC Quality System Manual, Recommended Procedures and Guidelines. Specialist Committee on Ships in Operation at Sea of the 29th ITTC.

ITTC, 2017d. Uncertainty Analysis in CFD Verification and Validation Methodology and Procedures, ITTC Quality System Manual, Recommended Procedures and Guidelines. Resistance Committee of the 28th ITTC.

Janson, C.-E., 1997. Potential Flow Panel Methods for the Calculation of Free-Surface Flows with Lift (Ph.D. thesis). Chalmers University of Technology, Gothenburg, Sweden.

Kim, K., Leer-Andersen, M., Orych, M., 2014. Hydrodynamic optimization of energy saving devices in full scale. In: Proceedings, 30th Symposium on Naval Hydrodynamics, Hobart, Tasmania, Australia.

Korkmaz, K.B., 2015. CFD Predictions of Resistance and Propulsion for the JAPAN Bulk Carrier (JBC) with and Without an Energy Saving Device (MSc Thesis). Chalmers University of Technology, Gothenburg, Sweden.

Leer-Andersen, M., 2020. Skin friction database. https://www.sspa.se/tools-and-methods/skin-friction-database/extrapolation-full-scale.

MARIN, 2018. Numerical Uncertainty Analysis – User Manual. MARIN, The Netherlands.

Orych, M., Werner, S., Larsson, L., 2021. Roughness effect modelling for wall resolved RANS – comparison of methods. in preparation.

Pereira, F., Vaz, G., Eça, L., 2017. Verification and validation exercises for the flow around the KVLCC2 tanker at model and full-scale Reynolds numbers. Ocean Eng. 129, 133–148.

PETSc, 2020a. PETSc web page. https://www.mcs.anl.gov/petsc/index.html.

PETSc, 2020b. PETSc documentation, solvers. https://www.mcs.anl.gov/petsc/petsc-current/docs/manualpages/KSP/KSPGMRES.html.

PETSc, 2020c. PETSc documentation, preconditioners. https://www.mcs.anl.gov/petsc/petsc-current/docs/manualpages/PC/PCBJACOBI.html.

Ponkratov, D., 2017. 2016 workshop on ship scale hydrodynamic computer simulations. In: Proceedings: Lloyd's Register's Full-Scale Numerical Modelling Workshop.

Raven, H.C., van der Ploeg, A., Starke, A., Eça, L., 2008. Towards a CFD-based prediction of ship performance —progress in predicting full-scale resistance and scale effects. Trans. RINA A 150, 31–42.

Roe, P.L., 1981. Approximate Riemann solvers, parameter vectors, and difference schemes. J. Comput. Phys. 43, 357.

Townsin, R., Byrne, D., Svensen, T., Milne, A., 1981. Estimating the technical and economic penalties of hull and propeller roughness. Trans. Soc. Nav. Archit. Mar. Eng. 89, 295–318.

Werner, S., Gustafsson, L., 2020. Uncertainty of speed trials. In: Proceedings of the HullPIC 2020, Hamburg, Germany. pp. 26–28.

Zhang, D.H., 1990. Numerical Computation of Ship Stern/Propeller Flow (Ph.D. thesis). Chalmers University of Technology, Gothenburg, Sweden.

Paper III

Speed and delivered power in waves—Predictions with CFD simulations at full scale

M. Orych, M. Östberg S., M. Kjellberg, S. Werner, L. Larsson

Ocean Engineering 285 (2023)

10.1016/j.oceaneng.2023.115289

Ocean Engineering 285 (2023) 115289

Contents lists available at ScienceDirect

Ocean Engineering

journal homepage: www.elsevier.com/locate/oceaneng

Speed and delivered power in waves — Predictions with CFD simulations at full scale

Michal Orych [a,d,*], Magnus Östberg [d], Martin Kjellberg [b], Sofia Werner [b], Lars Larsson [a,c]

[a] Department of Mechanics and Maritime Sciences, Chalmers University of Technology, Gothenburg, Sweden
[b] RISE Research Institutes of Sweden/SSPA Sweden AB, Gothenburg, Sweden
[c] International School of Yacht Design – ISYD AB, Sweden
[d] FLOWTECH International AB, Gothenburg, Sweden

ARTICLE INFO

Keywords:
Seakeeping
EEDI
Weather factor
Delivered power
Speed loss
Full-scale
Self-propulsion
validation
CFD

ABSTRACT

An efficient numerical method is proposed to estimate delivered power and speed loss for a ship in wind and waves. The added resistance in waves, obtained with an unsteady potential flow panel method, is added to the calm water resistance from a steady-state potential flow/RANS method coupled with a body force propeller model for self-propulsion. A comparison of numerical and experimental results is made for added resistance, calm water resistance and delivered power. A good agreement is obtained. As a practical application, the approach is used to calculate the weather factor, f_w, of the Energy Efficiency Design Index (EEDI). The calculated weather factor is consistent with the values derived from full-scale measurements included in a database of similar ships.

1. Introduction

Computational Fluid Dynamics (CFD) is presently an accepted tool for predicting calm water resistance and powering at model scale. The development of this area is well covered by the International Workshops on Numerical Ship Hydrodynamics, see Larsson et al. (2014) and Hino et al. (2021). However, to obtain full-scale data, the results have to be extrapolated. More recently, the interest has shifted towards direct full-scale predictions, and the currently most comprehensive validation exercise is performed within the Joint Research Project, "Development of Industry-Recognised Benchmark for Ship Energy Efficiency Solutions", JoRes (2023). In a recent paper, the authors also demonstrated the feasibility of this approach, Orych et al. (2021).

However, ship designers place greater emphasis on real-world conditions, which include environmental factors like wind and waves. Historically, seakeeping studies have primarily relied on experimental testing in towing tanks or model basins, but numerical predictions are becoming more and more popular. They can be used, for example, to estimate the weather factor (ITTC, 2021b), which is a part of the Energy Efficiency Ship Index (EEDI) (IMO, 2018), and they are accepted for computing the calm water reference speed for the Energy Efficiency Existing Ship Index (EEXI) (IMO, 2022).

A hierarchy of numerical methods for seakeeping performance is presented in Fig. 1, showing their level of approximation versus computational effort. At the far end of the x-axis is the simple frequency domain strip method, which is extremely rapid on today's computers. The next method is an extension to non-linear strip theory in the time domain. Then there are two 3D boundary element (BEM) methods, the first one being linear and the second one non-linear. The unsteady Reynolds-Averaged Navier–Stokes (RANS) method is next. It introduces a more physically accurate representation of reality but requires much more computational effort than the non-linear BEM. At the most exact end of the graph, there is Large Eddy Simulation, LES, which is still too expensive to be applied in the industry, and Direct Numerical Simulation, DNS, entirely out of reach for practical applications.

At present, the best compromise between accuracy and computational demands are the RANS and non-linear BEM methods. While the former is more popular, there is a rather severe limitation in the number of computations that can be carried out in a reasonable time. A hybrid method was proposed by Kim et al. (2017), who used linear 2-D and 3-D potential flow methods, as well as unsteady RANS, to evaluate added resistance in waves, but the calm water resistance and speed loss in waves were estimated with simplified methods. Saettone (2020) used an unsteady potential flow 6DOF method combined with a double-model RANS code coupled with a propeller analysis tool based on a boundary-element method. His work indicates that this approach could determine the mean propulsive power in moderate waves with relatively good accuracy.

* Corresponding author at: Department of Mechanics and Maritime Sciences, Chalmers University of Technology, Gothenburg, Sweden.
E-mail address: orych@chalmers.se (M. Orych).

https://doi.org/10.1016/j.oceaneng.2023.115289
Received 15 March 2023; Received in revised form 14 June 2023; Accepted 29 June 2023
Available online 11 July 2023

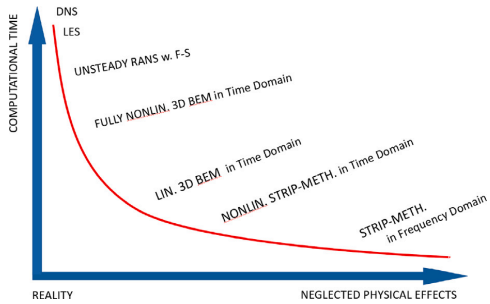

Fig. 1. Computational methods for seakeeping.

Nomenclature

ω	Specific turbulence dissipation rate
C_F	Frictional resistance coefficient
C_P	Pressure resistance coefficient
C_T	Total resistance coefficient
C_{AW}	Added resistance in waves coefficient
f_w	Weather factor
k	Turbulent kinetic energy
k_S	Equivalent sand grain roughness height
n_g	Number of grid cells
P_D	Delivered power
U_G	Grid uncertainty

Even though it is possible to combine hydro- and aerodynamic simulations in one computation as presented by Zhang and Kim (2018), it is not practical to combine it with seakeeping. It is a common practice to consider wind resistance in self-propulsion simulations as an external resistance component. This can be estimated through wind tunnel testing, CFD methods or empirical formulations, ITTC (2021b).

In this paper, we propose a similar hybrid BEM/RANS method for predicting the powering performance, including speed loss, of full-scale ships in irregular waves. The method is based on a newly developed, fully nonlinear, unsteady potential flow solver for free surface flows with floating bodies, subject to 6DOF, see Coslovich et al. (2021). This gives the added resistance in waves, which is combined with a potential flow for calm water wave resistance and a double-model steady-state RANS solver for self-propulsion at full scale. More than an order of magnitude is gained in computational time compared to unsteady RANS, and the accuracy is at the same level. The method should be of interest both in vessel design and in connection with current and future regulations, such as the EEDI. Note that the scope is limited to normal operating conditions and does not include severe survival modes.

2. Numerical method

The software used in this project is SHIPFLOW, developed over a long period of time at Chalmers University of Technology and FLOWTECH. It includes several modules and solvers. The calm water wave resistance, including sinkage and trim, is computed using the potential flow solver XPAN, (Janson, 1997), and the steady-state RANS solver XCHAP is used to simulate self-propulsion at full scale, Korkmaz (2015). Added resistance is obtained using the newly developed seakeeping module MOTIONS (Coslovich et al., 2021). Results from all the solvers can be combined in a chain of simulations to provide necessary resistance components for self-propulsion simulations in waves.

2.1. Added resistance in waves

MOTIONS is based on a fully nonlinear unsteady potential flow solver for free surface flows with floating bodies subject to 6DOF. It has an internal automatic mesh engine for rigid bodies and the free surface, as well as support for importing externally generated meshes of rigid bodies or environment boundaries. The rigid body meshes are initially refined close to the free surface and in regions with large curvature and, after that, kept the same throughout the computation.

In each time step, the free surface mesh is initialized with a coarse mesh. The free surface panels completely inside a rigid body are then cut away, and panels partially inside a rigid body are split into four panels. This is done a specified number of times recursively. Subsequently, the free surface panel nodes closest to the rigid body are snapped the rigid body. Additionally, the free surface mesh is refined in regions with large free surface curvature, see Fig. 2.

The free surface is traced by markers using a mixed Eulerian–Lagrangian approach. In the Eulerian step, the velocity potential and velocity of each marker are computed with a boundary element method (BEM). In the Lagrangian step, the free surface boundary conditions are integrated in time, and the marker's position and velocity potential are updated.

Once the Lagrangian step is finished, a new free surface mesh is generated by interpolating the surface elevation from the marker's updated positions. In addition, the boundary conditions for the next Eulerian step are obtained by interpolating the velocity potential of the markers. The interpolations on the free surface are done with thin-plate splines, Duchon (1976).

The hull body motions are calculated by summing up the pressure forces on the hull panels and integrating the corresponding rigid body acceleration in time. The total pressure on the hull is given by Bernoulli's equation, and for robustness reasons, an acceleration potential is used to obtain the time derivative of the velocity potential. A 4th-order Adams–Bashforth–Moulton predictor–corrector method is utilized for time integration.

Several measures have been taken to lower the computational time. For instance, a nonlinear decomposition of the solution into an undisturbed incident wave field and a disturbance field due to the presence of the hull, Ducrozet et al. (2014). This ensures that incident waves far from the hull do not have to be resolved by the BEM and thereby larger panels can be used away from the hull without affecting the quality of the incident wave field, which is described analytically by 5th-order Stokes wave theory. Another example is the use of a modified Barnes–Hut algorithm, where panels are grouped together into nodes based on the distance to the point where their influence is to be computed, Barnes and Hut (1986).

The code has an automatic way to detect risks for wave breaking and applies additional pressure in such regions of the free surface to mitigate local wave breaking, Mola et al. (2017). Additionally to avoid wave reflections from the domain boundaries a damping zone is introduced. A forcing term that eliminates the disturbance, i.e. the difference between the undisturbed incident waves and the total computed wave height, is applied close to the outer boundaries, Kjellberg et al. (2022).

2.2. Calm water wave resistance

XPAN is a nonlinear Rankine source panel method, Janson (1997). It uses higher-order panels and singularity distributions. Nonlinear boundary conditions are used for the free surface. Dynamic sinkage and trim are computed during the iterative procedure for the nonlinear free surface boundary condition. During each iteration, the ship is repositioned and the panelization of the hull and free surface is regenerated. An illustration of the hull and free surface panelization is shown in Fig. 3. The resulting heave and pitch are used to position the hull, and the wave resistance is added in the RANS simulations in a one-way coupling. The viscous results do not affect the trim, sinkage and wave resistance.

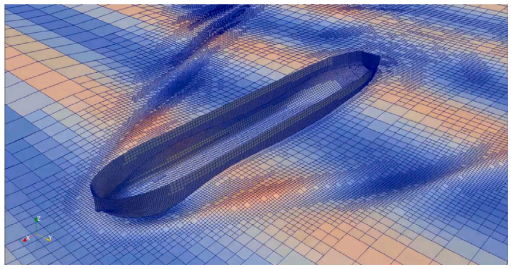

Fig. 2. An example of an adaptive mesh for the free surface.

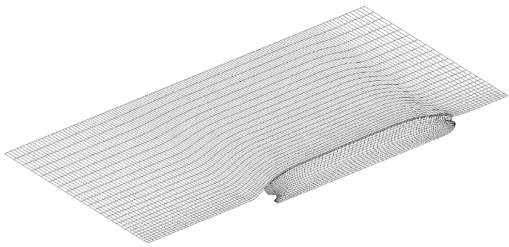

Fig. 3. Free surface and hull meshes used in XPAN simulations.

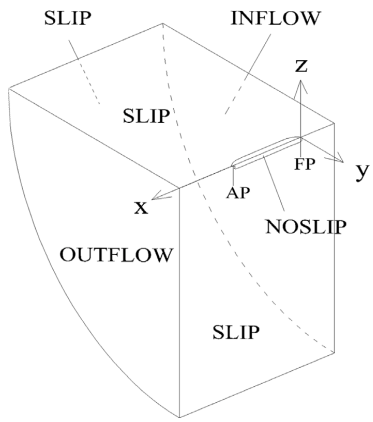

Fig. 4. Illustration of the computational domain and boundary conditions for RANS simulations.

2.3. Calm water self propulsion

XCHAP solves the steady, incompressible RANS equations using a finite volume method. The explicit algebraic stress turbulence model, EASM, Deng et al. (2005), is used in the present paper. No wall functions are used, and the equations are integrated down to the wall. The equations are discretized using the Roe scheme, Roe (1981), for the convection, while a central scheme is used for the diffusive fluxes. An explicit flux correction is applied to achieve second-order accuracy, Dick and Linden (1992), Chakravarthy and Osher (1985).

The hull roughness effect is modeled by a modification of the boundary conditions for the specific dissipation of the turbulent kinetic energy, ω and the turbulent kinetic energy, k, Orych et al. (2022).

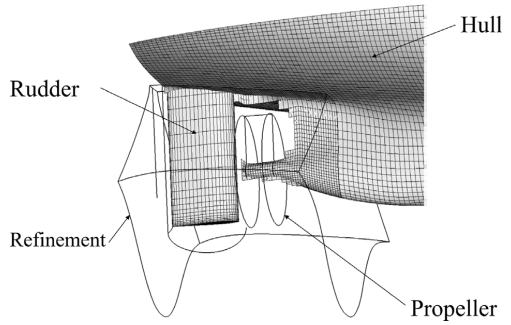

Fig. 5. Grids representing the aft part of the hull, including local refinement, along with the rudder and propeller.

The roughness is quantified using the equivalent sand grain roughness height, k_S .

XCHAP uses structured grids. A single block grid is typically generated for a bare hull case. A double-model approach is used where a symmetry condition is applied to the still-water plane, Fig. 4. Multi-block structured or overlapping grids are applied for more complex geometries such as hulls with appendages, and local grid refinements, Fig. 5.

To simulate the effect of the propeller, body forces are introduced. When the flow passes through the propeller swept volume, its linear and angular momentum increase as if it had passed a propeller with an infinite number of blades. The forces vary in space, but are independent of time, and generate a propeller-induced steady flow. The body forces are computed with a built-in lifting line propeller analysis program, Zhang (1990). Additionally, a friction resistance component is accounted for that contributes to the propeller torque. This simple modeling is also used to take into account the blade roughness.

The computation of the body forces is embedded in an iterative procedure, where first the current approximation of the velocity field is extracted at a representative propeller plane. The effective wake is thereafter obtained by subtracting the induced propeller wake. This is the function of the propeller code and is computed by the circulation from the previous iteration in the lifting line method. The new circulation and forces are computed in the effective wake. Thereafter, the forces are distributed over the volume cells in the cylindrical grid. The body forces are added to the right-hand side of the flow equations. This will give a new velocity field after solving the equations. The body forces are updated in every iteration. At convergence, the total wake computed by the RANS solver and the lifting line method should match in the selected propeller plane.

To simulate self-propulsion, the program automatically adjusts the propeller rotational speed to achieve a balance between resistance and thrust, ITTC (2017a).

The momentum and continuity equations are coupled, while the turbulent quantities are solved separately. A Krylov-type solver from the PETSc software suite, PETSc (2020a), is used to solve linear equations. The selected GMRES, PETSc (2020b), with the block Jacobi preconditioner, PETSc (2020c), is in this case very efficient, both in terms of convergence speed and stability.

3. Case description

A Korean VLCC test case (KVLCC2) developed by Korea Research Institute of Ships and Ocean Engineering, KRISO (formerly MOERI), was selected for this investigation. The ship and the propeller particulars are found in Table 1 and Table 2. Many experimental facilities have tested the model. In this paper, we will use recent data from SSPA, Sweden. The measurements include resistance, propulsion in scale 1:45.7 and seakeeping properties of the hull in scale 1:68.

Table 1
KVLCC2 main particulars.

Length between perpendiculars	L_{PP}	m	320.0
Length of waterline	L_{WL}	m	325.5
Maximum beam of waterline	B_{WL}	m	58.0
Draft	T	m	20.8
Displacement volume	∇	m^3	312 622
Wetted surface area	S	m^2	27 194
Block coefficient	C_B	–	0.8098
Midship section coefficient	C_M	–	0.9980
Longitudinal centre of gravity	$\overline{LCG}$	m	171.1
Vertical centre of gravity	$\overline{KG}$	m	18.6
Roll radius of gyration	kxx	m	23.2
Pitch radius of gyration	kyy	m	80.0
Frontal area	AF	m^2	1 200

Table 2
KP458 propeller particulars.

Type	–	–	Fixed Pitch
No. of blades	Z	–	4
Diameter	D	m	9.86
Pitch/Diameter ratio	$P/D(0.7R)$	–	0.721
Expanded area ratio	A_E/A_0	–	0.431
Hub ratio	d_h/D	–	0.155

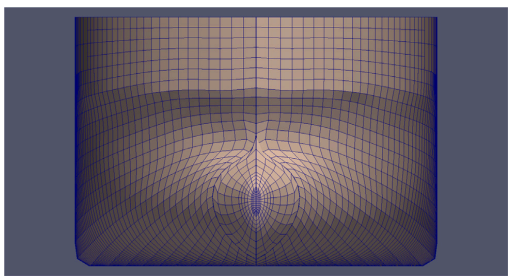

Fig. 6. Bow view of hull mesh with approximately 7000 panels.

4. Computational setup

4.1. Added resistance in waves

The hull panelization from the internal mesh engine can be seen in Figs. 6 and 7. The panelization is based on a block-structured mesh and has automatically been refined around the bow, stern, and waterline as well as in regions with large curvature. This is the coarse mesh in the grid refinement study.

The hull panels cover the entire hull, but in the computation, only the panels, entirely or partially, below the free surface are being used by the solver in each time step.

In Fig. 8 the initial free surface mesh is shown. The domain extends $4L_{PP}$ in all directions from the centre of the hull, and the free surface Cartesian background mesh has 24 panels in each direction. These panels are refined 6 times close to the hull, see Fig. 9.

The hull has no appendages in the SHIPFLOW MOTIONS setup. It starts from rest and is accelerated up to full speed. When the nominal speed is achieved the hull is released and towed with a spring preloaded to balance the friction resistance. The computations are set to simulate 20 s in model scale resulting in 46 wave encounters for the shortest and 9 wave encounters for the longest waves, respectively.

For the simulations in waves, the free surface is initialized with the undisturbed incident wave field and for the simulations in calm water, the fluid is initialized to be completely calm. As the computation progresses and the hull accelerates, the free surface disturbance from the hull grows, and panels further away from the hull are refined based on panel size and how large the free surface disturbance is. The added resistance is obtained by subtracting the resistance in calm water from the resistance in waves, both computed with MOTIONS.

The incident regular waves are modeled with the 5th-order Stokes wave theory.

Settings for the meshes and the time step size are kept the same for the whole set of computations to avoid scatter in the results due to discretization as much as possible.

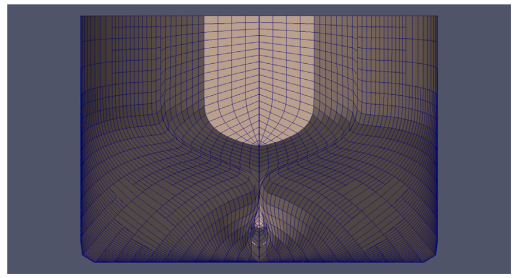

Fig. 7. Stern view of hull mesh with approximately 7000 panels.

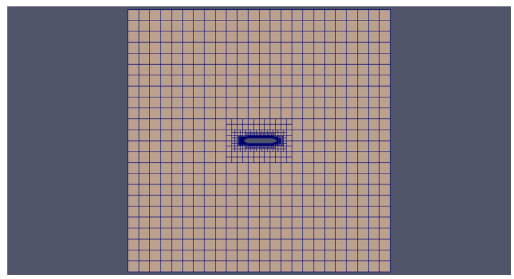

Fig. 8. The initial free surface panelization.

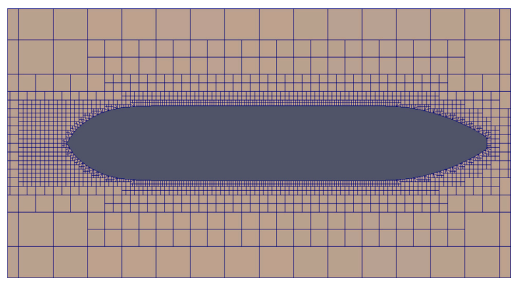

Fig. 9. Zoomed in view of the initial free surface panelization.

4.2. Calm water resistance and delivered power

To compute the wave pattern, dynamic sinkage, and trim, the XPAN module, which employs the nonlinear potential flow method, is utilized. A wave-cut integration method is employed for evaluating the wave resistance. Computing the viscous pressure resistance and friction involves using the RANS method XCHAP. For the RANS computations, an H-O structured background grid describing the hull is complemented with overlapping component grids. The domain extends 0.8 L_{PP} in front of and behind the hull, and the outer radius of the semi-cylindrical

Table 3
Cell sizes in selected regions, non-dimensionalized with L_{PP}.

GRID	Length-wise		Girth-wise	y^+
	forebody	aftbody	midship	midship
1	0.58× 10^{-3}	0.41× 10^{-3}	1.50× 10^{-3}	0.495
6	1.38× 10^{-3}	0.97× 10^{-3}	3.57× 10^{-3}	1.177

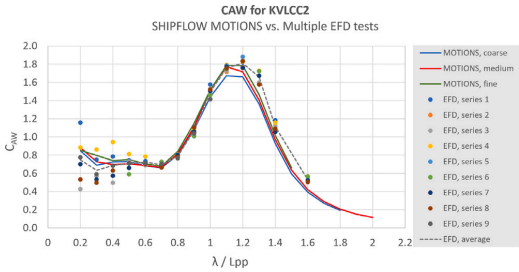

Fig. 10. Coefficient of added resistance due to regular, head sea waves for multiple measurements and simulations with three grid densities.

domain is 3.0 L_{PP}. Behind the submerged part of the transom, a separate grid block is used. An additional cylindrical domain represents the propeller. The separate rudder grid is of O-O type. The propeller and the rudder are encapsulated within a local refinement that is based on the background grid, where each cell is split to generate eight new cells. A detailed description of the applied boundary conditions is given in Broberg et al. (2022).

The simulations are performed with the fluid properties corresponding to the towing tank test conditions at model scale, and 15 °C seawater at full scale. The average hull roughness at full scale is assumed to be 100 μm.

4.3. Delivered power in waves

To obtain the delivered power in waves, two additional resistance components are introduced to the self-propulsion simulations. The first is the added resistance in waves, which was detailed in Section 4.1. The second resistance component taken into account is wind resistance. For this, we utilize the empirical method proposed by Fujiwara et al. (2005). These resistance values act as opposing forces, or 'negative towing forces', within the XCHAP solver.

5. Comparison of simulations with experimental results

5.1. Added resistance in regular waves

With the current potential flow method which uses an adaptive grid technique and employs breaking wave suppression mechanisms, see Kjellberg et al. (2022), it is not feasible to perform a strict verification study. The typical behavior of a free surface potential flow method in a systematic mesh refinement study would end up with a grid density where wave-breaking starts to appear, leading to divergence of the solution. Furthermore, the wave breaking suppression modeling employed in the current method begins to deteriorate at such small scales. In the current framework, the mesh is automatically refined to capture the free surface waves more accurately, but at the same time, the overall wave steepness is limited, and wave overturning is prevented. Therefore, a basic study is presented with three mesh resolutions to illustrate the general response to mesh refinement. The computed added resistance in regular waves at 15.5 knots of speed corresponding to Froude number Fr=0.142, is plotted in Fig. 10 together with the available test data. The measurements were performed at the

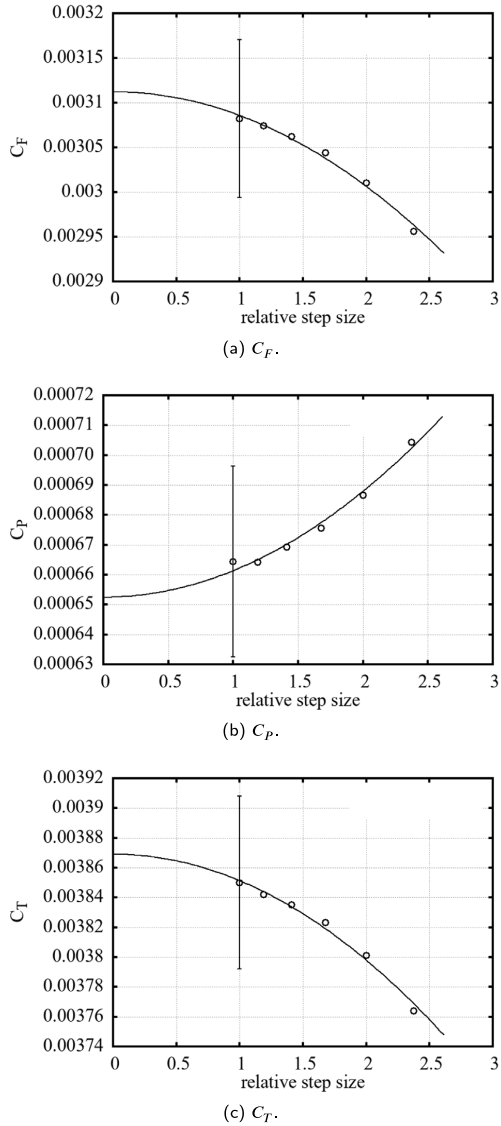

Fig. 11. Grid convergence of frictional, viscous pressure and total resistance coefficients, resistance at model scale. Error bar indicates uncertainty for the finest grid.

Maritime Dynamics Laboratory of SSPA. The collection includes multiple test series for all wave lengths, including tests with a self-propelled model and tests where the model is towed with soft springs, which is extremely valuable and not often presented, see Kjellberg and Gerhardt (2019) for further details. Even though there is a significant scatter in the data, especially for the shortest wave lengths, the simulations can be compared to the average value to judge the accuracy of the numerical method.

The simulation results are within the scatter found in the measurements for all three grid densities for λ/Lpp between 0.2 to 1.0, which is

Table 4
Total resistance coefficient uncertainty and deviations from the infinitely large grid.

GRID	$n_g \times 10^6$	$C_T \times 10^{-3}$	$U_G\%S_i$	$\lvert C_{Ti} - C_{T0}\rvert \%C_{T0}$
0	∞	3.869	–	–
1	16.6	3.850	1.5%	0.5%
2	9.9	3.842	2.1%	0.7%
3	5.9	3.835	2.9%	0.9%
4	3.5	3.823	4.1%	1.2%
5	2.1	3.801	5.8%	1.8%
6	1.2	3.764	8.2%	2.7%

essential to the current investigation. The longest waves do not overlap with the irregular wave energy spectrum of the investigated sea state, which will be seen later.

From the presented validation, it can be concluded that the viscous effects on added resistance in waves are limited for these conditions. In fact, the measurement accuracy should be of greater concern, especially for shorter waves. For the following resistance computations in this paper, the coarse mesh was used to minimize the computational time.

5.2. Calm water resistance and delivered power

The verification is carried out to investigate the numerical uncertainty. It is performed for a resistance case at the design speed. The least square root, LSR, is the method used to determine the numerical uncertainty and the order of accuracy, Eça and Hoekstra (2014). A software tool prepared by MARIN, MARIN (2018), is used to process the results.

The grid refinement ratio is $\sqrt[4]{2}$ in each direction of the structured volume grid for RANS simulations. The total number of cells ranges from 1.2×10^6 to 16.6×10^6 at model scale. The cell sizes in selected regions for the finest (#1) and coarsest (#6) grids are given in Table 3. The length and girth-wise sizes are non-dimensionalized by L_{PP}. It should be noted that the aftbody cell size in the length-wise direction is given in a region where the overlapping grid refinement is used. The number of cells in the normal direction for the full-scale simulations is about 65% larger compared to the model scale, to compensate for the clustering of cells close to the hull, due to the stretching necessary to keep y^+ according to the requirements of the turbulence model.

The grid convergence results are plotted in Fig. 11. The horizontal axis represents the relative step size between the grids. The total resistance coefficient and its frictional and pressure components indicate monotonous grid convergence with small uncertainties and limited scatter.

Table 4 contains C_T results obtained for all grid sizes, n_g, as well as the value extrapolated to an infinite number of cells. Since it is often not practical to use the finest grid that was included in the verification study, the uncertainties for coarser grids are also very important, here expressed as a percentage of the solution for each grid, S_i. The last column can be of particular interest to the designers. It shows a difference between C_{T0}, the value extrapolated to zero step size, and each grid result, C_{Ti}, in percent of C_{T0}.

Considering the computational effort, the fourth-finest grid from the verification step is used in the validation. To validate the computed results, the computations are compared to the model-scale towing tank measurements of the total resistance, Fig. 12. The total resistance average comparison error is about 1% for all three speeds that are considered. The delivered power computations in full-scale are compared to the measurements extrapolated to full-scale with the ITTC78 method, Fig. 13. The average comparison error is about 1% for all three speeds. The roughness effects on the hull and propeller at full scale are computed using the model implemented in the RANS code, while the aerodynamic resistance is added using the ship's frontal area and a coefficient provided by the model testing facility. Since there are no sea trials available for KVLCC2, only the comparison with the extrapolated model tests is possible. However, a full-scale validation of a smaller tanker for the same numerical method has been published earlier, Orych et al. (2021)

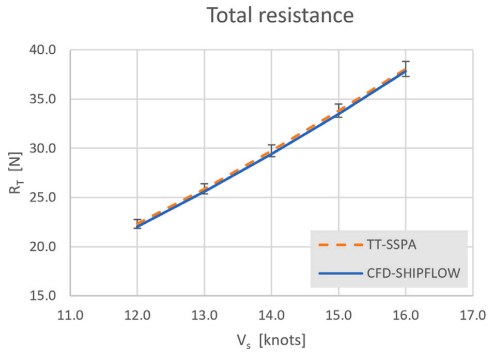

Fig. 12. Validation of total resistance measured at SSPA towing tank and CFD simulations. Error bars indicate 2% error for reference.

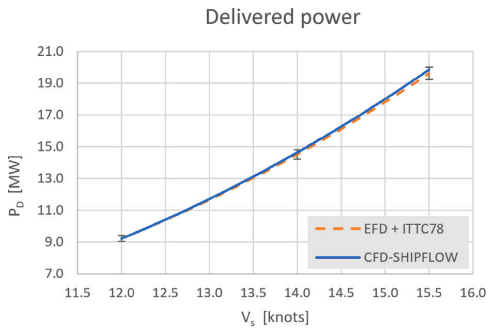

Fig. 13. Comparison of full-scale delivered power extrapolated from measurements with ITTC78 method and predicted by CFD simulations. Error bars indicate 2% error for reference.

6. Speed loss prediction

The speed loss of a ship in a seaway can be expressed as a weather factor, f_w, calculated from the speed achieved in certain wave and wind conditions and the speed in calm water at the same delivered power. In the ITTC guidelines, ITTC (2021b), three methods are illustrated: experiments, numerical simulations or empirical formulas can be used to achieve various levels of fidelity. The high-fidelity methods are often less practical due to the cost and time involved. The method presented here can be used in the ship design stage but at the same time give good accuracy, see Fig. 14 where the current approach is highlighted.

6.1. Added resistance in waves

The added resistance in waves is computed for three speeds, 12.5, 13.5 and 14.5 knots (Froude number of 0.11, 0.12 and 0.13) and three wave directions, 0° (head waves), 30° and 60°, for a range of regular wave lengths from 0.2 to 1.8 λ/L_{PP}, see Fig. 15 illustrating the C_{AW} at 14.5 knots of ship speed. The response in the shortest waves, below $\lambda/L_{PP} = 0.2$, is estimated with STAwave-II method, ITTC (2021a). It is an empirical method developed to estimate the transfer function related to the average increase in resistance for a ship in regular head waves. This method uses primary parameters such as the dimensions of the ship and its speed. To achieve this, a comprehensive array of seakeeping model test results for a large number of ships has been utilized. The STAwave-II method addresses both types of resistance

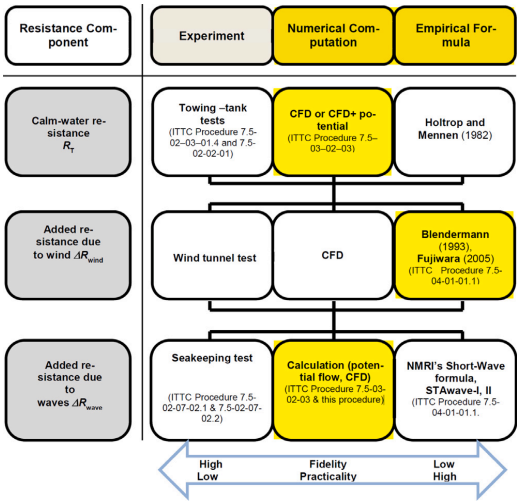

Fig. 14. Methods used to determine total resistance in waves, ITTC (2021b).

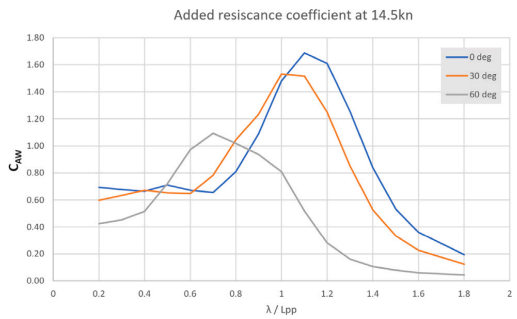

Fig. 15. C_{AW} for three wave directions at 14.5 knots, Fr=0.13.

increase in wave conditions: the wave reflection-induced increase and the motion-induced resistance.

The mean resistance in irregular waves is calculated by integrating the transfer function of the mean added resistance in regular waves with the wave spectrum, $S(\omega)$. The mean resistance increase for irregular waves is given by

$$\overline{R_{AW}(\alpha)} = 2\int_0^{2\pi} \frac{R_{AW}(\omega,\alpha)}{\zeta_A^2(\omega)} S(\omega)\, d\omega \tag{1}$$

where $R_{AW}(\alpha)$ is the mean resistance increase in regular waves for a given wave direction, and ζ_A is the corresponding wave amplitude.

For the weather factor calculations, a spectrum described in ITTC with significant wave height, H_S, of 3.0 m and zero up-crossing period, T_Z, of 6.16 s is used. The wave spectrum given by IMO (2012) is:

$$S = \frac{A_S}{\omega^5} e^{-\frac{B_S}{\omega^4}} \tag{2}$$

where

$$A_S = \frac{H_S^2}{4\pi}\left(\frac{2\pi}{T_Z}\right)^4 \text{ and } B_S = \frac{1}{\pi}\left(\frac{2\pi}{T_Z}\right)^4 \tag{3}$$

When the spectrum and C_{AW} are plotted together it can be seen that for this sea state, the wave energy is concentrated in the region between

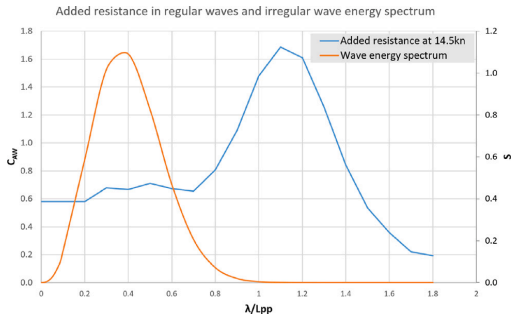

Fig. 16. Irregular wave energy spectrum and ship added resistance coefficient in regular head waves at 14.5 knots.

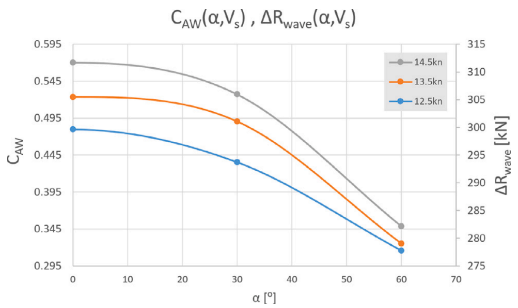

Fig. 17. Mean added wave resistance for three speeds as a function of wave direction.

0.1 to 0.8 λ/L_{PP}, while the C_{AW} peak is outside of these conditions, see Fig. 16. Therefore, the mean added resistance due to the waves will depend more on the wave reflection and diffraction rather than radiation, i.e. the motion-induced resistance.

The mean added wave resistance for the KVLCC2 hull for three speeds for three different wave directions is illustrated in Fig. 17. The maximum values for each speed occur for the head waves.

An additional simulation is carried out in irregular waves at the highest speed in head waves. This is done to check if the results would be similar to those obtained by integrating the regular wave transfer function of the mean resistance with the irregular wave energy spectrum. Sea state 5 wave spectrum according to ITTC, is realized with a significant wave height of 3.0 m and a zero up-crossing period of 6.16 s. The wave energy spectrum is shown in Fig. 16. Using the same mesh as in the regular waves, the simulations are executed for 320 seconds in full-scale, corresponding to 110 wave encounters, zero up-crossings, in this case. The longer simulation is needed to provide sufficient statistical data for obtaining the average resistance. The difference between integrating the added resistance in regular waves with the wave spectrum and the added resistance computed in irregular waves is about 5%. This test is done to cross-check the numerical results and see if the simulation time can be shortened. In this case, running in irregular waves takes about half the time needed for the entire range of regular waves. The authors do not have the measurements in the irregular waves for this particular case to illustrate the validity, but the simulation results seem promising both in terms of agreement with the regular waves and the execution time.

6.2. Speed-power curves

The weather factor, f_w signifies the percentage of the ship's calm water speed that it can sustain when encountering Beaufort 6 weather

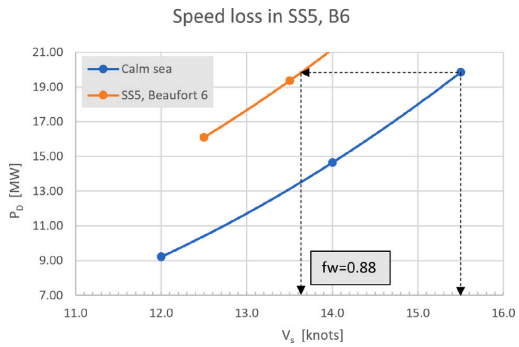

Fig. 18. Speed-power curves for calm water and in State 5 head seas with Beaufort 6 wind.

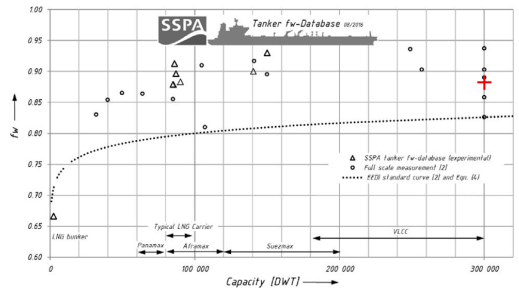

Fig. 19. f_w database for tankers, Gerhardt and Kjellberg (2017). The result from the current method is marked with red "+" symbol.

conditions and corresponding waves, Gerhardt and Kjellberg (2017). Estimating that factor requires power prediction in calm water and in waves. The resistance due to the waves and the apparent wind is added as an external force in the self-propulsion simulations. For both conditions, we compute the delivered power, and the speed loss at the given P_D is estimated, see Fig. 18. In this case, the weather factor is 0.88. It is about 6.5% higher than the more conservative standard curve for the weather factor in EEDI, which represents the effect of wind and waves on the energy efficiency of a ship (IMO, 2012). The simulation result corresponds well also to the excerpt from SSPA's database for tankers, see Fig. 19.

7. Discussion

The presented method attempts to deliver accurate and fast predictions of power requirements for ships sailing in waves. It combines the unsteady potential flow simulations in waves with the steady state self-propulsion at full scale. On average, the simulations require approximately 1.5 h per case in waves and 2 h for self-propelled cases on a single node with a 24-core CPU. Assuming that a sufficient number of runs are completed, such as 8 wave lengths for the seakeeping part and 6 propelled cases to estimate delivered power, the total time required for assessing the speed loss is approximately one day.

Since the mean added resistance in waves and the aerodynamic resistance are directly used in the propulsion simulations to increase the total resistance, this approach certainly has its limitations. The propeller performance is not affected by the time-varying wake, propeller and free surface interactions, submergence and loading. This technique is compared with quasi-steady and fully unsteady approaches in Saettone et al. (2020). The described relative propeller torque difference between steady and unsteady approach for wave length $\lambda/L = 1.0$ with 2% steepness, is about 2.5% and diminishes with lower wave heights and shorter lengths. For the case presented in the current paper, the sea state 5 spectrum peak is at $\lambda/L = 0.4$ and the energy spectrum goes to zero at $\lambda/L = 1.0$. The pitch and heave responses are small, and the propeller submergence is not changed significantly. It is likely that the time-varying flow effects are small for the presented case, but further investigation is necessary to confirm this assumption.

By analyzing its limitations, we can determine the range of applications for which this method can be confidently used. However, it should be noted that spray, large hull motions that may result in propeller ventilation, or high propeller loading cannot be precisely accounted for. Nevertheless, the presented method shows reliable predictions for standard seakeeping tests conducted in regular waves. Furthermore, the simulations conducted in irregular waves for a moderate sea state show good agreement with the integrated irregular wave spectrum and transfer function of the mean added resistance observed in regular waves. These results suggest that the presented approach could serve as a valuable complement to physical testing, offering ship designers a useful tool for initial design and optimization.

8. Conclusions

The main objective of this paper is to present an efficient and accurate numerical method to estimate the power requirements in waves. The method is suitable for calculations of the added power in waves or the weather factor, f_w, of the attained energy efficiency design index for new ships, EEDI. The comparison between the numerical simulations and the experimental results of the resistance, the delivered power and the added resistance in waves indicate good accuracy. The resistance and the delivered power comparison errors are about 1% at the considered speeds. The estimated weather factor is consistent with the values derived from full-scale measurements included in the example database of similar ships. However, the accuracy may deteriorate for relatively larger waves where the time-varying wake, propeller submergence and loading cannot be neglected.

CRediT authorship contribution statement

Michal Orych: Conceptualization, Methodology, Software, Validation, Visualization, Writing – original draft. **Magnus Östberg:** Methodology, Software, Validation, Writing – original draft. **Martin Kjellberg:** Methodology, Software, Validation, Writing – original draft. **Sofia Werner:** Data Curation, Writing – review & editing. **Lars Larsson:** Supervision, Writing – review & editing.

Declaration of competing interest

The authors declare that they have no known competing financial interests or personal relationships that could have appeared to influence the work reported in this paper.

Data availability

Data will be made available on request.

Acknowledgments

The authors would like to thank: Energimyndigheten, Sweden (Swedish Energy Agency, project 49300-1) for the financial support and SSPA AB for providing highly valuable validation data.

References

Barnes, J.E., Hut, P., 1986. A hierarchical O(n-log-n) force calculation algorithm. Nature 324, 446.

Broberg, L., Regnström, B., Östberg, M., 2022. XCHAP – Theoretical Manual. FLOWTECH International AB, Gothenburg, Sweden.

Chakravarthy, S., Osher, S., 1985. A new class of high accuracy TVD schemes for hyperbolic conservation laws. In: 23rd Aerospace Sciences Meeting, Reno, NV, U.S.A., AIAA Paper No 85–0363.

Coslovich, F., Kjellberg, M., Östberg, M., Janson, C.-E., 2021. Added resistance, heave and pitch for the KVLCC2 tanker using a fully nonlinear unsteady potential flow boundary element method. Ocean Eng. 229, 108935. http://dx.doi.org/10.1016/j.oceaneng.2021.108935, URL: https://www.sciencedirect.com/science/article/pii/S002980182100370X.

Deng, G.B., Queutey, P., Visonneau, M., 2005. Three-dimensional flow computation with Reynolds Stress and Algebraic Stress Models. In: Procedings of the ERCOFTAC International Symposium on Engineering Turbulence Modelling and Measurements; ETMM6, Sardinia, Italy, 23–25 May, 2005. pp. 389–398.

Dick, E., Linden, J., 1992. A multigrid method for steady incompressible Navier-Stokes equations based on flux difference splitting. Internat. J. Numer. Methods Fluids 14, 1311–1323.

Duchon, J., 1976. Splines minimizing rotation-invariant semi-norms in Sobolev spaces. In: Schempp, W., Zeller, K. (Eds.), Constructive Theory of Functions of Several Variables: Proceedings of a Conference Held at Oberwolfach, Germany, April 25 - May 1, 1976. In: Lecture Notes in Mathematics, vol. 571, Springer, pp. 85–100.

Ducrozet, G., Engsig-Karup, A.P., Bingham, H.B., Ferrant, P., 2014. A non-linear wave decomposition model for efficient wave-structure interaction. Part A: Formulation, validation and analysis. J. Comput. Phys. 257, 863–883.

Eça, L., Hoekstra, M., 2014. A procedure for the estimation of the numerical uncertainty of CFD calculations based on grid refinement studies. J. Comput. Phys. 262, 104–130.

Fujiwara, T., Ueno, M., Ikeda, Y., 2005. A new estimation method of wind forces and moments acting on ships on the basis of physical component models. J. JASNAOE 2.

Gerhardt, F.C., Kjellberg, M., 2017. Determining the EEDI 'Weather Factor' FW. In: Influence of EEDI on Ship Design & Operation, 13 September 2017, London.

Hino, T., Stern, F., Larsson, L., Visonneau, M., Hirata, N., Kim, J., 2021. Numerical ship hydrodynamics. In: An Assessment of the Tokyo 2015 Workshop. In: Lecture Notes in Applied and Computational Mechanics, vol. 94, Springer Nature, Switzerland, http://dx.doi.org/10.1007/978-3-030-47572-7.

IMO, 2012. Interim Guidelines for the Calculation of the Coefficient FW for Decrease in Ship Speed in a Representative Sea Condition for Trial Use. IMO Circular MEPC.1/Circ.796.

IMO, 2018. Guidelines on the Method of Calculation of the Attained Energy Efficiency Design Index (EEDI) for New Ships. RESOLUTION MEPC.308(73).

IMO, 2022. Guidelines on the Method of Calculation of the Attained Energy Efficiency Existing Ship Index (EEXI). Resolution MEPC.350(78).

ITTC, 2017a. 1978 ITTC Performance Prediction Method, ITTC Quality System Manual, Recommended Procedures and Guidelines. Propulsion Committee of the 28th ITTC.

ITTC, 2021a. Preparation, Conduct and Analysis of Speed/Power Trials, ITTC Quality System Manual, Recommended Procedures and Guidelines. Specialist Committee on Ships in Operation at Sea of the 29th ITTC.

ITTC, 2021b. Calculation of the Weather Factor f_w for Decrease of Ship Speed in Wind and Waves, ITTC Quality System Manual, Recommended Procedures and Guidelines. Specialist Committee on Ships in Operation at Sea of the 29th ITTC.

Janson, C.-E., 1997. Potential Flow Panel Methods for the Calculation of Free-Surface Flows with Lift (Ph.D. thesis). Chalmers University of Technology, Gothenburg, Sweden.

JoRes, 2023. JoRes Web Page. https://jores.net.

Kim, M., Hizir, O., Turan, O., Day, S., Incecik, A., 2017. Estimation of added resistance and ship speed loss in a seaway. Ocean Eng. 141, 465–476. http://dx.doi.org/10.1016/j.oceaneng.2017.06.051.

Kjellberg, M., Gerhardt, F.C., 2019. Improved methods for the experimetal determination of "added resistance in waves". In: AMT Conference <9-11 October 2019, Rome Italy.

Kjellberg, M., Gerhardt, F., Werner, S., 2022. Sailing in waves : A numerical method for analysis of seakeeping performance and dynamic behavior of a wind powered ship. In: SNAME 24th Chesapeake Sailing Yacht Symposium, CSYS 2022. Society of Naval Architects and Marine Engineers, RISE Research Institutes of Sweden, Maritime department.

Korkmaz, K.B., 2015. CFD Predictions of Resistance and Propulsion for the JAPAN Bulk Carrier (JBC) with and Without an Energy Saving Device (MSc Thesis). Chalmers University of Technology, Gothenburg, Sweden.

Larsson, L., Stern, F., Visonneau, M., 2014. Numerical Ship Hydrodynamics - An Assessment of the Gothenburg 2010 Workshop. Springer Verlag, http://dx.doi.org/10.1007/978-94-007-7189-5.

MARIN, 2018. Numerical Uncertainty Analysis – User Manual. MARIN, The Netherlands.

Mola, A., Heltai, L., DeSimone, A., 2017. Wet and dry transom stern treatment for unsteady and nonlinear potential flow model for naval hydrodynamics simulations. J. Ship Res. 61, 1–14.

Orych, M., Werner, S., Larsson, L., 2021. Validation of full-scale delivered power CFD simulations. Ocean Eng. 238, 109654. http://dx.doi.org/10.1016/j.oceaneng.2021.109654.

Orych, M., Werner, S., Larsson, L., 2022. Roughness effect modelling for wall resolved RANS – Comparison of methods. Ocean Eng. 266, 112778. http://dx.doi.org/10.1016/j.oceaneng.2022.112778.

PETSc, 2020a. PETSc web page. https://www.mcs.anl.gov/petsc/index.html.

PETSc, 2020b. PETSc documentation, solvers. https://www.mcs.anl.gov/petsc/petsc-current/docs/manualpages/KSP/KSPGMRES.html.

PETSc, 2020c. PETSc documentation, preconditioners. https://www.mcs.anl.gov/petsc/petsc-current/docs/manualpages/PC/PCBJACOBI.html.

Roe, P.L., 1981. Approximate Riemann solvers, parameter vectors, and difference schemes. J. Comput. Phys. 43, 357.

Saettone, S., 2020. Ship Propulsion Hydrodynamics in Waves (Ph.D. thesis). Technical University of Denmark.

Saettone, S., Tavakoli, S., Taskar, B., Jensen, M.V., Pedersen, E., Schramm, J., Steen, S., Andersen, P., 2020. The importance of the engine-propeller model accuracy on the performance prediction of a marine propulsion system in the presence of waves. Appl. Ocean Res. 103, 102320. http://dx.doi.org/10.1016/j.apor.2020.102320, URL: https://www.sciencedirect.com/science/article/pii/S0141118720302893.

Zhang, D.H., 1990. Numerical Computation of Ship Stern/Propeller Flow (Ph.D. thesis). Chalmers University of Technology, Gothenburg, Sweden.

Zhang, Y., Kim, B., 2018. A fully coupled computational fluid dynamics method for analysis of semi-submersible floating offshore wind turbines under wind-wave excitation conditions based on OC5 data. Appl. Sci. 8 (11), URL: https://www.mdpi.com/2076-3417/8/11/2314.

Paper IV

Hydrodynamic Optimization of Pre-swirl Stator by CFD and Model Testing

K. Kim, M. Leer-Andersen, S. Werner, **M. Orych**, Y. Choi

29th Symposium on Naval Hydrodynamics Gothenburg, Sweden (August 2012)

Paper V

Hydrodynamic Optimization of Energy Saving Devices in Full Scale

K. Kim, M. Leer-Andersen, **M. Orych**

30th Symposium on Naval Hydrodynamics Hobart, Tasmania, Australia
(November 2014)